MODELING AND CONTROL OF A HEAT GUN

HUANG YING

A THESIS SUBMITTED

FOR THE DEGREE OF MASTER OF ENGINEERING

DEPARTMENT OF ELECTRICAL AND COMPUTER

ENGINEERING

NATIONAL UNIVERSITY OF SINGAPORE

2006

Acknowledgements

I would like to express my great appreciation to my supervisor, A/P Loh Ai Poh for her continuous and invaluable guidance and encouragements throughout my research. With her constant guidance, I was able to clarify my thoughts each time I encounter a problem.

I would also like to thank Mr Wang Lan for his help in many problems I encountered with the FLUENT software.

My project will not have been so smooth without the help of many of my colleagues in the Advanced Control Technology lab. They are S Mainavathi, Lim Li Hong Idris, Fu Jun, Liu min, and Wu Dongrui. I thank all the people who have directly or indirectly contributed to my project.

I am grateful to the National University of Singapore for the research scholarship.

Last, but not least, special thanks should be given to my family.

Contents

List of Tables

List of Figures

Summary

In this thesis, a heat gun is designed to deliver a stream of hot air which satisfies certain temperature and velocity uniformity specifications.

The heat gun was initially designed and simulated in the software FLUENT. From the simulation results, the parameters and some supplements which improve the output uniformity of the heat gun were identified. It was found that increasing the length of the pipe, and adding a heating coil near the pipe, help in achieving temperature uniformity. The use of heat recycle, which recycles the output air into the input helps in improving energy efficiency.

Based on the results obtained, the different components of the heat gun were modelled. They are the DC motor for driving the air, the main resistive coils for heating the air, the insulated pipe acting as the air flow path, the additional coil for compensating the heat loss near the end of the pipe, and the heat recycle.

Various control methods for the heat gun are also proposed. They are proportional -integral-derivative control, state feedback control, linear-quadratic state-feedback regulator and linear-quadratic-Gaussian control. For each control method, the effect of the control parameters were observed and used in improving the performance of the heater. In order to enhance the quality of the control, problems of disturbance rejection, actuator saturation, measurement noise are also discussed.

The final design of the heat gun was able to deliver a stream of hot air with a temperature uniformity of $\pm 0.5\ ^oC$ for a range of temperature between $120\,^oC$ and $200\,^oC$, with a uniformity of $\pm 1\,m/s$ at a velocity of at least $5\ m/s$.

Chapter 1

Introduction

1.1 Motivation and Objective

Integrated circuits (IC) consist of a large number of individual components, such as transistors, resistors, capacitors etc., fabricated on a common substrate and wired together to perform a particular circuit function. One of the greatest challenges in IC design (Plummer *et al.*, 2000) is in achieving smaller component sizes which allow more components to be integrated on a given area. The decreasing component sizes are characterized by the minimum line width, which is defined as the smallest feature size printable on the wafer surface during the fabrication process. According to the National Technology Roadmap for Semiconductors, the minimum feature size will be 100 nm in 2006. With such dimensions, more stringent demands are placed on the manufacturing process. In the case of wafer processing, the variations in the temperature distribution across the wafer must be kept within 1 ^oC in order to minimize the variations in the feature sizes. One of the on-going research projects at NUS is the processing of wafers by the use of hot air. The advantages of the method are listed as follows:

1. The process is simple.

2. This baking process is able to achieve a temperature uniformity within 0.1 ^oC across the whole wafer of 300 mm in diameter.

3. The whole process is easily scalable to multi-wafer processing.

This method of wafer processing however requires the heater to deliver hot air with stringent temperature and velocity uniformity.

The main objective of this thesis is therefore to design an air heater which can supply the hot air as required. The requirements on the air heater are listed as follows:

1. High uniformity of the output air temperature. It is required that the temperature uniformity of the output air should be less than $\pm 0.5\ ^oC$ for a range of temperature between 120 ^oC and 200 ^oC.

2. The uniformity of the air velocity should not be more than $\pm 1\ m/s$ for air flow rate of at least 5 m/s.

3. It should also deliver hot air with an airflow rate of at least 0.04 m^3/s.

1.2 Background

At present, the commercial air heaters have some disadvantages as follows:

1. The adjustable temperature range of the heaters is limited. Although most air heaters have temperature regulators which allow the output temperature to be adjusted, the regulator scale settings are not sufficiently fine. For instance, some air heaters can only produce air with the temperature denoted by "*high*" and "*low*". Precise information on the range of exit temperature is also generally not available.

2. The adjustable velocity range of the heaters is also limited. Similar to the point above, most air heaters have air velocity regulators, which have very

coarse settings. In many cases, both temperature and velocity settings cannot be adjusted independently.

3. Hot air produced by most industrial air heaters does not have uniform temperature and velocity. In particular, the temperature uniformity is generally not within the specification of 0.5 ^oC.

In recent years, some measurement methods have been developed. Wade and Tyler (1997) designed an Holographic Interferometry system method which can quantitatively analyze the air flow and temperature of heaters. Gorlach (2004) built a model of the exit air velocity profile for a thermal gun with the use of a computational fluid dynamics (CFD) software.

It is worth noticing that there are no strict requirements of the exit air temperature and velocity uniformity for commercial air heaters. The UL 499 (1997), UL (Underwriters' Laboratories) standards of electric heating appliances which is also approved by the American National Standard Institute, has no strict standards on the uniformity of the exit air temperature and velocity. In addition, manufacturers of air heating products are only focused on achieving high air temperature and volume without too much regard for uniformity.

However, in practice, air with uniform temperature and velocity is needed for various applications. Some researchers have devoted their study to the uniformity in exit air temperature and velocity for air heaters. In order to achieve a uniform hot airflow, Cameron (1993) used a damper in the air path to control the air flow and the energy of the heating element and the blower, which impels air. Wang *et al.* (1996) performed a comparative study which established the use of the mesh heater originally developed by Gillespie (1993) to develop a uniformly heating airflow for heaters. Glucksman and Deros (1997) studied the construction of the electric air heater, where the shape of the heating device and guide vanes are used to guide and distribute air, so as to obtain uniformly silent low velocity air flow. Menassa

(2001) realized the control of the heating capability of the heating coil by using a thermistor as an airflow sensor to monitor the intake air. Atkins (2005) invented an electric heater which uses a baffle plate, a plate with orifices, to redistribute air so that the invented heater can provide uniform airflow. Then together with the exemplary embodiment, the outlet airflow of this heater can be controlled by monitoring and varying the inlet air pressure.

In the present markets, there is a type of air heater called the heat gun, which is a heat producing device primarily used to achieve higher uniformity in air flow. Heat gun HG−5000E produced by STEINEL company can achieve a differential exit air temperature of less than $\pm 12.2\,^oC$ and the maximum air volume as $28\,CFM$ ($0.0132\ m^3/s$). This makes HG−5000E one of the heat guns with the largest exit air volume. LEISTER Process Technologies with a leading position in heat gun technology has products with steplessly controllable temperature outputs ranging from $20\ ^oC$ to $650\ ^oC$ where the differential temperature is within $\pm 2\ ^oC$. The maximum air volume of the LESITER heat guns is $500\ l/Min$ ($8.33 \times 10^{-3}\ m^3/s$). It is noted that these commercial heat guns have small output air volumes.

1.3 Scope of the Thesis

The main aim of the study is to design, examine and develop a new air heater, also called the heat gun, to meet the requirements on temperature, velocity uniformity and air volume, as given in Section 1.1. The advantages of the newly designed heat gun, as compared to commercial air heaters, are as follows:

- This heat gun has a range of controllable air temperature and air velocity.
- Output air from this heat gun has temperature uniformity less than $\pm 0.5\ ^oC$, for a range between $120\ ^oC$ and $200\ ^oC$.
- Output air from this heat gun also has a variable velocity of at least $5\,m/s$

with good uniformity of $\pm 1\ m/s$.

In this thesis, the structural design, system analysis and control design for this heat gun to achieve the goals are discussed.

Based on the design of the heat gun, various parameters which contribute to the temperature and velocity uniformity were identified. Various subsystems of the heat gun were analyzed and modelled. Based on these models, the dynamic behavior of the heat gun was also investigated.

Different control methods for the heat gun are also presented, including Proportional -Integrator -Derivative (PID) control, state feedback control, Linear-Quadratic state-feedback Regulator (LQR) and Linear-Quadratic-Gaussian (LQG) control. In addition, disturbance rejection, actuator saturation, and the influence of heat recycle and measurement noise are also taken into consideration in the design of the controllers.

In this thesis, MATLAB is used to design the controllers, while FLUENT and GAMBIT are used to analyze the heat transfer process of the hot air in the heat gun. FLUENT is a computational fluid dynamics (CFD) software which is used for simulation, visualization, and analysis of fluid flow, heat and mass transfer, and chemical reactions. GAMBIT is a preprocessor for the CFD analysis. GAMBIT allows fast geometry modeling and high quality meshing to be achieved efficiently and these are crucial to the successful use of FLUENT. Simulations in FLUENT and GAMBIT enable the collection of data that are more accurate in designing the structure of the heat gun.

1.4 Organization

Chapter 2 gives the overview of the proposed heat gun, with its fundamental components and dimensions. Chapter 3 presents the design of the heat gun structure, from simulations performed using FLUENT and GAMBIT. In this chapter, the de-

sign of the heat gun is proposed, including the construction of the pipe, additional heater coil and the heat recycle. In Chapter 4, the models for different parts of the heat gun are analyzed, and some parameters of the heater materials are also provided. Characteristics of this heat gun are discussed and simulated in Chapter 5.

In Chapter 6, two designs of the PID controllers are discussed. In Chapter 7, other control methods including state feedback control, LQR and LQG are discussed. In the design of the controllers, disturbance rejection, heat recycle, actuator saturation and measurement noise were considered. The main findings and suggestions for further work are given in Chapter 8.

Chapter 2

Overview of the Heat Gun

2.1 Introduction

In the previous chapter, the motivation and objectives for the heat gun were introduced. The fundamental components of this heat gun will now be discussed in this chapter. The various dimensions of these components will also be presented, given the purpose and specifications of this heat gun.

2.2 Overview of the Proposed Heat Gun

In some lithography steps, Silicon wafers are required to be baked at temperatures between 120 ^oC to 200 ^oC. In some conventional lithography techniques, baking is done on a hot plate with a relatively large thermal mass compared to the wafer. In such systems, good temperature uniformity on the wafer within 0.5 ^oC is difficult to achieve due to the nature of heat transfer which does not guarantee good uniformities even if the hot plate has an absolutely uniform temperature distribution. For this reason, new techniques for baking wafers to such good temperature uniformities have to be sought. The most recent research is on the use of hot air streams to achieve this objective. Thus the heat gun proposed in this thesis is

designed for this purpose.

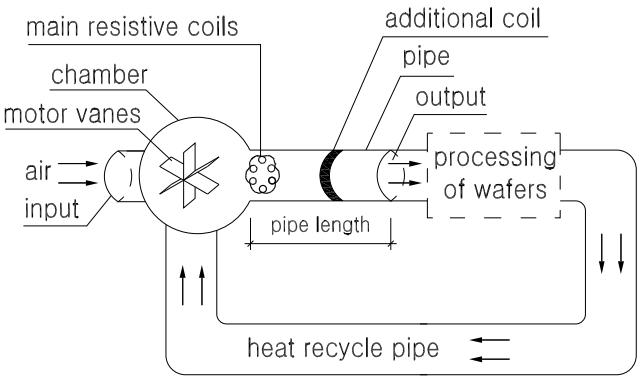

Figure 2.1: Schematic diagram of the heat gun

The proposed heat gun with its schematic diagram shown in Figure 2.1 is mainly composed of three parts:

1. A DC motor for driving the air through an output pipe.
2. A set of main electrical resistive coils for heating the air.
3. An insulated output pipe acting as a guide for the air flow.

In addition to these main parts, the heat gun also includes

1. An additional electrical resistive coil for heating the air near the exit of the pipe so as to compensate for the heat loss at the pipe wall.
2. A heat recycle unit for recycling the hot air back to the input for improved energy efficiency.

In this setup, the motor, main resistive coils and additional coil can be activated by separate electric power supplies for independent control. The heating process of the heat gun is as follows.

When the heat gun is turned on, the motor vanes suck in the air from the environment into the chamber and forces the air over the resistive coils and through

the pipe. When the air passes over the resistive coils, it is heated up. This hot air is then delivered through the pipe. The additional coil near the exit of the pipe reheats the air in order to compensate for the heat lost to the pipe wall.

The wafer processing system is attached to the end of the output pipe so that the hot air is directly transferred into the system to bake the wafer. Since the Silicon wafer is thin and its thermal conductivity is much better than air, much of the air at the exit of the wafer processing system remains relatively hot. Thus, it will be highly inefficient if this air is simply discharged into the atmosphere. In order to improve the energy efficiency, heat recycling is considered in the design of the heat gun.

The main specifications of the heat gun are thus as follows :

1. It must deliver air at temperatures between 120 ^oC and 200 ^oC with a uniformity better than 0.5 ^oC.

2. The wafer processing system requires an air volume transfer rate of at least 0.04 m^3/s assuming that air is incompressible. The velocity requirement is at least 5 m/s.

3. The uniformity in velocity of the air is also important and is set at ± 1 m/s at the velocity of $5\,m/s$.

In order to satisfy the specifications given above, the control tasks of the heat gun must also be well designed, taking into consideration power saturation and efficiency. To achieve this, the DC motor, the main resistive and additional coils are controlled separately.

2.3 Dimensions of the Heat Gun

The primary structure of the heat gun is shown in Figure 2.2. It consists of 3 main sections : (a) a short inlet section, (b) a spherical chamber which houses the

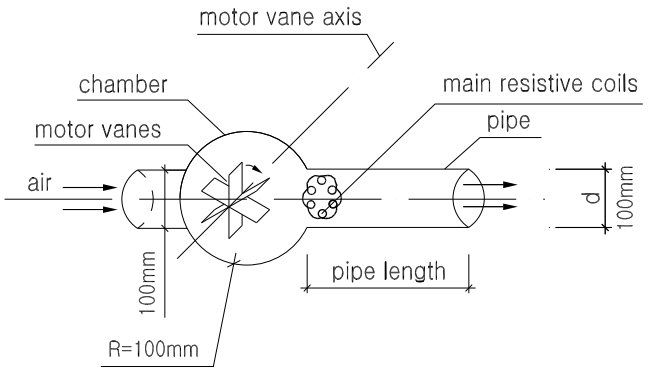

Figure 2.2: Primary structure of the heat gun

DC motor and (c) a straight output pipe. Given that the gun has to deliver air at 0.04 m^3/s at no less than 5 m/s, the pipe diameter is chosen to be 100 mm in diameter. Thus the spherical chamber chamber is chosen as 200 mm in diameter and the inlet section is also set at 100 mm in diameter.

At the entrance of the output pipe, the main resistive coils are distributed uniformly along the pipe for a distance of 30 mm. These coils are made of electric resistive wires which are evenly spaced and placed like a net as shown in Figure 2.3. The specifications for the resistive coil will be determined in Chapter 3.

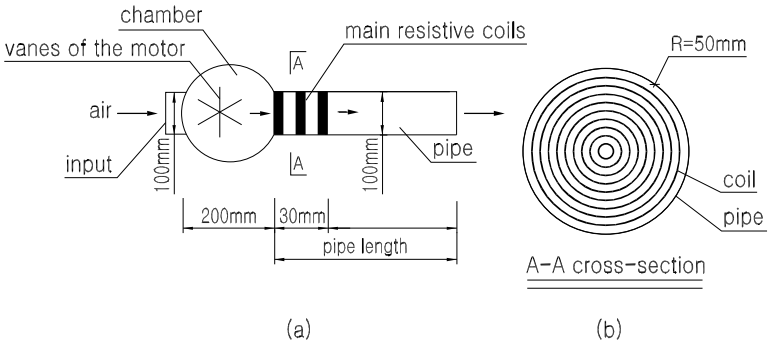

Figure 2.3: Dimension diagram of the primary heat gun

2.4 Region of Uniformity for the Proposed Heat Gun

The natural velocity and temperature profiles of the air at the output of the heat gun are studied in this design. As the hot air moves through the pipe, the layer of air that is near the pipe wall adheres to the surface of the pipe wall. Thus, it can be expected that the air velocity at the outlet of the pipe will be non-uniform. In addition, a great amount of heat is lost to the pipe wall by the air near the pipe wall. Hence, the air temperature across the cross-section of the outlet will also be non-uniform (see Figure 2.4) under the condition that the input air has uniform temperature.

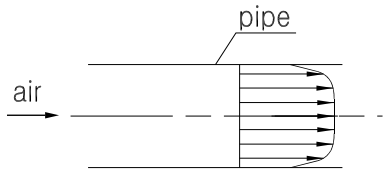

Figure 2.4: Temperature profile for the flow in a pipe

The velocity profiles of laminar and turbulent flow in a pipe are shown in Figure 2.5 (Holman, 1997) where the input air has a uniform velocity. The velocity profile for laminar flow is approximately a parabola. When the flow is turbulent, the velocity profile is relatively flat except for a small marginal part, where the velocity profile is nearly linear, near the pipe wall. The air velocity of zero on the pipe wall cannot be changed. Therefore, according to the dimensions of the proposed heat gun, when we refer to the velocity uniformity afterwards, we refer to the velocity in the circular region which has a diameter of $90\,mm$ as shown in Figure 2.6, which ensures that more than 80% output air meets the requirement of the velocity uniformity.

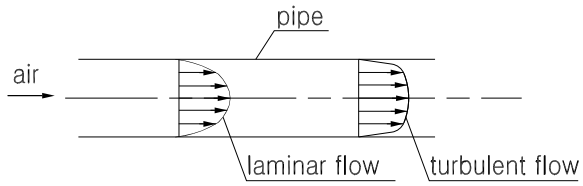

Figure 2.5: Velocity profiles for laminar and turbulent flow in a pipe

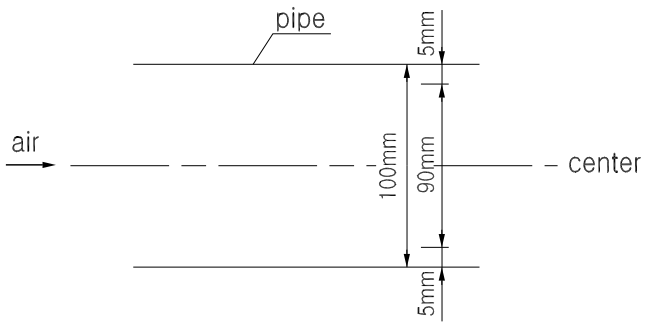

Figure 2.6: Region of the velocity uniformity

2.5 Power Consumption of the Heat Gun

The heat gun is required to deliver hot air at between 120 ^oC and 200 ^oC. The air flow rate is at least 0.04 m^3/s. From steady state calculations based on

$$power = \rho \times air\ volume \times c_p \times (final\ temp - initial\ temp),$$

where ρ is the air density and c_p is the specific heat capacity of air, the power requirement is between 3.5 and 6.5KW. In this calculation, the properties of air such as its specific heat capacity, thermal conductivity and density are assumed to be constants.

2.6 Conclusion

The purpose of the heat gun has been introduced, along with its physical structure and dimensions. In the next chapter, the design of the heat gun based on this structure will be presented.

Chapter 3

Structural Design of the Heat Gun

3.1 Introduction

The heat gun is required to deliver hot air with stringent temperature and velocity requirements where the temperature uniformity of the output air should be less than $\pm 0.5\,^oC$ for a range of temperature between $120\,^oC$ and $200\,^oC$. The velocity uniformity of the air should be no more than $\pm 1\,m/s$ within a region having a radius of $45\,mm$ and the velocity of the hot air has to be no less than $5\,m/s$. In this chapter, the structure of the heat gun will be designed to achieve these specifications.

The overview of the heat gun was presented in Chapter 2. The temperature and velocity profiles of the air at the outlet of the heat gun are studied in this chapter. As explained in Section 2.4, when the hot air moves through the pipe, the air temperature and velocity across the cross-section of the outlet will be non-uniform even though the input air has uniform temperature and velocity. A simple simulation was performed to verify this. A straight pipe with uniform inlet temperature and velocity of $200\,^oC$ and $5\,m/s$ respectively was simulated using FLUENT.

The initial parameters are shown in Table 3.1. Figure 3.1 shows the GAMBIT models. Figure 3.2(a) shows the temperature distribution at the pipe exit while Figure 3.2(b) shows the velocity profile of the air at the exit. From these figures, it can be observed that the layers of air which are at different radial distance away from the pipe wall are at different temperatures and velocities. The temperature uniformity for Figure 3.2(a) is $200 \pm 37.3189\ ^oC$, and the velocity uniformity for Figure 3.2(b) is $5 \pm 0.95\, m/s$ for up to $45\, mm$ in radial distance from the center.

For the heat gun to meet the design requirements on air temperature and velocity uniformity, the exit air temperature difference and the exit air velocity difference have to be reduced. In order to overcome the above challenges, studies on the effect of the insulation, material and length of the pipe are conducted. The use of the additional heat coil as well as the application of heat recycle will also be considered. These will be discussed in the rest of the chapter.

3.2 Design of the Pipe

In this section, the studies on the effect of the insulation materials of the pipe, the material of the pipe and the length of the pipe will be presented.

The mesh models of the pipes are built in GAMBIT and FLUENT is used to perform the simulations required. The model of the pipe in GAMBIT is shown in Figure 3.1, and the output results calculated in FLUENT are listed in Figure 3.2, where no insulation material is used and the length of the pipe is $220\, mm$. In the FLUENT simulations, the initial conditions are set as shown in Table 3.1 and steel is used as the material for the pipe. The use of steel will be examined in Section 3.2.2.

The temperature uniformity and the velocity uniformity for Figure 3.2 are $200 \pm 37.3189\ ^oC$ and $5 \pm 0.95\ m/s$, for up to $45\, mm$ in radial distance from the center, respectively. It is observed that the air temperature uniformity does not meet the

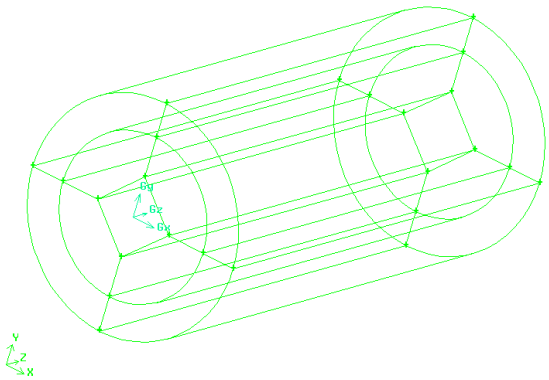

(a) Model of the pipe

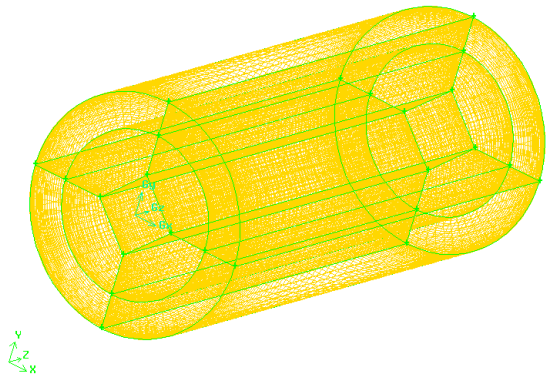

(b) Model of the pipe with mesh

Figure 3.1: Model of the heat gun's pipe in Gambit

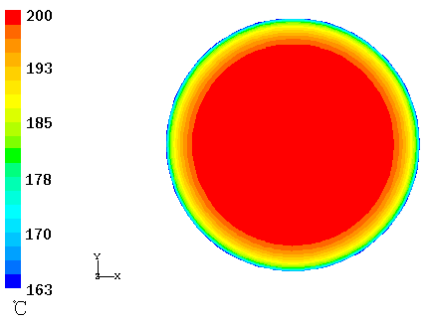

(a) Output air temperature

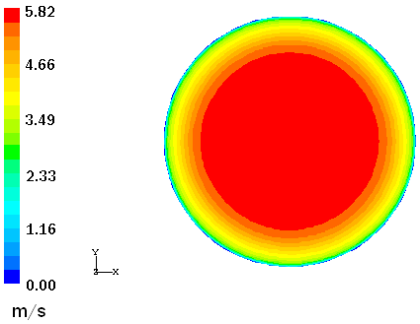

(b) Output air velocity

Figure 3.2: Output of the heat gun got from FLUENT

requirement while the air velocity uniformity meets.

Names	Initial values
Ambient temperature	27 ^oC
Air pressure	101325 $Pascal$
Air velocity of the pipe's inlet	5 m/s
Air temperature of the pipe's inlet	200 ^oC

Table 3.1: Initial conditions

3.2.1 Thermal Insulation Materials of the Pipe

It can be observed from Figure 3.2(a) that the maximum temperature difference at the exit of the pipe is 37.3189 ^oC. In this section, some insulation will be used to reduce the output temperature difference. Different insulation materials will be used to consider their effects.

The initial conditions of the air input into the pipe remain the same as in Table 3.1. The thickness of the insulation materials is set to 82 mm which will be discussed in Section 4.4. Thermal conductivities of some insulation materials simulated are listed in Table 3.2.

case no.	insulation material	thermal conductivity ($W/m \cdot ^o C$)
1	ash	0.071
2	calcium-surface	0.5
3	Shavings-Planner Maple, 16% Moisture	0.173
4	Shavings-Planner Red Wood Bark	0.0375

Table 3.2: Thermal conductivity of thermal insulation materials

In these four cases, the diameter and length of the pipe are kept at 100 mm and 220 mm respectively. Using FLUENT, the results are shown in Figure 3.3.

Figures 3.3(a), 3.3(c), 3.3(e) and 3.3(g) show the output air temperature and Figures 3.3(b), 3.3(d), 3.3(f) and 3.3(h) are the plots of the output air velocity for the four cases. As expected, the air velocities (see Figures 3.3(b), 3.3(d), 3.3(f) and 3.3(h)) are not affected by the type of insulation materials used. The air velocity uniformity is about $5 \pm 0.93\, m/s$ for up to 45 mm in radial distance from the center

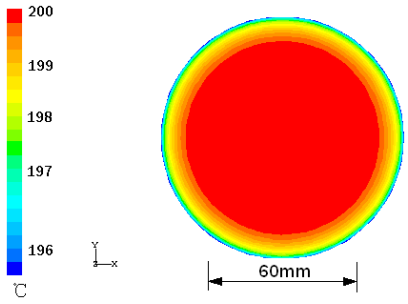

(a) Air temperature of case 1

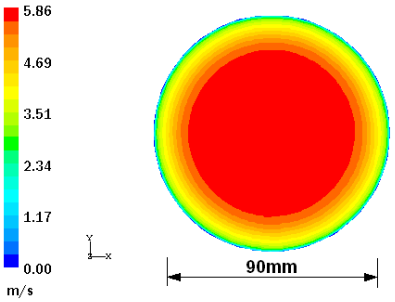

(b) Air velocity of case 1

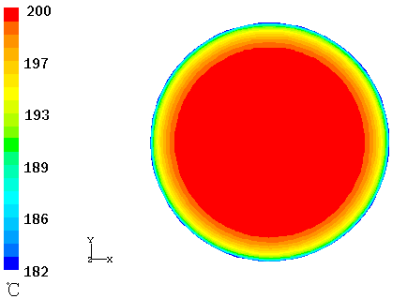

(c) Air temperature of case 2

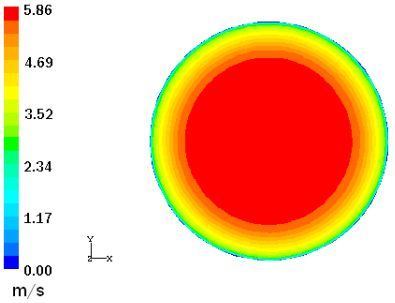

(d) Air velocity of case 2

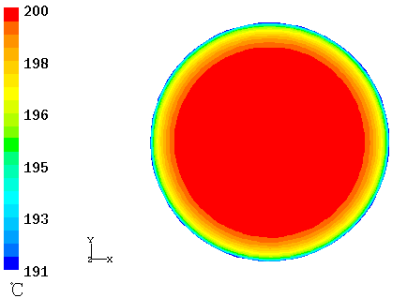

(e) Air temperature of case 3

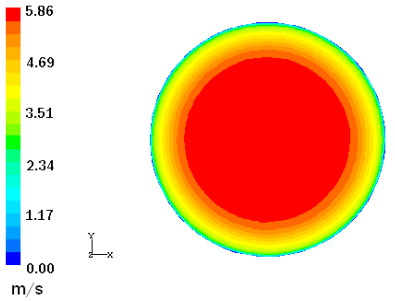

(f) Air velocity of case 3

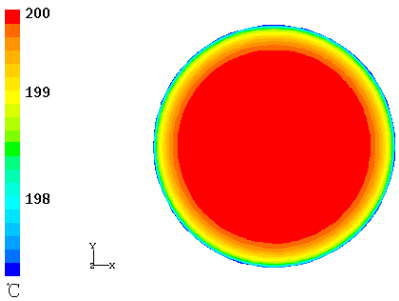

(g) Air temperature of case 4

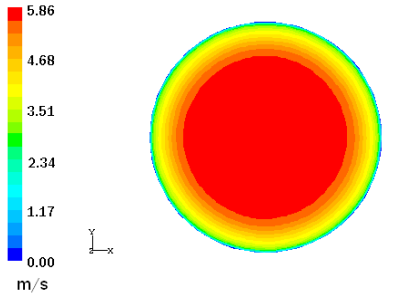

(h) Air velocity of case 4

Figure 3.3: Output air from the pipe by using different insulation materials

for all four cases.

The range of the output air temperature and velocity is listed in Table 3.3 and Table 3.4 respectively. From Table 3.3 and Figure 3.3, it is observed that

case no.	min output air temperature (^oC)	max output air temperature (^oC)	max temperature difference (^oC)
1	195.5488	200	4.4512
2	181.7898	200	18.2102
3	190.7486	200	9.2514
4	197.5074	200	2.4926

Table 3.3: Range of the output air temperature

case no.	output air velocity on the pipe wall (m/s)	min output air velocity within a radius of 45 mm to the center (m/s)	max output air velocity (m/s)
1	0.0	4.07	5.8564
2	0.0	4.05	5.8600
3	0.0	4.07	5.8578
4	0.0	4.07	5.8556

Table 3.4: Range of the output air velocity

the maximum difference of the output air temperature decreases as the thermal conductivity of the insulation decreases. In addition, the largest diameter of the circular area, where the output air temperature remain within 0.1 ^oC is about 60 mm for all cases. From Table 3.4 and Figure 3.3, it is found that the distributions of the output air velocities of these four cases are nearly the same.

Therefore, the insulation of shavings-planner red wood bark which has the smallest thermal conductivity of 0.0375 $W/m \cdot ^o C$ is chosen for the design. In the next section, the materials used for the pipe will be studied in detail.

3.2.2 Materials of the Pipe

In Section 3.2.1, it was found that the output air temperature is approximately constant for a radial length of $\pm 30\, mm$ from the center of the pipe. In this section,

the material for the pipe is changed to investigate their effect on the uniformity of the output air temperature.

The initial conditions of the air input into the pipes are listed in Table 3.1 and the pipes are uninsulated. The pipe materials are chosen as in Table 3.5. In these

case no.	material of the pipe wall	thermal conductivity $(W/m \cdot^o C)$
1	steel	54
2	aluminum	202.4
3	copper	387.6

Table 3.5: Pipe wall materials

three cases, the diameters and the lengths of the pipes are kept at $100\,mm$ and $220\,mm$ respectively.

The results from FLUENT are listed in Table 3.6 and Table 3.7. Figures 3.4(a), 3.4(c) and 3.4(e) show the output air temperature in all three cases. Figures 3.4(b), 3.4(d) and 3.4(f) are plots of the air velocity in all three cases. The plots show that all three cases are exactly the same for both the output air temperature and the output air velocity. From Table 3.6, Table 3.7, and Figure 3.4, it is observed

case no.	min output air temperature (^oC)	max output air temperature (^oC)	max temperature difference (^oC)
1	162.6811	200	37.3189
2	162.6801	200	37.3199
3	162.6798	200	37.3202

Table 3.6: The output air temperature of three cases

case no.	output air velocity on the pipe wall (m/s)	min output air velocity within a radius of $45\,mm$ to the center (m/s)	max output air velocity (m/s)
1	0.0	4.05	5.8191
2	0.0	4.05	5.8191
3	0.0	4.05	5.8191

Table 3.7: The output air velocity of three cases

that the difference of the output air temperature and velocity does not change

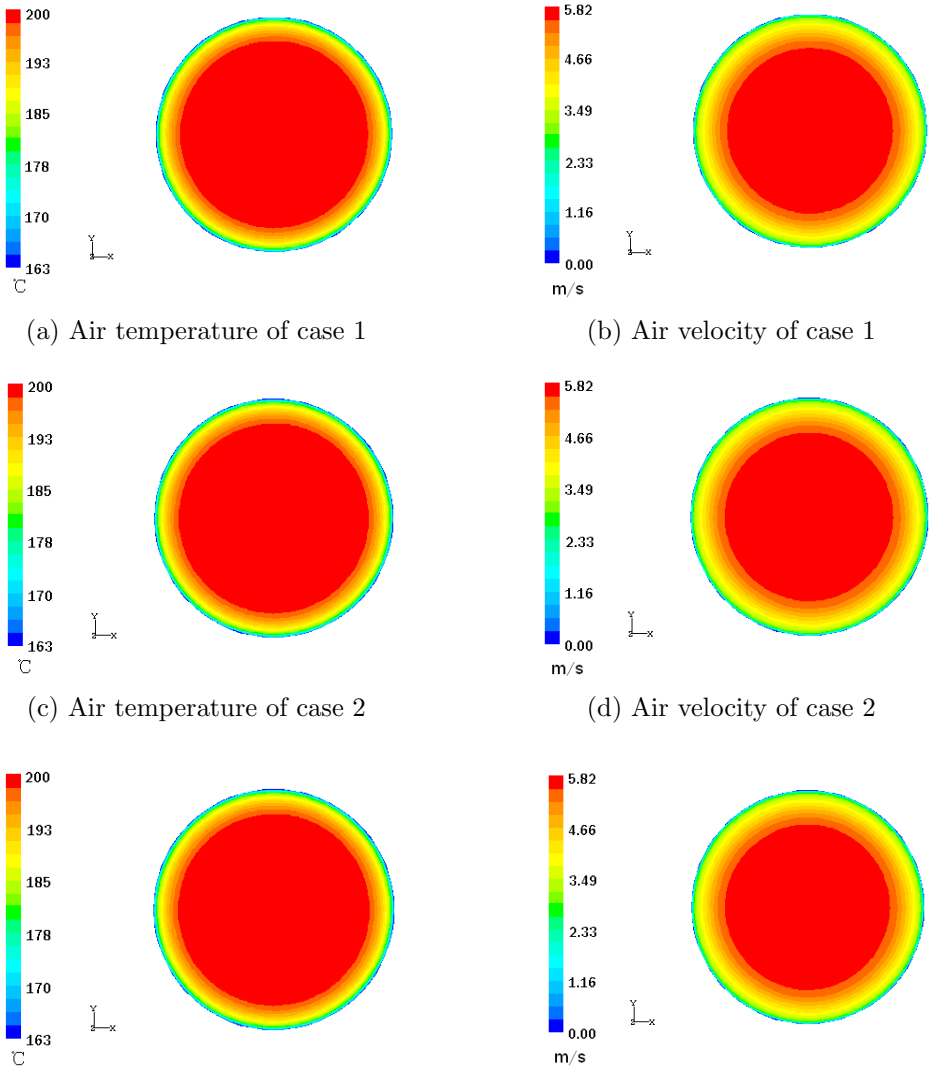

(a) Air temperature of case 1

(b) Air velocity of case 1

(c) Air temperature of case 2

(d) Air velocity of case 2

(e) Air temperature of case 3

(f) Air velocity of case 3

Figure 3.4: Output air from the pipe made of different materials

when the pipe material is changed. The largest diameter of the circular area, where the output air temperature remains within 0.1 ^oC, is about 60 mm which is also unchanged. The same output air temperature is obtained because the pipe wall is relatively thin and all materials of the pipe wall are good heat conductors compared to the thermal insulations shown in Table 3.2. The same air velocities for the three cases are expected because the same fluid, which is air, has been used in three cases. As the initial conditions of the input air for all three cases are the

same and the surface of the three metal pipes are set to be smooth, the movement of the air across the pipe is not affected by the change in the pipe materials

Thus, any one of the three materials can be used for the design of the heat gun. In the next section, the effect of the pipe length on the temperature and velocity uniformity will be examined.

3.2.3 Length of the Pipe

In this part, the length of the pipe will be determined. As can be expected, the longer the pipe, the more heat loss from the air inside the pipe to the pipe wall. In addition, due to the airflow over the heater coils, airflow through the pipe is initially expected to be turbulent. This pattern of airflow will affect the temperature uniformity at different sections of the pipe. Hence the length of the pipe plays an important role in ensuring a temperature uniformity that is achievable.

In this section, the heat gun model built in GAMBIT is shown in Figure 3.5. This heat gun has three rows of electric resistive coils (see Figures 3.5(c) and 3.5(d)), with nine circular coils evenly distributed from radial distances of $r = 3.6mm$ to $r = 46.2mm$ in each row (see Figures 3.5(b) and 3.5(d)). The cross-section of the coil wire is a $6mm \times 1mm$ rectangle (see Figure 3.5(d)). Three rows of coils are located along the pipe and they extend for 30 mm from the entrance of the pipe (see Figures 3.5(c) and 3.5(d)). The connection between the heat gun inlet and the pipe is a circular truncated cone instead of the sphere to simplify the generation of the mesh in GAMBIT for simulation. The cross-section of the heat gun inlet is circular with a radius of $100mm$. The height of the circular truncated cone is $100mm$. There is no insulation around the pipe. The inlet air velocity is set at 1.625 m/s so as to produce an average output air velocity of 6.5 m/s which satisfies the requirement that the output air velocity has to be greater than 5 m/s. The power input to the coils is $5300\,W$ and the ambient temperature is

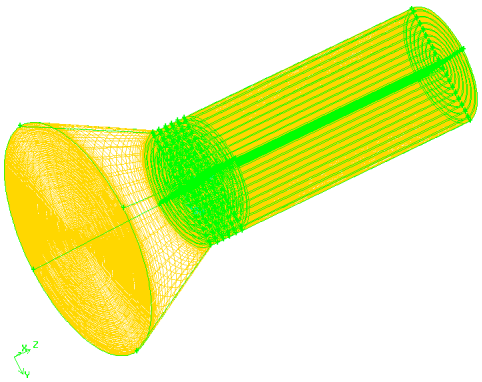

(a) Model of the heat gun in GAMBIT

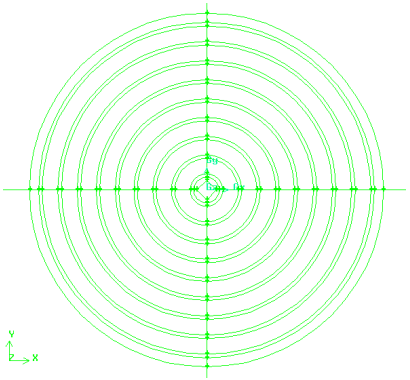

(b) Model of coils in GAMBIT

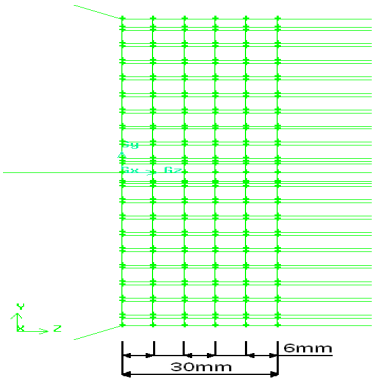

(c) Model of coils in GAMBIT

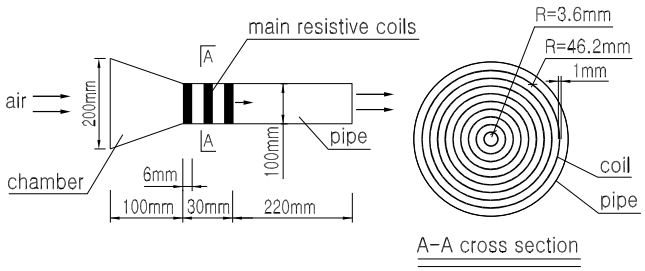

(d) Model of the heat gun in GAMBIT

Figure 3.5: Model of the heat gun in GAMBIT

$27\,^oC$ $(300K)$. The air temperature and velocity of the section located at the pipe length equal to $0.25\,m$ are shown in Figures 3.6(i) and 3.6(j).

The air temperature and velocity of the sections along the different lengths of the pipe are shown in Figure 3.6. From Figure 3.6, it is found that the largest

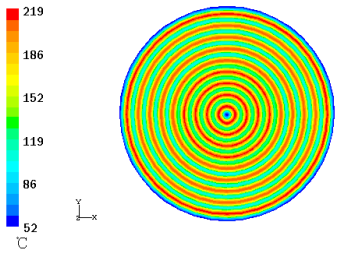

(a) Air temperature at Length=0.05m

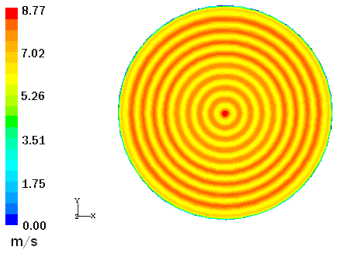

(b) Air velocity at Length=0.05m

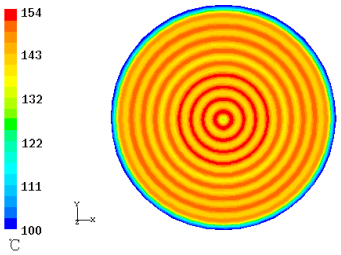

(c) Air temperature at Length=0.10m

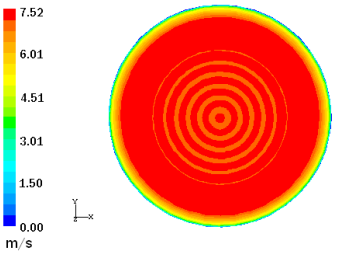

(d) Air velocity at Length=0.10m

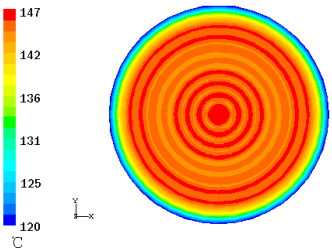

(e) Air temperature at Length=0.15m

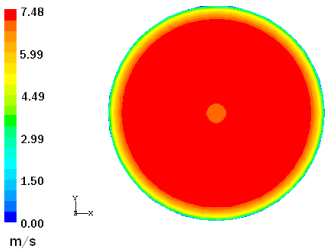

(f) Air velocity at Length=0.15m

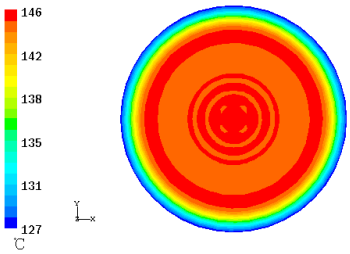

(g) Air temperature at Length=0.20m

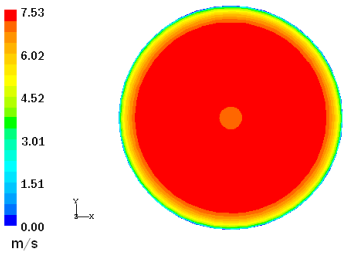

(h) Air velocity at Length=0.20m

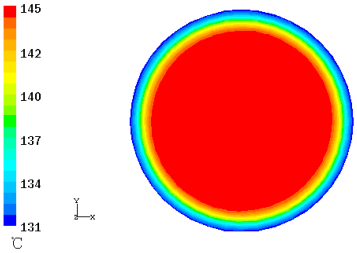

(i) Air temperature at Length=0.25m

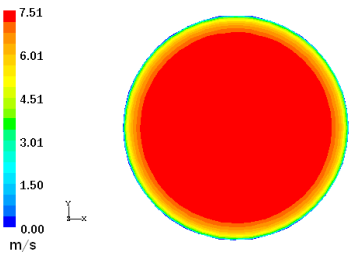

(j) Air velocity at Length=0.25m

Figure 3.6: Output air temperature and velocity at different lengths

difference in air temperature is when air just passes through the coils which are located up to 0.03 m from the entrance of the pipe. This difference becomes smaller and the uniformity improves as air flows further through the pipe. At a distance of 0.25 m from the entrance, the temperature distribution becomes much more uniform (see Figure 3.6(i)). The air temperature uniformity is less than $\pm 0.5^oC$ for up to 40 mm radius. If the length of the pipe is 250 mm, the output air velocity distribution is acceptable as can be seen from Figure 3.6(j) where the velocity uniformity is no more than $\pm 0.93\, m/s$ for up to 45 mm in radial distance from the center. When the input power to the coils is set at 5300 W and the inlet air

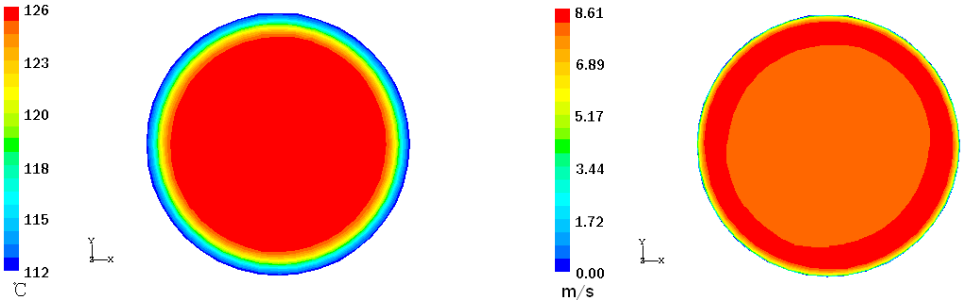

(a) Output air temperature (b) Output air velocity

Figure 3.7: Output air with the large velocity

velocity is increased to 1.8 m/s which is used to get the average output air velocity of 7.2 m/s, the output air temperature and velocity is shown in Figure 3.7 where the length of the pipe is kept at 0.25 m. From Figure 3.7(a), it is observed that the air temperature uniformity is less than $\pm 0.4^oC$ for up to 41 mm in radial distance from the center. From Figure 3.7(b), it is observed that the largest difference in the air velocity is 1.39 m/s for up to 45 mm in radial distance from the center.

3.2.4 Design Summary for the Pipe

From the above sections, the pipe of the heat gun is chosen to be insulated by shavings-planner red wood bark with a low thermal conductivity of $0.0375\, W/m{\cdot}^oC$

and 250 mm in length inclusive of the 30 mm length of the coil-net. In the next section, the use of the additional heat coil will be examined to further improve the temperature uniformity of the output air.

3.3 Additional Coil

In case 4 of Section 3.2.1, we found that the temperature uniformity is $200 \pm 2.4926\ ^oC$ and the velocity uniformity is $5 \pm 0.93\ m/s$ for up to 45 mm in radial distance from the center. The velocity uniformity satisfies the design requirement but the temperature uniformity needs to be further improved. In this section, some improvements will be made to reduce the temperature difference.

From the previous simulation results, it is observed that the air temperature drop significantly near the pipe wall. This area is the thermal boundary layer where a temperature gradient exists because of the heat transfer between the air inside the pipe and the pipe wall. To compensate for the loss, an additional section of heater coil is added at a suitable distance away from the exit. This is shown in Figure 3.8.

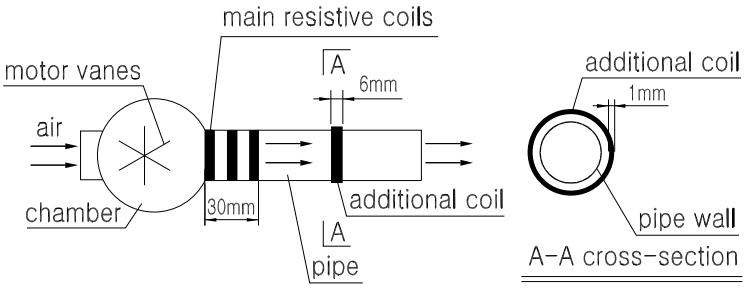

Figure 3.8: Additional coil

The location of the additional coil can be determined as follows. Different locations of the additional coil are tested using FLUENT and GAMBIT. These locations of the additional coil are from the beginning of the pipe to the end of

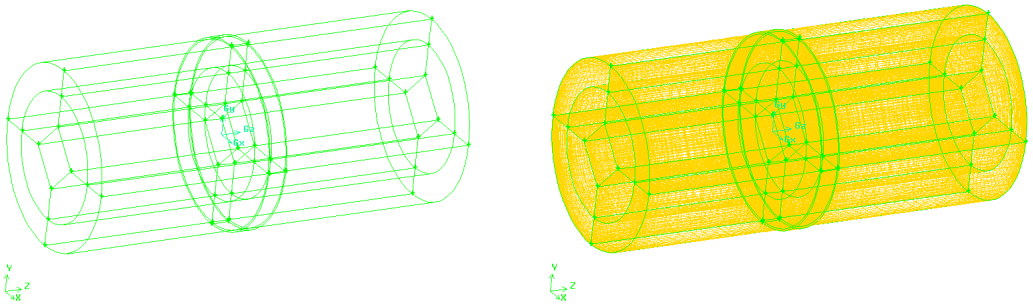

(a) Additional coil model (b) Mesh model of the additional coil

Figure 3.9: Model of the additional coil in GAMBIT

the pipe at intervals of $0.02\,m$. Here, the beginning of the pipe refers to the end of the main resistive coils. The inner radius and outer radius of the additional coil are $50\,mm$ and $51\,mm$ respectively. The cross-section of the additional coil wire is a $6mm \times 1mm$ rectangle where $6mm$ is along the pipe's length (see Figure 3.8). The model of the additional coil in GAMBIT is shown in Figure 3.9 where the location of the additional coil is in the middle of the pipe. The temperature of the air input to the pipe is set at $140\,^oC$, the velocity of the input air is $5\,m/s$ and the input power to the additional coil is $6\,W$ which will be justified in Section 4.5. When the additional coil is not used, the output air temperature and velocity obtained using FLUENT is as shown in Figure 3.10. The output air temperature uniformity is $140 \pm 1.5\,^oC$. The velocity uniformity is $5 \pm 0.89\,m/s$ (see Figure 3.10) for up to $45\,mm$ in radial distance from the center. When the additional coil is used, the output air temperature and velocity obtained from FLUENT is shown in Figure 3.11 where the distance between the end of the main coils and the beginning of the additional coil is 0.1 m. The output air temperature uniformity is $140 \pm 0.3\,^oC$. The velocity uniformity is $5 \pm 0.9\,m/s$ (see Figure 3.11) for up to $45\,mm$ in radial distance from the center. The use of the addition coil has improved the temperature uniformity. Velocity uniformity is still acceptable by the design requirements. The output air temperature with the additional coil

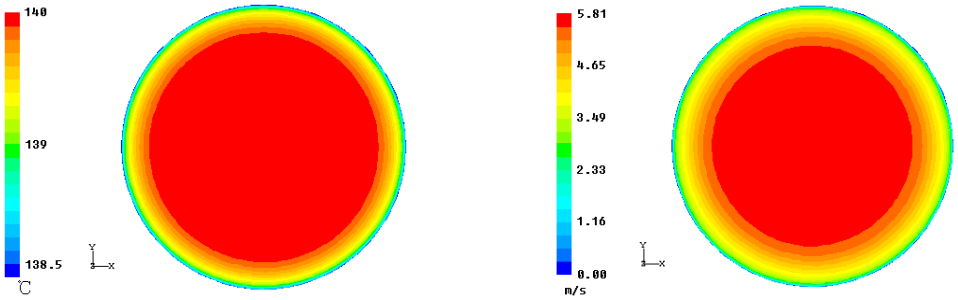

(a) Output air temperature (b) Output air velocity

Figure 3.10: Output air without the additional coil

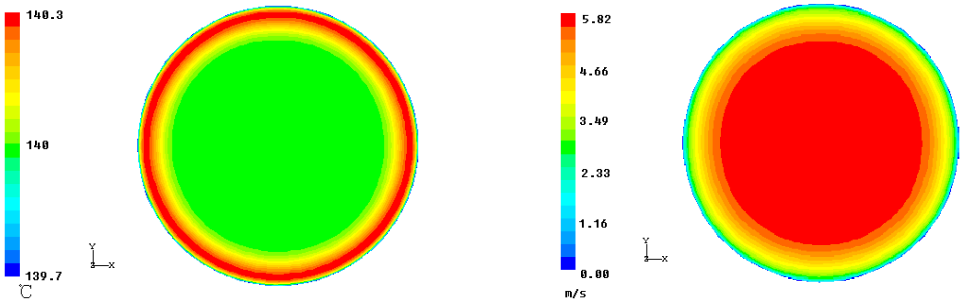

(a) Output air temperature (b) Output air velocity

Figure 3.11: Output air with the additional coil

located at different locations is shown in Figure 3.12(a). Figure 3.12(b) is a partial amplification of Figure 3.12(a).

The temperature along the exit diameter is shown in Figure 3.12 where the "*Distance*" in the legend is the distance from the end of the main resistive coils and the beginning of the additional coil. In Figure 3.12, it is shown that when the additional coil is further away from the main coils, both ends of the curves are much higher. This indicates that the air temperature near the pipe is higher when the additional coil is nearer the exit of the pipe.

The maximum and minimum output air temperatures corresponding to the different locations of the additional coil are shown in Figure 3.13 where x-axis shows the distance from the starting point of the additional coil to the inlet of the pipe. The two horizontal lines represent the maximum and the minimum output

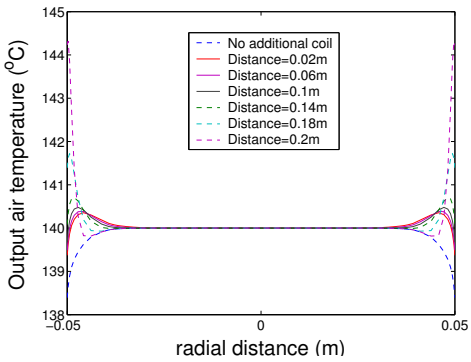

(a) Output air temperature

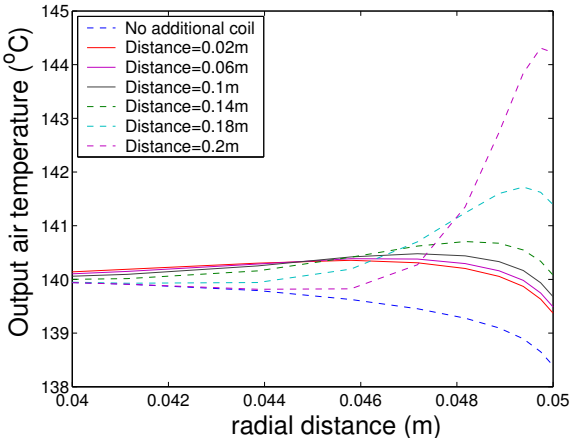

(b) Output air temperature

Figure 3.12: Comparison of the output air temperature

air temperatures without the additional coil. From Figure 3.12 and Figure 3.13, it

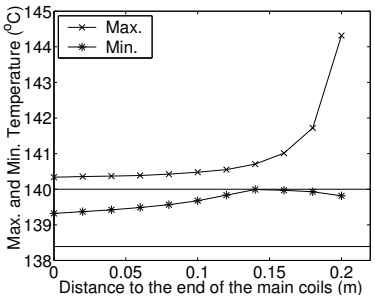

Figure 3.13: Maximum and minimum output air temperature

is observed that the temperature uniformity of the output section is the smallest and less than 0.5 ^oC if the additional coil is located at 0.1 m after the end of the

main resistive coils. When no additional coil is used, the temperature uniformity at the exit is $140 \pm 1.5\ ^oC$. Thus the temperature uniformity is improved by using the additional coil.

Thus, the two groups of coils, the main resistive coils and the additional coil, can be used together to produce more uniform air temperature across the exit. The power supplies to the two groups of coils are controlled separately to get the desired results. This will be discussed in Chapter 4.

In the next section, heat recycling will be explored.

3.4 Heat Recycle

As the heat gun is required to output air at a high temperature and velocity, a high power input to its resistive coils is required. The power (Holman, 1988) needed to heat the air from ambient temperature, T_0 (^oC), to a high temperature, T (^oC), is given by

$$P = \rho c_p \upsilon A(T - T_0) \tag{3.1}$$

where ρ = density of air (kg/m^3),

c_p = specific heat of air ($J/kg \cdot^o C$),

υ = air velocity (m/s),

A = cross-section area of the exit (m^2).

The cross-section area of the exit for the heat gun is $7.85 \times 10^{-3}\, m^2$. ρ and c_p are $0.8826\, kg/m^3$ and $1014\, J/kg \cdot^o C$ respectively at a temperature of $140\, ^oC$. According to the design specifications, the air velocity has to be greater than $5\, m/s$ and heated from $27\, ^oC$ to $140\, ^oC$. From (3.1), if the air with a velocity of $5\, m/s$ is needed to heat from $27\, ^oC$ to $140\, ^oC$, the required power is $3970\, W$. From Section 3.2.3, it was found that the air temperature is only raised from $27\, ^oC$ to $145\, ^oC$

with the output air velocity of $6.5\,m/s$ when the input power to the coils is $5300\,W$. This shows that a very high input power is required in this design.

In order to reduce the power consumption, a circulation path is created which transfers the output hot air from the heat gun back to the input of the heat gun for reuse. The schematic diagram of the heat gun with the heat recycle is shown in Figure 3.14. The diameters of the outlet and inlet of the recycle pipe are equal to that of the heat gun's pipe outlet . If the energy efficiency coefficient of the

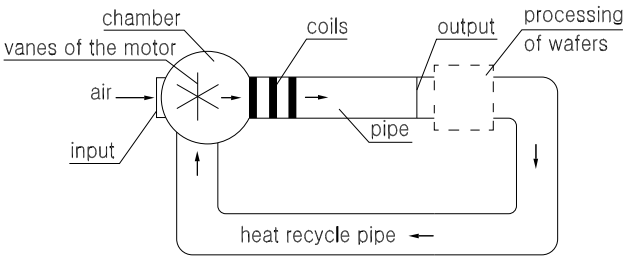

Figure 3.14: Heat gun with the heat recycle

recycle is 0.7, the above required power of $3970\,W$ and $5300\,W$ will be greatly decreased because the power returned by the heat recycle are $3442\,W$ and $4635\,W$ respectively according to (3.2).

$$P = 0.7\rho c_p \upsilon AT \tag{3.2}$$

The efficiency coefficient of the recycle is closely related to the insulation of the recycle pipe if the recycle pipe is well sealed (see Section 4.6). Hence the heat recycle will improve the energy efficiency if the recycle pipe is well insulated and sealed. Further analysis of the heat recycling will be given in Section 4.6

3.5 Conclusion

In this chapter, the structure of the heat gun was discussed. Detailed parameters of the pipe, the insulation material and the length, were investigated using FLUENT and GAMBIT. In addition, the installation of an additional coil was proposed to improve uniformity. The positioning of this coil was also investigated. Finally, heat recycle was introduced to improve energy efficiency.

Chapter 4

Modeling of the Heat Gun

4.1 Introduction

In this chapter, the heat gun is modelled for the purpose of analysis and control in the later chapters. According to Chapters 1 and 3, the main process of heating air can be divided into three steps. Firstly, air is sucked into the chamber of the heater by a rotating DC motor. Secondly, air is heated by the main electric resistive coils. Finally, air passes through the pipe and exits as heated air with a certain temperature. The heated air also satisfies certain temperature and velocity uniformity requirements. In this heat gun, air near the exit of the pipe is reheated by the additional coil to offset the heat loss during the air transfer in the pipe. Heat recycle is also considered. Each of these steps is modelled in the following sections.

4.2 Modeling of the DC Motor

DC motors are extremely versatile drives, capable of reversible operation over a wide range of speeds, with accurate control of the speed at all times. They can be controlled smoothly from zero speed to full speed in both directions. DC motors

have a high torque-to-inertia ratio that gives quick response to control signals. And for elaborate control, DC signal computation is easier than that of AC signal (D'Azzo and Houpis, 1981). Therefore, in this project, a DC motor is selected to drive the air through the heater pipe.

Figure 4.1 is a schematic diagram of an armature-controlled DC motor, where the circuit on the left generates the magnetic field and the circuit on the right generates the output torque.

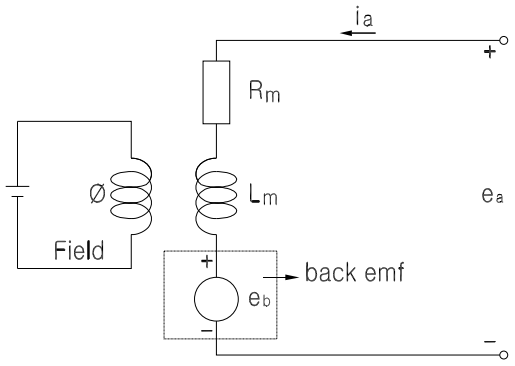

Figure 4.1: Schematic diagram of a DC motor

A variable voltage e_a (V) is applied to the armature winding.

Equation (4.1) shows the back emf, $e_b(t)$, generated from the motor speed measured by the tachogenerator.

$$e_b(t) = K_E \omega(t) \tag{4.1}$$

where K_E is the feedback constant $(V \cdot s/rad)$, and ω is the rotation speed of the DC motor in rad/s.

Taking Laplace transform and assuming zero initial conditions, we have

$$E_b(s) = K_E \Omega(s) \ . \tag{4.2}$$

With the back emf, the resulting armature current, $i_a(t)$ satisfies the following

relationship:

$$e_a(t) = L_m \frac{di_a}{dt} + R_m i_a(t) + e_b(t) \tag{4.3}$$

where L_m is the armature inductance, and R_m is the armature resistance.

Taking Laplace transform with zero initial conditions,

$$E_a(s) = L_m s I_a(s) + R_m I_a(s) + E_b(s) \tag{4.4}$$

or

$$I_a(s) = [E_a(s) - E_b(s)](\frac{1}{R_m + L_m s}) \ . \tag{4.5}$$

It is well known that the relationship between the armature current, i_a, and the torque, T_{or} $(N \cdot m)$, produced by the DC motor is given by

$$T_{or}(t) = K_T i_a(t) \tag{4.6}$$

where K_T $(N \cdot m/A)$ is the torque constant. The corresponding Laplace transform is as follows

$$T_{or}(s) = K_T I_a(s) \ . \tag{4.7}$$

With Newton's law of motion, we have

$$J \frac{d\omega(t)}{dt} = \Gamma(t) \tag{4.8}$$

where J $(N \cdot m \cdot s^2/rad)$ is the inertia of the motor and its load, and $\Gamma(t)$ $(N \cdot m)$ is the net torque given by

$$\Gamma(t) = T_{or}(t) - T_{load}(t) - B\omega(t) \tag{4.9}$$

where B ($N \cdot m \cdot s/rad$) is a constant related to the viscous friction. Therefore,

$$J\frac{d\omega(t)}{dt} = T_{or}(t) - T_{load}(t) - B\omega(t)\,. \tag{4.10}$$

The corresponding Laplace transform of (4.10) with zero initial conditions is as follows,

$$Js\Omega(s) = T_{or}(s) - T_{load}(s) - B\Omega(s)\,, \tag{4.11}$$

or

$$\Omega(s) = \frac{T_{or}(s) - T_{laod}(s)}{Js + B}\,. \tag{4.12}$$

The block diagram of an armature-controlled DC motor is illustrated in Figure 4.2, where T_{load} is modelled as a disturbance.

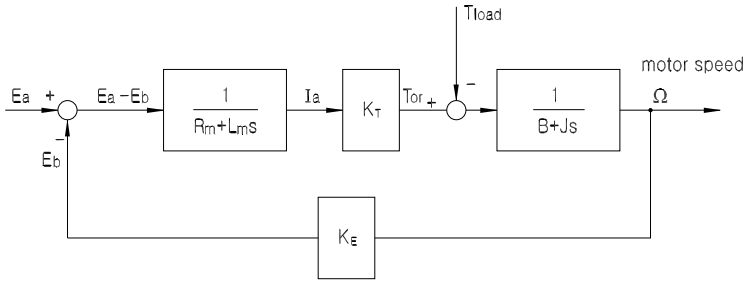

Figure 4.2: Block diagram of the DC motor

From the equations above, the transfer function of the DC motor's rotational speed is given by

$$\begin{aligned}\Omega(s) =& \frac{K_T}{L_m J s^2 + (R_m J + B L_m)s + K_E K_T + R_m B} E_a(s) \\ & - \frac{R_m + L_m s}{L_m J s^2 + (R_m J + B L_m)s + K_E K_T + R_m B} T_{load}(s)\,.\end{aligned} \tag{4.13}$$

If T_{load} is very small, then (4.13) becomes

$$\Omega(s) = \frac{K_T}{L_m J s^2 + (R_m J + B L_m)s + K_E K_T + R_m B} E_a(s)\,. \tag{4.14}$$

The velocity of air driven by the motor can further be written as

$$\upsilon_a(s) = k_n\Omega(s) = \frac{k_n K_T}{L_m J s^2 + (R_m J + B L_m)s + K_E K_T + R_m B} E_a(s) \qquad (4.15)$$

where k_n is a coefficient determined by the shape of the motor vanes. Here, the length of the motor vane is selected as $4cm$. The average υ_a with respect to the length of the vane is given by

$$\frac{1}{0.04}\int_0^{0.04} \upsilon_a dx = \frac{1}{0.04}\int_0^{0.04} 2\pi x \frac{\omega}{2\pi} dx = 0.02\omega \ . \qquad (4.16)$$

Using the value of the average υ_a to substitute the value of υ_a, we obtain $k_n = 0.02$.

An example of a permanent-magnet armature-controlled DC motor[1] has coefficients shown in Table 4.1. The DC motor can drive the air to the rated velocity of $10.472\,m/s$ with $k_n = 0.02$.

Rated speed ω_{max}	$523.6\,(rad/s)$ or $5000\,(r/min)$
Rated armature current I	$21\,(A)$
Feedback constant K_E	$0.18\,(V \cdot s/rad)$
Torque constant K_T	$0.18\,(N \cdot m/A)$
Armature resistance R_m	$0.5\,(\Omega)$
Armature inductance L_m	$0.0092\,(H)$
Armature moment of inertia J	$1.573\times10^{-2}\,(N \cdot m \cdot s^2)$
Armature viscous friction B	$1.0\times10^{-4}\,(N \cdot m \cdot s/rad)$

Table 4.1: Parameters of a DC motor

Using these coefficients, the transfer function in (4.14) becomes

$$\frac{\Omega(s)}{E_a(s)} = \frac{180}{0.1447s^2 + 7.866s + 32.45} \ . \qquad (4.17)$$

[1]It is produced by Shanghai JUFENG LTD.

4.3 Modeling of the Main Electric Resistive Coils

In this heat gun, the main electric resistive coils are placed at the inlet of the pipe which connects to the chamber which houses the DC motor vanes. Air driven by the motor flows over the heated coils and passes through the pipe. Figure 4.3(a)

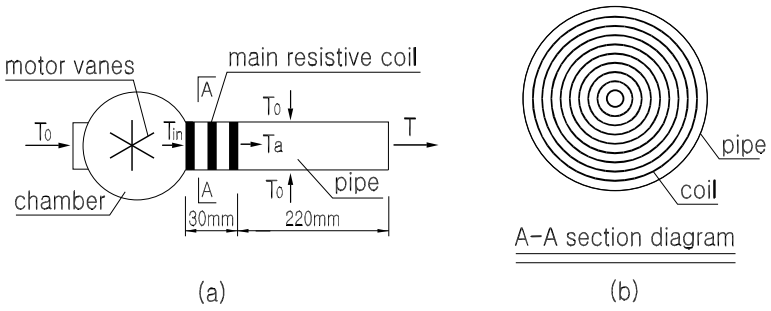

Figure 4.3: Modeling of the main electric resistive coils

shows the schematic diagram of the overall heater. Figure 4.3(b) displays the A-A cross-sectional view. In the modeling of the coils, it is assumed that the air is an incompressible ideal gas. The input air temperature before the hot coils is T_{in} and the output air temperature after the hot coils is T_a. It is known that the closer the air approaches the coils, the higher the air temperature. In this heater, the required air velocity is greater than $5\,m/s$, and the thermal conductivity of air is very small. So compared to the temperature T_a, the difference between T_{in} and the ambient temperature, T_0, should be small and this difference can be neglected. We thus assume that T_{in} equals the ambient temperature, T_0.

A diagram modeling the main resistive coils is presented in Figure 4.4. The layout of these main resistive coils is given in Chapter 3. As mentioned there, the coils are evenly spread from the entrance of the pipe to $30\,mm$ further away along the pipe. If this part of the pipe is well insulated, a mathematical model of the temperature of the air can be developed using the energy conservation law

(Holman, 1988) in the control volume (see Figure 4.4) as follows:

$$P_{in} - \frac{d(E_o - E_i)}{dt} = \frac{dE}{dt} \tag{4.18}$$

where P_{in} = power input to coils (W),

E = internal energy of coils and air in the control volume (J),

E_o = energy out of the control volume taken by air (J),

E_i = energy into the control volume taken by air (J).

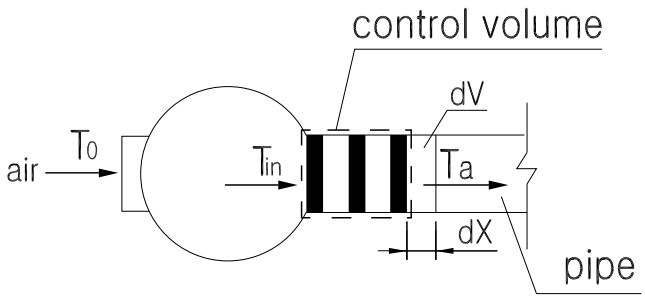

Figure 4.4: Analysis of the main electric resistive coils

Supposing that air is an ideal gas and air in the control volume is mixed well, then the air temperature in the control volume is equal to the air temperature at the output of the control volume. Considering the boundary of the control volume, the rate of transfer of energy, which is taken out from the control volume by air whose initial temperature is T_{in}, is given by

$$\frac{d(E_o - E_i)}{dt} = \dot{m}_a c_{pa}(T_a - T_{in}) \tag{4.19}$$

where c_{pa} = specific heat of air $(J/kg.^oC)$,

T_a= air temperature in the control volume (^oC),

T_{in} = air temperature at the inlet of the control volume (^oC),

$\dot{m}_a$ = air mass flow rate through the control volume(kg/s).

T_{in} is constant because it is assumed that T_{in} is approximately equal to the ambient temperature, T_0.

It is known that

$$\dot{m}_a = \rho_a \frac{dV}{dt} = \rho_a Q_a \tag{4.20}$$

and

$$Q_a = \frac{dV}{dt} = k_a \frac{dX}{dt} = k_a \upsilon_a \tag{4.21}$$

where Q_a = air flow rate (m^3/s), which is determined by the air velocity,

υ_a = air velocity (m/s),

dV = the volume of the air out of the control volume during the time interval dt (m^3),

dX = the distance travelled by the air out of the control volume during the time interval dt (m),

k_a = cross sectional area of the control volume (m^2).

The internal energy change in the control volume, which includes coils and air, is given by

$$\frac{dE}{dt} = \rho_a V_a c_{pa} \frac{dT_a}{dt} + \rho_r V_r c_{pr} \frac{dT_r}{dt} \tag{4.22}$$

where ρ_a = density of air (kg/m^3), assumed constant,

ρ_r = density of coils (kg/m^3),

T_r= temperature of coils (^oC),

V_a = volume of the space (air) exclusive of coils in the control volume (m^3),

V_r = volume of coils (m^3),

c_{pr} = specific heat of coils ($J/kg.^oC$).

Substituting (4.19) and (4.22) into (4.18), we obtain

$$P_{in} = \rho_a V_a c_{pa} \frac{dT_a}{dt} + \rho_r V_r c_{pr} \frac{dT_r}{dt} + \dot{m}_a c_{pa}(T_a - T_{in}) \ . \tag{4.23}$$

Rewriting (4.23),

$$P_{in} = \rho_a V_a c_{pa} \frac{dT'_a}{dt} + \rho_r V_r c_{pr} \frac{dT'_r}{dt} + \dot{m}_a c_{pa} T'_a \tag{4.24}$$

where $T'_a = T_a - T_{in} \approx T_a - T_0$ (^oC),

$T'_r = T_r - T_{in} \approx T_r - T_0$ (^oC),

T_0 = ambient temperature (^oC),

Applying conservation of energy to the resistive coils (Kreith and Bohn, 1986), we have

$$P_{in} - \bar{h} A_r (T_r - T_a) = V_r c_{pr} \rho_r \frac{dT_r}{dt} \tag{4.25}$$

where $\bar{h} A_r (T_r - T_a)$ = the heat transferred from the coils to the air mainly by convection and ignoring radiation,

$\bar{h}$ = mean convective heat transfer coefficient ($W/m^2.^oC$),

A_r = surface area of the resistive coils (m^2).

Equation (4.25) can then be written as

$$P_{in} - \bar{h} A_r (T'_r - T'_a) = V_r c_{pr} \rho_r \frac{dT'_r}{dt} \ . \tag{4.26}$$

Taking Laplace transform of (4.24) and (4.26) and rearranging after eliminating $T'_r(s)$, we obtain

$$\frac{T'_a(s)}{P_{in}(s)} = \frac{\bar{h} A_r}{(\rho_a V_a c_{pa} \rho_r V_r c_{pr}) s^2 + (\rho_a V_a c_{pa} \bar{h} A_r + \rho_r V_r c_{pr} \bar{h} A_r + \rho_a Q_a c_{pa} \rho_r V_r c_{pr}) s + \rho_a Q_a c_{pa} \bar{h} A_r} \ . \tag{4.27}$$

Furthermore,

$$P_{in} = I^2 R \tag{4.28}$$

where I = current in the resistive coils (A),

R= resistance of resistive coils (Ω).

Accordingly, the transfer diagram from I to T_a is shown in Figure 4.5.

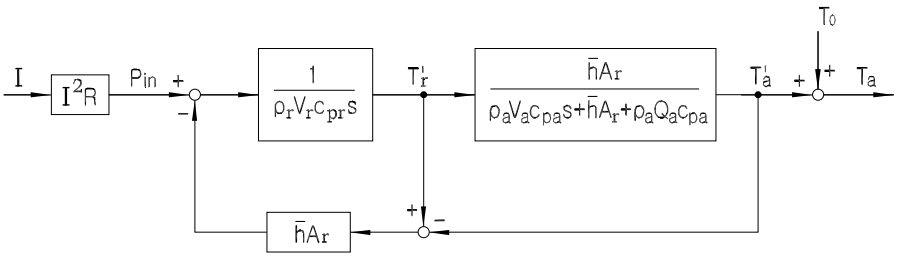

Figure 4.5: Transfer diagram of the main resistive coils

In practice, we often choose a material with high electrical resistivity as the heater coils. An example of such material is Fe-Cr-Al. The characteristics of this material is shown in Table 4.2. In this project, the output cross sectional area of the control volume is $7.85 \times 10^{-3} m^2$ because the radius of the control volume is $50mm$. Hence $k_a = 7.85 \times 10^{-3}\ m^2$.

Main chemical composition	Cr 12-15% Al 4.0-6.0% Fe rest
Maximum continuous service temperature	1200^oC
Melting point	1500^oC
Resistivity at 20^oC	$1.25 \pm 0.08 (\Omega.mm^2/m)$
Density	$7.3\ g/cm^3$
Specific heat	$0.49 (KJ/kg.^oC)$
Coefficient of thermal conductivity	$14.65 (W/m.^oC)$
Length	$4.5\ m$
Diameter	$0.5\ mm$

Table 4.2: Characteristics of Fe-Cr-Al resistive coil

If the resistive wire in the control volume is $4.5\,m$ long with a cross-section as

a rectangle of $6mm \times 1mm$, we obtain

the surface area of the coils: $A_r = 0.063\ (m^2)$

the volume of the coils: $V_r = 2.7 \times 10^{-5}\ (m^3)$,

the air space in the control volume: $V_a = 2.0862 \times 10^{-4}(m^3)$.

If the ambient temperature is assumed to be 24 (^oC),

the density of air, $\rho_a = 1.1774\ (kg/m^3)$ and

the specific heat of air, $c_{pa} = 1006\ (J.kg/^oC)$.

Substituting numerical values into (4.27) and choosing $\bar{h} = 25\ W/m^2.^oC$ which is a typical convection coefficient (Holman, 1997), we get

$$\frac{T_a'(s)}{P_{in}(s)} = \frac{1.575}{23.865s^2 + (152.501 + 897.996\upsilon_a)s + 14.644\upsilon_a}\ . \tag{4.29}$$

4.4 Modeling of the Heat Transfer in the Pipe

As the air flows over the heated coils, it heats up according to (4.29). This hot air then passes through the pipe of the heat gun, and in so doing, heat is transferred onto the pipe's wall. There is thus heat loss from the hot air. In order to reduce the heat loss from the hot air inside the pipe to the surrounding air outside the pipe, some insulation is mounted around the outside wall of the pipe. The schematic diagram for this process is shown in Figure 4.6.

From the basic law of heat transfer, it is known that the heat loss from the inner radius of the pipe to the outer surface of the insulation for an element of length, dl, of the pipe is given by

$$dq = \frac{T_1 - T_2}{\Sigma R_d} \tag{4.30}$$

where dq = differential heat flow through an element of length, dl (W),

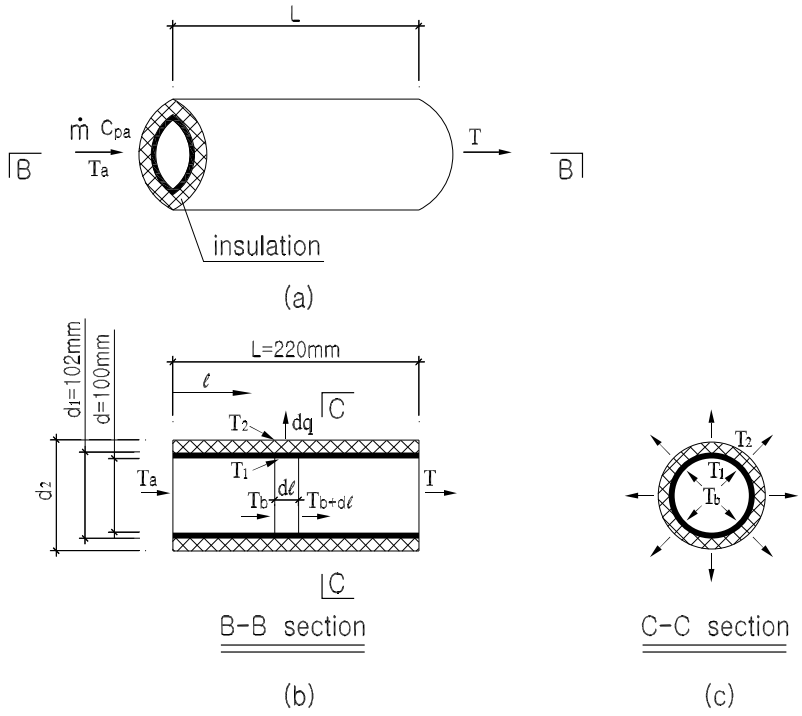

Figure 4.6: Modeling of the heat transfer in the insulated pipe

T_1 = temperature of inner surface of the pipe (^oC),

T_2 = temperature of outer surface of the pipe's insulation (^oC),

ΣR_d = total differential thermal resistance from the inner radius of the pipe to the outer surface of the insulation along the length of dl ($^oC/W$).

ΣR_d is composed of two parts. One is the thermal conductivity resistance of the pipe, while another is the thermal conductivity resistance of the insulation.

Therefore,

$$\Sigma R_d = \frac{ln(d_2/d_1)}{2\pi k_m dl} + \frac{ln(d_1/d)}{2\pi k dl} \tag{4.31}$$

where d = inner diameter of the pipe (m),

d_1 = outer diameter of the pipe and inner diameter of the cylindrical insulation (m),

d_2 = outer diameter of the cylindrical insulation (m),

k_m = thermal conductivity of the insulation $(W/m \cdot^o C)$,

k = thermal conductivity of the pipe $(W/m \cdot^o C)$.

In the pipe, it can be assumed that the temperature of air inside the pipe equals the temperature of the inner surface of the pipe along the axial length. That is $T_1 = T_b$, where T_b =bulk temperature (^oC) of air flow inside the pipe at the location l.

Then (4.30) can be written as follows:

$$dq = -\frac{2\pi(T_b - T_2)}{\frac{ln(d_2/d_1)}{k_m} + \frac{ln(d_1/d)}{k}} \cdot dl \ . \tag{4.32}$$

The minus sign signifies heat loss.

In the axial direction of the pipe, the heat loss along the differential length of the pipe can also be expressed as follows:

$$dq = \dot{m} c_{pa} dT_b \tag{4.33}$$

where c_{pa} = specific heat of air $(J/kg \cdot^o C)$,

$\dot{m}$ = mass flow rate(kg/s).

$$\dot{m} = \rho_a \upsilon_a \frac{\pi d^2}{4} \tag{4.34}$$

where υ_a = air velocity (m/s),

d = inner diameter of the pipe (m),

ρ_a = density of air (kg/m^3).

Combining (4.32), (4.33) and (4.34), we have

$$-\frac{2\pi(T_b - T_2)}{\frac{ln(d_2/d_1)}{k_m} + \frac{ln(d_1/d)}{k}} \cdot dl = \rho_a \upsilon_a c_{pa} \frac{\pi d^2}{4} dT_b \ . \tag{4.35}$$

Solving (4.35) and using the boundary conditions, where $l = 0$, $T_b = T_a$, the solution of T_b is given by

$$T_b = T_a e^{-l/C} + (1 - e^{-l/C})T_2 \tag{4.36}$$

where $C = (\frac{ln(d_2/d_1)}{2\pi k_m} + \frac{ln(d_1/d)}{2\pi k})\rho_a \upsilon_a c_{pa} \frac{\pi d^2}{4}$, is a constant. If υ_a goes to zero, it means that there is no air flow, thus there is no heat transferred by convection. Thus T_b approaches T_2 if υ_a goes to zero. At the same time, T_2 will be equal to the ambient temperature, T_0, since there is no hot air flow at all.

At $l = L$, the expression of the exit temperature, T, across the outlet section of the pipe is

$$T = T_a e^{-L/C} + (1 - e^{-L/C})T_2 \ . \tag{4.37}$$

Equation (4.37) gives the steady state output temperature of the pipe.

If the time delay is considered due to the time it takes for air to go through the pipe, (4.37) becomes

$$T(s) = [T_a e^{-L/C} + (1 - e^{-L/C})T_2]e^{-(L/\upsilon_a)s} \ . \tag{4.38}$$

The pipe's output and input temperature relationship is shown in Figure 4.7.

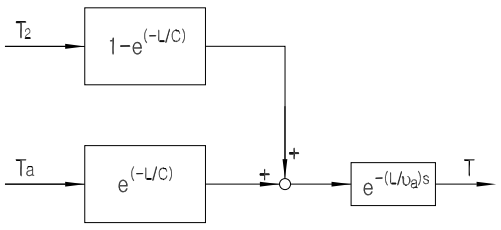

Figure 4.7: Block diagram of the heat transfer in the pipe

In order to decide d_2, the thickness of the insulation can be selected such that T_2 (the temperature of the external surface of the insulation) equals a given tem-

perature while the hot air in the pipe attains the maximum temperature permitted.

It is known that heat is transferred from the insulation surface to the surrounding air mostly by convection and radiation. According to the Stefan-Boltzman law (Malloy, 1969), heat transfer by radiation is given by

$$Q_r = 0.548\varepsilon[(\frac{T_2 + 273.16}{55.55})^4 - (\frac{T_0 + 273.16}{55.55})^4] \tag{4.39}$$

where Q_r = heat transfer by radiation (W/m^2),

ε = surface emittance,

T_2 = temperature of insulation's outer surface (^oC),

T_0 = temperature of ambient air (^oC).

In the case of convection taking place at the surface of the insulation, the heat transfer via natural convection as given by Langmuir (Malloy, 1969) is

$$Q_c = 1.957(T_2 - T_0)^{5/4} \tag{4.40}$$

where Q_c = heat transfer by convection (W/m^2).

Therefore, the total heat transferred from the surface of the insulation to the ambient air is

$$Q = 0.548\varepsilon[(\frac{T_2 + 273.16}{55.55})^4 - (\frac{T_0 + 273.16}{55.55})^4] + 1.957(T_2 - T_0)^{5/4} \ . \tag{4.41}$$

In practice, (4.32) is not used to calculate the thickness of the insulation because it does not lead to easy reference (Malloy, 1969). A more common method of calculating heat transfer is to base all heat transfer on the outer surface of insulation and to use thermal conductance, f_m, in the heat transfer formulae to arrive at

resistances, which is listed in (4.42):

$$Q = \frac{T_b - T_2}{\frac{d_2 ln\frac{d_2}{d_1}}{2k_m} + \frac{1}{f_m}} \tag{4.42}$$

where $f_m = 2k/(d_1 - d)$ $(W/m^2 \cdot^o C)$ is the thermal conductance of the pipe wall.

It is clear that at steady state, the heat transferred from the hot air in the pipe to the inner surface of the insulation is equal to the heat transfer from the surface of the insulation to the surrounding air. So we can get the thickness of insulation by combining (4.41) and (4.42).

For example, we may set the maximum T_b as 200^oC, the surface temperature of the insulation $T_2 \leq 50^oC$ and select one type of insulation with thermal conductivity $k_m = 0.07211\, W/m \cdot^o C$. The rest of the variables are set as

ambient temperature, $T_0 = 24\,^oC$,

emittance, ε= 0.85 (Malloy, 1969),

f_m= $12.489026\, W/m^2 \cdot^o C$ where $k = 0.0125\, W/m \cdot^o C$,

d_1= 102 mm.

From (4.41), Q is calculated as

Q=266.9571 (W/m^2)

Substituting this Q into (4.42), we obtain $d_2 = 159(mm)$ which means that the insulation having a thickness bigger than $28.5mm$ can meet the requirement. By using (4.32), we get

$$Q = \frac{T_b - T_2}{\frac{d_2 ln\frac{d_2}{d_1}}{2k_m} + \frac{d_2 ln\frac{d_1}{d}}{2k}} \tag{4.43}$$

which gives the same d_2.

We can also select other types of the insulation materials which have smaller thermal conductivities in order to minimize the outer surface temperature of the

insulation. In this way, the difference in temperature between the insulation's outer surface and the ambient can be ignored.

Suppose the parameters of the insulation material and the pipe material are selected as in Table 4.3. Setting the temperature of air in the pipe to be 200^oC,

	material	conductivity in $(W/m \cdot^o C)$	normal emittance ε
insulation	Shavings-Planner Red Wood Bark	0.0375	0.83-0.92
pipe	steel with less 0.6% carbon	41.82	

Table 4.3: Parameters of the insulation and the pipe

with the maximum surface temperature of the insulation being no more than 30^oC, the thickness of the insulation is computed to be at least $82mm$.

Finally, with $d_2 = 266\,mm$, $d_1 = 102\,mm$, $d = 100\,mm$, $L = 220\,mm$, $\varepsilon = 0.85$, $\rho_a = 1.1774\,kg/m^3$, $c_{pa} = 1006\,J/kg \cdot^o C$ and $C = 37.8453 v_a$, (4.38) becomes

$$T = [e^{-0.00581/v_a} T_a + (1 - e^{-0.00581/v_a}) \cdot T_2] e^{-(0.22/v_a)s} \,. \tag{4.44}$$

If v_a approaches zero, T approaches T_2 which is the surface temperature of the insulation. In that case, T_2 will be equal to the ambient temperature, T_0.

The block diagram of the models of the DC motor, the heating coils, the pipe and its insulation is shown in Figure 4.8. It can be seen that the air velocity is closely coupled to the output air temperature. The effects will be shown in simulations in Chapter 5.

4.5 Modeling of the Additional Coil

The role of the additional coil near the exit of the pipe was explained in Chapter 3. For the purpose of control of this additional coil, the model of the additional coil is now derived. Its schematic diagram is shown in Figure 4.9.

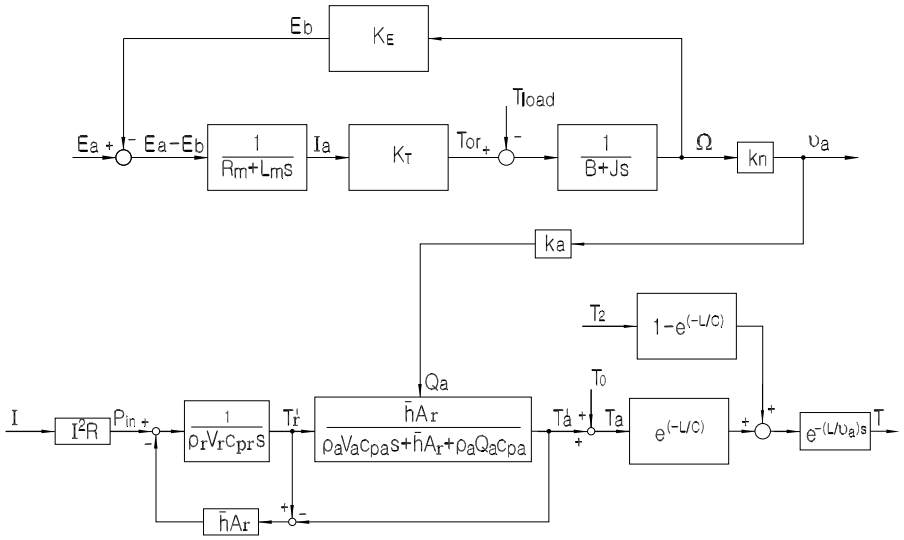

Figure 4.8: Block diagram of the main parts of the heat gun

Like the model of the main resistive coils proposed in Section 4.3, the model of the additional coil can be similarly analyzed. The control volume controlled by the additional coil is shown in Figure 4.9, where area 1 is assumed to be the space where the air temperature is raised by the additional coil.

Using the energy conservation law, (4.18), in the control volume of the additional coil, then the differential equation for this control volume can be written as in (4.45) and (4.48) where T_{add0} (^oC), the initial temperatures of air and the coil in the control volume of the additional coil are assumed to be equal to T_{inadd} (^oC), the air temperature at the inlet of area 1.

$$\rho_a V_{add} c_{pa} \frac{dT'_{add}}{dt} + \rho_r V_{radd} c_{pr} \frac{dT'_{radd}}{dt} = P_{inadd} - \rho_a c_{pa} Q_{add} T'_{add} \tag{4.45}$$

where c_{pa} = specific heat of air ($J/kg.^oC$),

c_{pr} = specific heat of the additional coil ($J/kg.^oC$),

V_{add} = volume of area 1 (m^3),

V_{radd} = volume of the additional coil, (m^3)

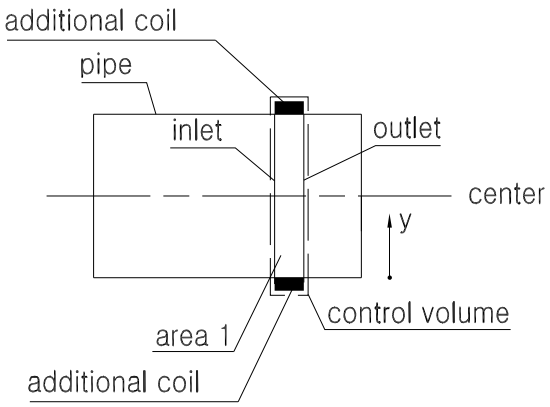

Figure 4.9: Control volume of the additional coil

ρ_a = density of air (kg/m^3),

ρ_r = density of the additional coil (kg/m^3),

T_{add} = average air temperature at the outlet of area 1 (^oC),

T_{radd} = temperature of the additional coil (^oC),

$T'_{add} = T_{add} - T_{inadd}$ (^oC),

$T'_{radd} = T_{radd} - T_{inadd}$ (^oC),

P_{inadd} = power input to the additional coil (W),

Q_{add} = air flow rate of area 1 (m^3/s), which is determined by v_{add} (m/s), the velocity of air in area 1, and k_{add} (m^2), the cross sectional area of area 1.

$$Q_{add} = k_{add} v_{add} \tag{4.46}$$

Applying conservation of energy to the additional coil (Kreith and Bohn, 1986), we have

$$P_{inadd} - \bar{h}_r A_{radd}(T_{radd} - T_{add}) = V_{radd} c_{pr} \rho_r \frac{dT_{radd}}{dt} \tag{4.47}$$

where $\bar{h}_r A_r(T_{radd} - T_{add})$ = the heat transferred from the additional coil to the air in area 1 by convection (W),

$\bar{h}_r$ = mean convective heat transfer coefficient $(W/m^2.^oC)$,

A_{radd} = surface area of the additional resistive coil (m^2).

(4.47) is then written as

$$P_{inadd} - \bar{h}_r A_{radd}(T'_{radd} - T'_{add}) = V_{radd} c_{pr} \rho_r \frac{dT'_{radd}}{dt} \ . \tag{4.48}$$

Taking Laplace transform of (4.45) and (4.48) and rearranging them, we get

$$\frac{T'_{add}(s)}{P_{inadd}(s)} = \frac{\bar{h}_r A_{radd}}{(\rho_a V_{add} c_{pa} \rho_r V_{radd} c_{pr}) s^2 + (\rho_a V_{add} c_{pa} \bar{h}_r A_{radd} + \rho_r V_{radd} c_{pr} \bar{h}_r A_{radd} + \\ + \rho_a Q_{add} c_{pa} \rho_r V_{radd} c_{pr}) s + \rho_a Q_{add} c_{pa} \bar{h}_r A_{radd}} \ . \tag{4.49}$$

The block diagram from P_{inadd} to T_{add} is shown in Figure 4.10.

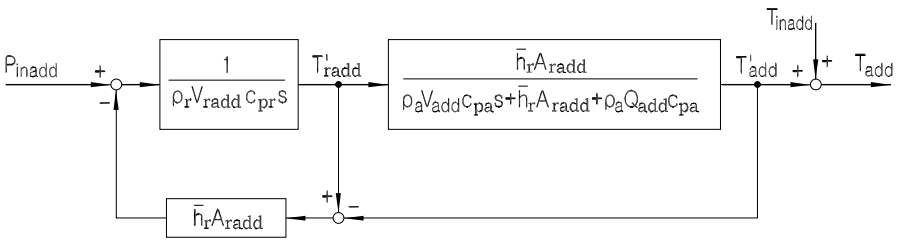

Figure 4.10: Block diagram of the additional coil

Setting the cross-section of the additional coil wire as a $6mm \times 1mm$ rectangle where $6mm$ is along the pipe's length, we obtain

$$V_{add} = 4.71 \times 10^{-5} \ m^3 \text{ and } k_{add} = 7.85 \times 10^{-3} \ m^2.$$

The temperature of the air at the output of the heat gun were investigated in Chapter 3. When the hot air moves through the pipe, a great amount of heat is lost to the pipe wall by the air near the pipe wall. Hence, the air temperature

across the cross-section of the outlet will be non-uniform and the air temperature at the center of the outlet is higher than the air temperature on other places across the outlet section. With the additional coil, the air with the average temperature, T_{inadd}, at the inlet of area 1, will heat up to approach the temperature, T_{cen}, at the center of the inlet of area 1. This will help to improve the temperature uniformity.

For the application of the additional coil whose transfer function is shown in (4.49), T_{cen} needs to be identified. T_{cen} changes with T. Suppose the additional coil is used after T becomes stable, T can be seen as a constant in this process. Then T_{cen} can be seen as a constant too under this condition. Under these conditions, the power requirement, P_{inadd}, can also be determined.

4.5.1 T_{cen} for the Additional Coil

From the previous analysis in Chapter 3, it is observed that the air temperature at the center of the outlet is higher than the air temperature at other points across the outlet section. Thus, the average air temperature is lower than the air temperature at the center, it shows that T_{inadd} is less than T_{cen}. To improve the temperature uniformity, it is required to reduce the difference between T_{inadd} and T_{cen}. Because T_{cen} cannot be decreased if the air velocity is constant, the improvement of the air temperature uniformity is then realized by increasing T_{inadd} to approach T_{cen}.

The transfer function of the additional coil is proposed in (4.49). The values of T_{cen}, which will decide the set point of T_{add}, has to be identified for this transfer function.

Suppose the input air temperature and velocity in the pipe are $140\,^oC$ and $5\,m/s$ respectively. Around $140\,^oC$, some properties of air are listed as follows (Holman, 1997):

Density $\rho_a = 0.8826\ kg/m^3$,

Specific heat $c_{pa} = 1014\ J/kg\cdot^o C$,

Kinematic viscosity $\nu_a = 25.9 \times 10^{-6}\ m^2/s$,

Prandtl number $Pr = 0.689$.

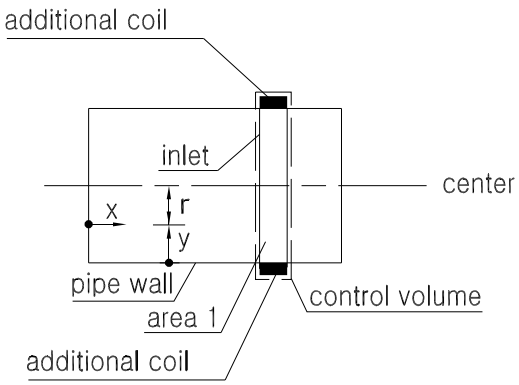

Figure 4.11: Schematic diagram of y and x for (4.50) and (4.52) respectively

For turbulent flow in a tube with $Pr \approx 1$, the temperature distribution (Burmeister, 1993) along the radial distance of the inlet of area 1 can be written as

$$\frac{T_y - T_w}{T_{cen} - T_w} = (\frac{y}{r_0})^{1/7} \tag{4.50}$$

where y = radial distance (m) from the pipe wall as shown in Figure 4.11,

T_y = air temperature in the radial location of y, located on the inlet section of area 1, (^oC),

T_{cen} = air temperature in the center of the inlet of area 1 (^oC),

T_w = temperature of the pipe wall (^oC),

r_0 = radius of the pipe (m).

According to (4.50), when T_{cen} approaches a certain temperature, T_y at other radial distances are less than T_{cen}. T_{inadd} is supposed to be the average temperature of T_y along the radial distance of the inlet section. From (4.50), the average

temperature from the pipe wall to y with respect to radial distance is given by

$$\bar{T_y} = \frac{1}{r_0 - r}\int_0^{r_0 - r} T_y dr = \frac{7}{8}(\frac{r_0 - r}{r_0})^{\frac{1}{7}}(T_{cen} - T_w) + T_w \tag{4.51}$$

where r (m) is the radius corresponding to the location of y and r_0 (m) is the radius of the pipe. When $r = 0$, $\bar{T_y} = T_{inadd}$.

To obtain T_w for (4.51), consider (4.52) (Bejan, 1995) which is suitable for the turbulent duct flow,

$$\frac{q''}{\rho_a c_{pa} \upsilon_a (T_w - T_{cen})} = 0.0296(\frac{\upsilon_a x}{\nu_a})^{-1/5} \tag{4.52}$$

where ν_a = kinematic viscosity of air (m^2/s)=25.9×10^{-6} m^2/s,

q''= heat flux (W/m^2),

x= axial distance from the inlet of the pipe (m), which is $0.1\,m$ for the inlet of area 1 (shown in Figure 4.11).

q'' can be obtained from (4.41). Setting $T_2 = 30\,^oC$, $T_0 = 24\,^oC$ and $\varepsilon = 0.85$, we get

$$q'' = -50.13\ W/m^2.$$

Substituting this $q'' = -50.13\ W/m^2$, c_{pa} and ν_a back into (4.52), we obtain

$$T_{cen} = T_w + 9.8706/(\upsilon_a)^{0.8}\ . \tag{4.53}$$

It is seen that T_{cen} approaches the temperature of the pipe wall, T_w when υ_a goes to infinity.

Substituting (4.53) into (4.51) and setting r_0=0.05 m and $r = 0$ m where $y = 0.05\ m = 5\,cm$, we get

$$T_{cen} = \bar{T_y}|_{y=0.05} + 1.234/(\upsilon_a)^{0.8}\ , \tag{4.54}$$

where $\bar{T}_y|_{y=0.05\,m}$ is the average air temperature from $r = 0$ to $r = 0.05\,m$ (see (4.51)),

or

$$T_{cen} = T_{inadd} + 1.234/(\upsilon_a)^{0.8} \tag{4.55}$$

We can assume that

$$T_{inadd} = T \quad \text{and} \quad \upsilon_{add} = \upsilon_a.$$

where T and υ_a are the average temperature and average velocity of the output air respectively. Therefore,

$$T_{cen} = T + 1.234/(\upsilon_a)^{0.8}\ . \tag{4.56}$$

From (4.56), it is seen that T_{cen} approaches T when υ_a goes to infinity. Equation (4.56) shows that for a given set point temperature, T, and air velocity, υ_a, the center temperature, T_{cen}, will always be higher according to this equation.

If the output air temperature and velocity of the pipe are 140 ^oC and 5 m/s respectively, from (4.56), we get

$$T_{cen} = 140.3405\ ^oC \tag{4.57}$$

As discussed before, T_{add} is proposed to be improved to approach T_{cen} by the additional coil. However, when the average temperature at the outlet of area 1, T_{add} is increased by the additional coil, the air temperature at the center of the outlet of area 1 will also be slightly increased by the additional coil. It will reduce the effectiveness of the additional coil on the air temperature uniformity. Therefore, T_{add} is not required to improve to the exact magnitude of T_{cen}. Thus suppose the temperature difference between T_{inadd} and T_{cen} is required to reduce by half times for this heat gun, the steady power input, derived from (4.45) and (4.46), for the

additional coil to the air in area 1 is

$$P_{inadd} = \rho_a k_{add} \upsilon_{add} c_{pa} \frac{T_{cen} - T_{inadd}}{2} \ . \tag{4.58}$$

Substituting (4.57) into (4.58), we obtain

$$P_{inadd} = 0.8826 \cdot 7.85 \times 10^{-3} \cdot 5 \cdot 1014 \cdot \frac{140.3405 - 140}{2} = 6 \ \ (W) \ . \tag{4.59}$$

The result was used in the FLUENT simulations in Chapter 3.

Using FLUENT to check (4.51), (4.53) and (4.56), the results are shown in Figure 4.12. $\bar{T}_y$ at different y is shown in Figure 4.12(a) where υ_a and T_{cen} are kept at $5\,m/s$ and $140\,^oC$ respectively. Figure 4.12(b) shows $\bar{T}$ under the conditions that T_{cen} is kept at $140\,^oC$ and υ_a is changed. In Figure 4.12(c), $\bar{T}$ is obtained under the conditions that υ_a is kept at $5\,m/s$ while T_{cen} is changed. It is seen that

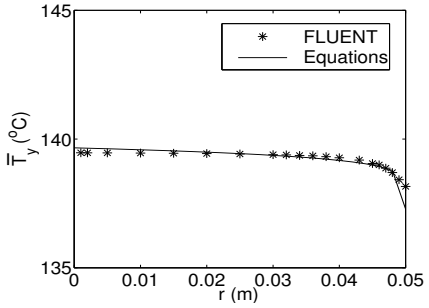

(a) $\bar{T}_y$ for different r ($r = r_0 - y$)

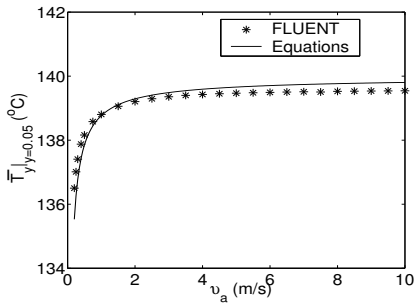

(b) $\bar{T}_y|_{y=0.05}$ for different υ_a

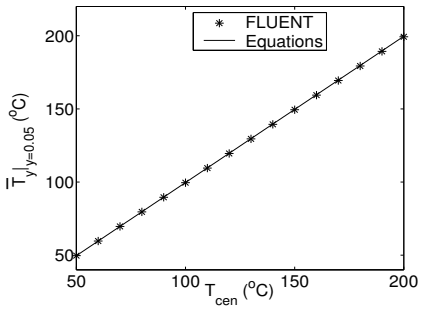

(c) $\bar{T}_y|_{y=0.05}$ for different T_{cen}

Figure 4.12: $\bar{T}$ from FLUENT and from (4.51) and (4.53)

$\bar{T}_y$ obtained from (4.51), (4.53) and (4.56) is relative close to those obtained from FLUENT, indicating that the analysis is quite accurate.

4.6 Modeling of the Heat Recycle

The heat recycle is shown in Figure 4.13, where t_a is the delay time caused by the hot air going through the recycle pipe, $1-\mu$ is the percentage of the fall in the air temperature at the beginning and end of the heat recycle, and P_c denotes the power of the air at the end of the heat recycle. From Figure 3.14 and 4.13, it

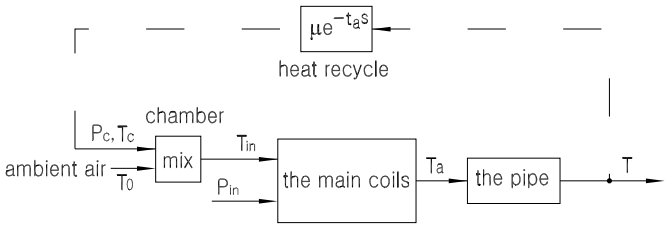

Figure 4.13: Process diagram for heating air by using the heat recycle

is clear that the input air temperature to the main resistive coils, T_{in}, is changed when the heat recycle is used. When the model of the resistive coils is proposed in Section 4.3, T_{in} is set as the ambient temperature, T_0. If the heat recycle is used and the air in the chamber is mixed well, the change in T_{in} can be expressed in (4.60) by using the energy conservation law:

$$\rho_a Q_{ac} c_{pa} T_c = \rho_a V_c c_{pa} \frac{dT_{in}}{dt} + \rho_a Q_a c_{pa} T_{in} - \rho_a Q_{a0} c_{pa} T_0 \tag{4.60}$$

where ρ_a = density of air (kg/m^3),

c_{pa} = specific heat of air $(J/kg.^oC)$,

Q_{ac} = air flow rate on the outlet of the heat recycle pipe (m^3/s),

Q_{a0} = air flow rate on the inlet of the heat gun (m^3/s),

Q_a = air flow rate on the input of the coil net (m^3/s),

T_c = air temperature on the outlet of the heat recycle pipe (^oC),

T_{in} = air temperature on the input to the coil net (^oC),

T_0 = ambient temperature (^oC),

V_c = volume of the chamber (m^3).

When air passes through the heat recycling pipe, the air flow rate and the air temperature will drop. The loss in the air flow rate is small if the heat recycle is well sealed. This loss is assumed to be zero. Together with the assumption that air is incompressible, we have

$$Q_{ac} + Q_{a0} = Q_a = total\ air\ flow\ rate. \tag{4.61}$$

Due to the heat loss during the heat recycle pipe, T_c may be expressed as

$$T_c(t) = \mu T(t - t_a) \tag{4.62}$$

where $1 - \mu$ = percentage of the fall in the air temperature,

t_a = transport lag (s) due to air flow from the output of the heat gun to the output of the heat recycle pipe.

μ is considered as the efficiency coefficient of the heat recycle, and t_a may be expressed as

$$t_a = l_a/\upsilon_a \tag{4.63}$$

where l_a = length of the heat recycle pipe (m),

υ_a = air velocity (m/s).

Then (4.60) becomes

$$\mu\rho_a Q_{ac} c_{pa} T(t - l_a/\upsilon_a) = \rho_a V_c c_{pa} \frac{dT_{in}(t)}{dt} + \rho_a Q_a c_{pa} T_{in}(t) - \rho_a (Q_a - Q_{ac}) c_{pa} T_0 \ . \tag{4.64}$$

Thus, (4.64) represents a model for the heat recycle unit. Taking Laplace transform of (4.64) and setting the initial conditions for T_{in} as ambient temperature, T_0, and combining (4.61), we have

$$T_{in}(s) = \frac{\mu}{\frac{V_c}{Q_a}s + 1} T(s) e^{-l_a/\upsilon_a} + T_0 \ . \tag{4.65}$$

The block transfer diagram of the heat recycle is shown in Figure 4.14.

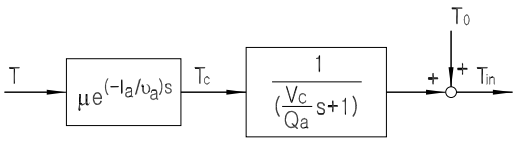

Figure 4.14: Block transfer diagram of the heat recycle

The overall system including heat recycle is shown in Figure 4.15. This figure shows the effect of the air flow rate, Q_a (υ_a), affecting the exit air temperature, T. At the same time, ambient temperature, T_o, and the external temperature of the insulation act as disturbances to the system. The simulations for this system will be shown in Chapter 5.

4.7 Conclusion

In this chapter, models of each part of the heat gun are proposed, including the DC motor, main resistive coils, the pipe with insulation, the additional coil and

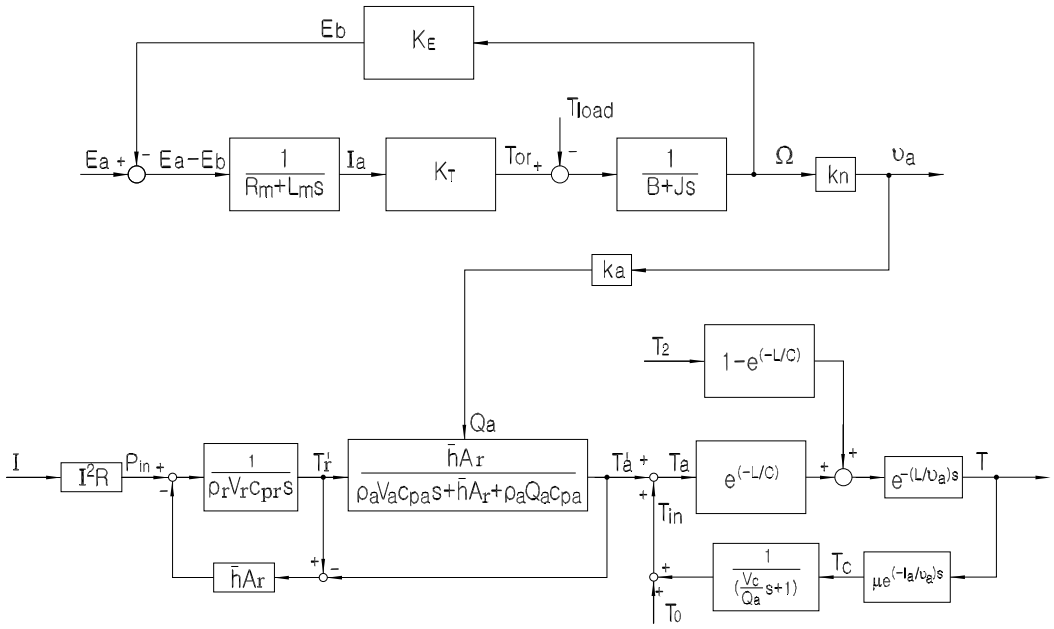

Figure 4.15: Block transfer diagram of the main parts of the heat gun

the heat recycle. These models will be used in the following chapters to determine the dynamic characteristics of the heat gun and to design the controllers.

Chapter 5

System Simulation

5.1 Introduction

The models obtained from Chapter 4 are used to simulate the system characteristics. The DC motor, the main resistive coils, the pipe and the additional coil are first considered independently. In Sections 5.6 and 5.7, the complete system without and with heat recycle is respectively simulated. MATLAB is used to carry out the simulations presented in this chapter.

5.2 Simulation of the DC Motor

The model obtained in Section 4.2 is used to simulate the DC motor.

The input armature voltage, e_a, is changed to different constants whose magnitudes are noted in Figure 5.1 where T_{load} is zero. As expected, the steady state speed of the motor changes for different e_a. While e_a is kept at $31\,V$, load disturbance, $T_{load} = 1\,N \cdot m$ is applied as shown in Figure 5.2(a). The response to this load disturbance is shown in Figure 5.2(b).

From Figure 5.1, it is clear that the output speed increases when the input e_a increases. From Figure 5.2, with $e_a = 50\,V$, it is found that the load disturbance

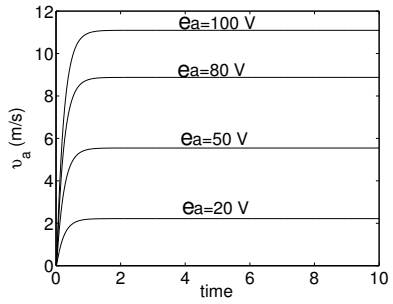

Figure 5.1: Responses with different inputs to DC motor

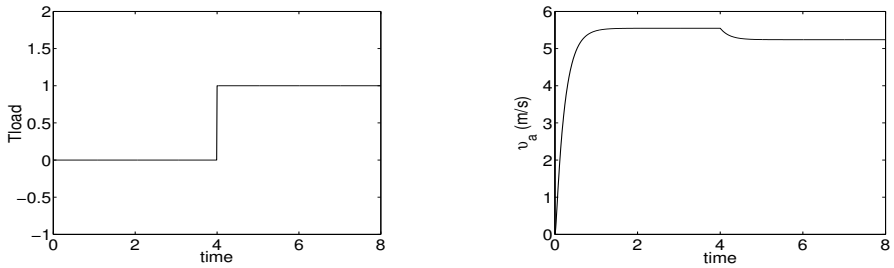

(a) T_{load} (b) v_a

Figure 5.2: Response of the DC motor to T_{load}

caused a drop in the output speed of the motor. This result is consistent with the open loop operation of the DC motor.

5.3 Simulation of the Main Resistive Coils

The model obtained in Section 4.3 is now used to simulate the process of air passing through the main resistive coils. We know that this partial system can be represented by (4.24) and (4.26).

When the velocity of the air is set as in Figure 5.3(a) and P_{in} is 5000 W, the temperature of the air after the main resistive coils is shown in Figure 5.3(b) and 5.3(c) which is the partial amplification of Figure 5.3(b). From 5.3(c), it is found that after the resistive coils are heated up, the response of the coils to a change in the air velocity is relatively fast compared to the initial response when the coils are at ambient temperature. As expected, when the air flow over the coils drops,

the air temperature increases, as the air takes a relatively longer time to flow over the coils and hence is heated up to a higher temperature.

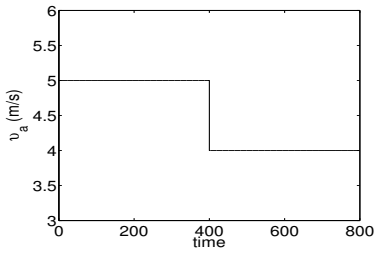

(a) Air velocity

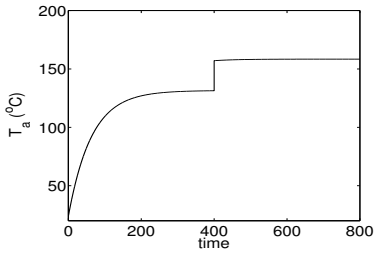

(b) Air temperature out of the heater coils

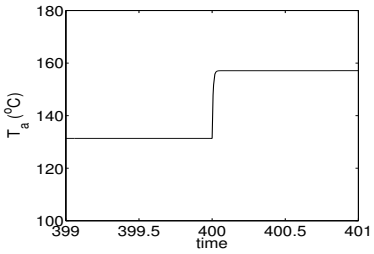

(c) Air temperature out of the heater coils

Figure 5.3: Response of the main resistive coils to the air velocity change

Keeping the same input power, $P_{in} = 5000\,W$, and changing the input air velocity, the output air temperature of the main resistive coils is shown in Figure 5.4. From Figure 5.4, it is found that when the air velocity increases, the steady state

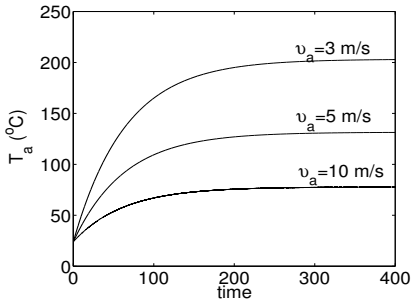

Figure 5.4: Air temperature out of the heater coils with different input air velocities

air temperature decreases. The influence of the air velocity on the air temperature is significant.

5.4 Simulation of the Heat Transfer in the Pipe

In Section 4.4, the heat transfer in the pipe is analyzed. The model in (4.44) is now simulated under the condition that the temperature of the air at the input of the pipe is at $T_a = 140\ ^oC$.

Setting $T_0 = 24\ ^oC$, $\upsilon_a = 5\ m/s$, the pipe length, $L = 220\ mm$, the response of the air temperature at the exit of the pipe is shown in Figure 5.5.

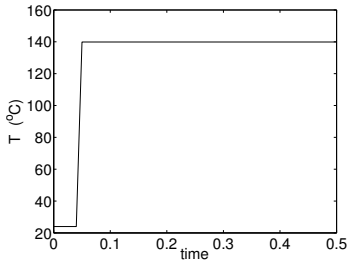

Figure 5.5: Response of the pipe

Keeping the length of the pipe at 220 mm and changing the air velocity, υ_a from 0.001 m/s to 10 m/s, the output air temperature, T, is shown in Figure 5.6. Similar to the analysis in Section 4.4, T approaches the the insulation surface's temperature, T_2, when υ_a is close to zero. From Figure 5.6, it can be seen that when the air velocity increases, the output air temperature increases because the heat loss from hot air inside the pipe to the pipe wall decreases when the air velocity increases. When air velocity is above 1 m/s shown in Figure 5.6, the output air temperature is almost invariable.

5.5 Simulation of the Additional Coil

In Section 4.5, the parameters of the additional coil are obtained as

$$V_{add} = 4.71 \times 10^{-5}\ m^3,$$

$$T_{cen} = T + 1.234/(\upsilon_a)^{0.8},$$

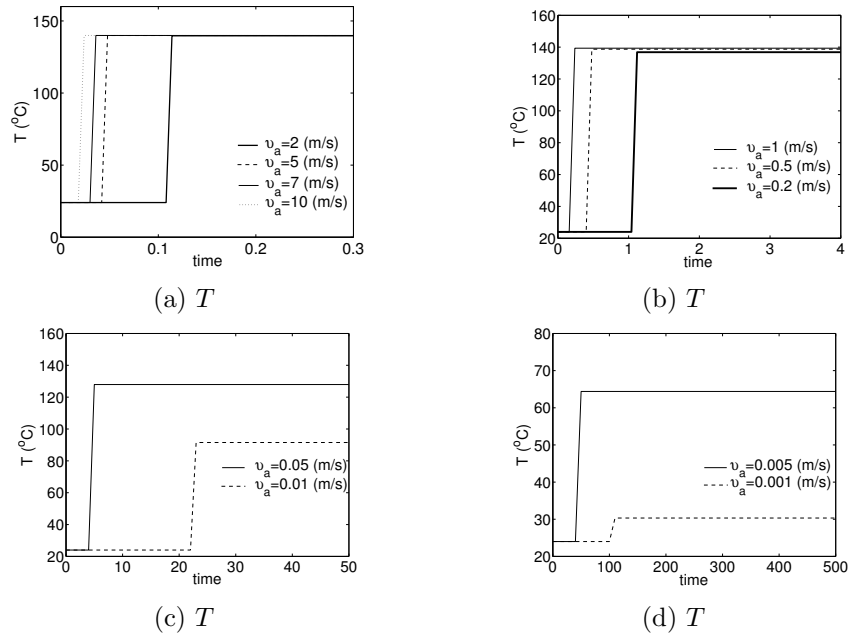

(a) T (b) T

(c) T (d) T

Figure 5.6: Air temperature from the heater pipe

$Q_{add} = k_{add}\upsilon_{add} = 7.85 \times 10^{-3}\upsilon_a$,

$V_{radd} = 1.9038 \times 10^{-6}\ m^3$,

$A_{radd} = 4.44 \times 10^{-3}\ m^2$,

$\bar{h}_r = 25\ W/m^2.^oC$,

$\rho_a = 0.8826\ kg/m^3$,

$\rho_r = 7300\ kg/m^3$,

$c_{pa} = 1014\ J/kg.^oC$,

$c_{pr} = 490\ J/kg.^oC$,

with the assumption that $\upsilon_{add} = \upsilon_a$ and $T_{inadd} = T$.

Substituting these values into (4.49), we obtain

$$\frac{T'_{add}(s)}{P_{inadd}(s)} = \frac{0.111}{0.287s^2 + (0.761 + 47.842\upsilon_a)s + 0.780\upsilon_a}\ . \tag{5.1}$$

When $v_a = 5\ m/s$, the two poles of (5.1) are at $s_1 = -836.1196$ and $s_2 = -0.0163$. Due to the small magnitude of s_2, we can predict that the response of the additional coil is slow.

Using (4.45) and (4.48), Setting $v_a = 5\ m/s$, $P_{inadd} = 10\ W$ and $T = 140\ ^oC$ ($T_{inadd} = 140\ ^oC$), the response of the additional coil is shown in Figure 5.7. From

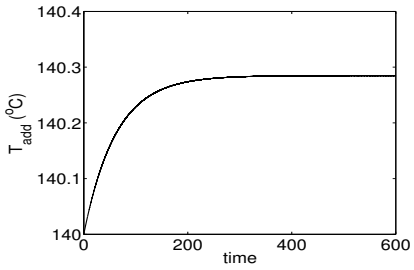

Figure 5.7: Response of the additional coil

Figure 5.7, it is found that the response of this part is slow because the internal energy change of the additional coil is considered.

5.6 Simulation of the Complete System without Heat Recycle and Additional Coil

This section shows the simulation of the whole heat gun without the heat recycle and the additional coil. The complete model (without the heat recycle and the additional coil) is divided into two parts as shown in Figure 5.8. The two parts are the motor and the heater and Figure 5.8 shows the interaction between them.

In the simulation, the input to the DC motor, e_a, is set as $50\,V$ and the input to the main resistive coils, P_{in}, is $5000\,W$. The response of the system is shown in Figure 5.9, where Figure 5.9(c) is the partial amplification of the initial response from Figure 5.9(b). In Figure 5.9(c), the small oscillation in the T is due to the starting of the DC motor and the time delay term, $e^{-(0.22/v_a)s}$, which is due to

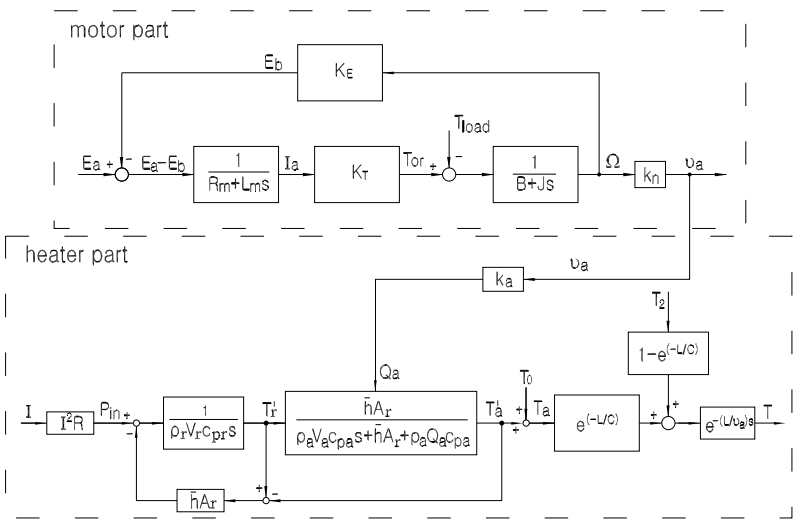

Figure 5.8: Division of the main heat gun system

the air movement in the pipe. It is seen that it is about 0.12 *sec* before the air temperature starts rising from the ambient temperature of 24 ^oC.

When the system reaches steady state at about 500 *sec*, a load disturbance, T_{load} shown in Figure 5.10(a), is added to the DC motor. The response of the system is shown in Figure 5.10(b) and Figure 5.10(c).

From Figure 5.10, it is found that T_{load} has a big effect on the speed of the DC motor and the output air temperature of the heater.

From Figure 4.8, it is clear that the air temperature is related to the motor speed. From Figure 5.4, it can be seen that T_a increases as the air velocity reduces. This same relationship is seen in Figures 5.10(a), 5.10(b) and 5.10(c).

5.7 Simulation with the Heat Recycle

From the simulation result in Section 5.6, it is found that an input power of 5000 W to the main resistive coils is required to produce hot air at a velocity of 5.5 m/s and temperature of 120 ^oC. This system is therefore very costly to operate continuously. Therefore, heat recycle is adopted to improve energy efficiency.

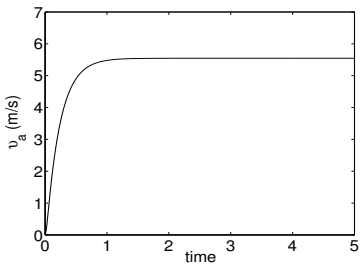

(a) Air velocity

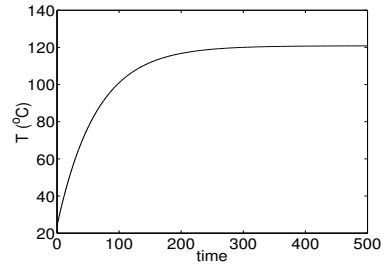

(b) Output air temperature

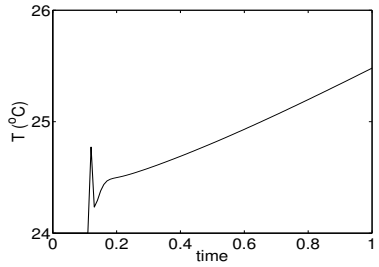

(c) Output air temperature

Figure 5.9: Response of the heat gun (without the heat recycle and additional coil)

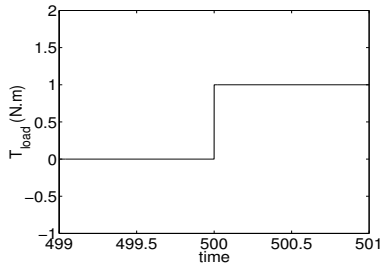

(a) T_{load}

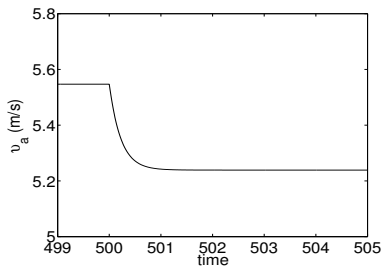

(b) υ_a

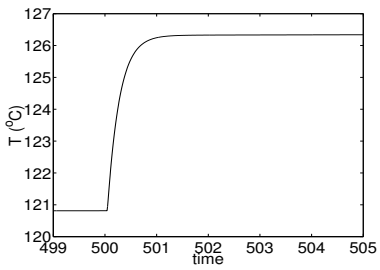

(c) T

Figure 5.10: Response of the main parts to T_{load}

For a spherical chamber of radius $100\,mm$, its volume is $V_c = 4.1867{\times}10^{-3}\ m^3$. In addition,

$c_{pa} = 1006\ J/kg.^oC$,

$\rho_a = 1.1774\ kg/m^3$,

$k_a = 7.85{\times}10^{-3}\ m^2$,

and we set the ambient temperature, T_0, as $24\,^oC$,

the length of the heat recycle pipe, l_a, as $2\,m$,

the efficiency coefficient of heat recycle , μ, as 0.7 (70%).

Substituting these values into (4.64) and simulating in MATLAB, we obtain the new response of the heating process shown in Figure 5.11(a), where $E_a = 50\,V$ and $P_{in} = 5000\,W$ which are the same as the setting in Section 5.6.

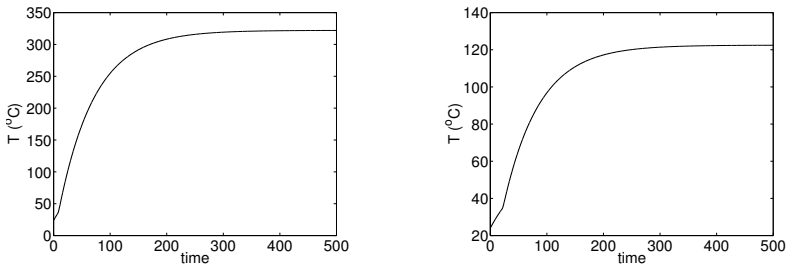

(a) T (b) T

Figure 5.11: Output air temperature with the heat recycle

Comparing with Figure 5.9(b), we see that the air temperature is much higher when the heat recycle is used with the power remaining the same. This result shows that if the air temperature is to be maintained at around the same value as that in Figure 5.9(b), P_{in} should be reduced to 1900 W whose result is shown in Figure 5.11(b).

5.8 Conclusion

In this chapter, each part of the heat gun has been simulated. From the simulations, we find that the load disturbance has an effect on the air velocity and temperature.

The response of the main resistive coils and the additional coil are not fast, and the power needed to raise the air temperature is high when there is no heat recycle. In later chapters, different controllers are designed for the heat gun using several strategies while heat recycle is used.

Chapter 6

Design of PID Controllers

6.1 Introduction

In Section 5.6, we divided the main system into two parts (see Figure 5.8), the motor and the heater part comprising the main electric resistive coils and the insulated pipe. In addition, the additional resistive coil is used to compensate for heat loss to the walls of the pipe. To control the heat gun, we control these three subsystems to achieve the desired air temperature and velocity profiles. The first is the motor for controlling the air velocity. The second is the heater for controlling the air temperature. The third is the additional coil for controlling the temperature of the air near the exit of the pipe so as to improve the temperature uniformity.

This heat gun is required to produce hot air with uniform temperature and velocity. Any oscillation of the output air temperature and velocity should be as small as possible at steady state. The temperature and velocity uniformities should be no more than $0.5\,^oC$ at $140\,^oC$ and $1\,m/s$ at $5\,m/s$ respectively. Thus, the steady state error of the air temperature and velocity outputs must be less than these uniformities.

To begin with, PID controllers are first designed to control the heat gun because PID controllers are widely used in the industry. In this chapter, the controllers for

every subsystem is designed independently.

6.2 Design of the PID Controllers

In theory, the PID controller is given by

$$G_{PID}(s) = K_p(1 + T_d s + \frac{1}{T_i s}) \quad . \tag{6.1}$$

For the motor, its transfer function can be written in the form of (6.2) (see (4.15)),

$$G_m(s) = \frac{C}{s^2 + As + B} \quad . \tag{6.2}$$

The closed-loop system is shown in Figure 6.1 where R_v is the set point for the air velocity.

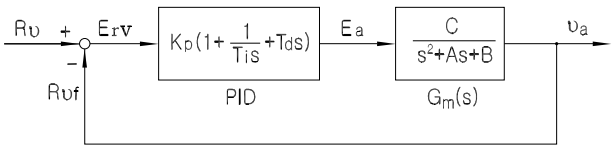

Figure 6.1: Block diagram of the motor with PID controller

With the PID controller in (6.1), the transfer function for the closed-loop system in Figure 6.1 is given by

$$G_{nm}(s) = \frac{CK_pT_iT_ds^2 + CK_pT_is + CK_p}{T_is^3 + (T_iA + CK_pT_iT_d)s^2 + (T_iB + CK_pT_i)s + CK_p} \quad . \tag{6.3}$$

The desired closed loop characteristic polynomial for the system in (6.3) can be determined by the choice of a good settling time and maximum overshoot. Since (6.3) is a second order system, one pole should be chosen far away from the imaginary axis so that it has little impact on the system response. Suppose that the settling time is chosen as 2 *sec* and the maximum overshoot is 5%, then the

desired dominant poles given by the solutions of $s^2 + 4s + 8 = 0$ will satisfy these specifications. The additional pole is chosen at -60. Then from pole placement calculations, $K_p = 0.9704$, $T_i = 0.0478$ and $T_d = 0.3993$. The simulation result of the closed-loop system is shown in Figure 6.2, where the air velocity set point is $5\,m/s$. A load torque of $1\,N \cdot m$ is added at time $8\,sec$. Comparing with the open

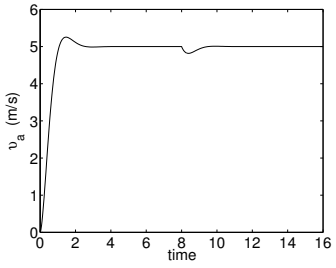

Figure 6.2: Response of the motor part with the PID controller

loop response in Figure 5.10(b), it is seen that the closed-loop system maintains zero steady state error after the disturbance, T_{load}, has been applied.

The analysis of the heating process is similar to that of the DC motor. The transfer function of the main resistive coils can be written in the form of (6.4) (see (4.27) and (4.29)).

$$G_{hr}(s) = \frac{C}{s^2 + As + B}\ , \tag{6.4}$$

and the transfer function of the insulated pipe can be written in the form of (6.5) (see (4.44)).

$$G_{hp}(s) = k_f e^{-as} \tag{6.5}$$

where $k_f \approx e^{-0.00581/\upsilon_a}$ is the gain caused by the heat loss across the pipe (see (4.44)), and the time delay, $a = 0.22/\upsilon_a$, is caused by the air movement through the pipe.

Thus the transfer function of the heating process can be written as

$$G_h(s) = G_{hr}(s)G_{hp}(s) = \frac{Ck_f e^{-as}}{s^2 + As + B}\ . \tag{6.6}$$

The closed-loop system of the heating process with a PID controller is shown in Figure 6.3 where T_0 is the ambient temperature and R_T is the set point for the air temperature.

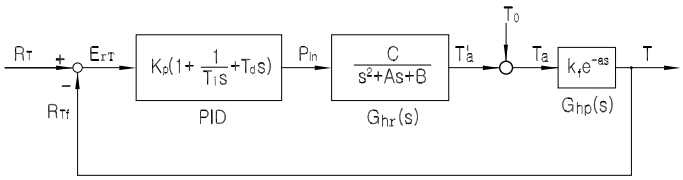

Figure 6.3: Block diagram of the heating process with the PID controller

Suppose $\upsilon_a = 5\,m/s$, the time delay, $0.22/\upsilon_a = 0.044\,sec$, is very small because of the short pipe and the high air velocity. To simplify, the time delay is not considered in designing the PID controller for the heating process. Then the simplified closed-loop transfer function can be written as in (6.7):

$$G_{nh}(s) = \frac{Ck_fK_pT_iT_ds^2 + Ck_fK_pT_is + Ck_fK_p}{T_is^3 + (T_iA + Ck_fK_pT_iT_d)s^2 + (T_iB + Ck_fK_pT_i)s + Ck_fK_p} \qquad (6.7)$$

Since (6.7) and (6.3) are similar, the choice of the PID parameters for the heating process is similar to that for the motor part. However, some properties of the heating process need to be considered. From Figure 5.4, it is observed that the response of the main resistive coils is very slow. Although fast response is needed, the expense of this requirement is a high input power to the main resistive coils. This will also cause a large overshoot which can only be reduced theoretically by applying a negative power to the heater coils which is equivalent to a cooling process. Since cooling is not allowed for in the design, the input power to the main resistive coils is then set to zero so as to reduce the overshoot. This power constraint has to be considered in the design of the PID controllers. The requirements of the closed-loop system are set as follows:

(a) The maximum overshoot should not exceed 2 ^oC when the desired output is 140 ^oC. Hence the maximum overshoot should be less than 1.4%.

(b) A fast response is required. From Figure 5.9(b), the open loop settling time is about 230 *sec*. Thus, the settling time is arbitrarily selected as 110 *sec*.

Like the motor part, in addition to two dominant poles, one more pole should be selected as the closed loop is a third order system. Since v_a is around $5\,m/s$ in this design, $k_f = e^{-0.00581/v_a} = 0.9988$. Selecting the third pole at -30, we obtain $K_p = 68.3143$, $T_i = 15.1626$, $T_d = 1.1005$, $\zeta = 0.8040$ and $\omega_n = 0.0995$. Using these parameters, the maximum overshoot exceeds the desired value. This is because of ζ. Reselecting $\zeta = 1.5$, we obtain $K_p = 68.2072$, $T_i = 52.6878$, $T_d = 1.1022$.

The closed loop response is shown in Figure 6.4 where the air velocity is set as $5\,m/s$. Input power to the main resistive coils is shown in Figure 6.4(b). From Figure 6.4(a), it is observed that the maximum overshoot, which is 0.786% ($141.1\,^oC$), meets the requirements, and the settling time, which is 115 *sec*, is 5 *sec* more than the requirements.

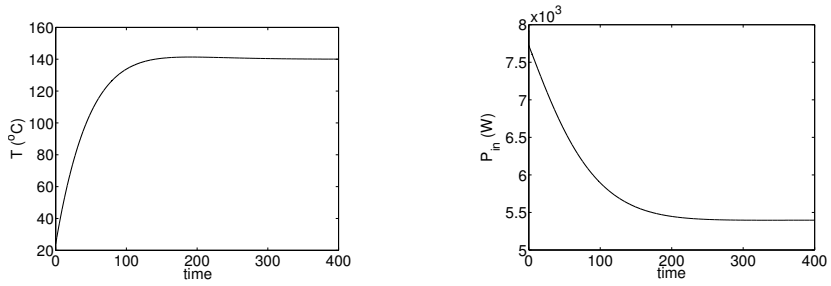

(a) T (b) P_{in}

Figure 6.4: Response of the heating process with the PID controller

Combining the DC motor and the heating process, the total response is shown in Figure 6.5.

From Figure 6.5(c), we find that the input power is too high and may be unrealizable for some period of time. Hence, the control system with the heat recycle is considered next.

The closed loop system with the heat recycle is shown in Figure 6.6. The maximum power input to the main resistive coils is set at $7000\,W$. With the same

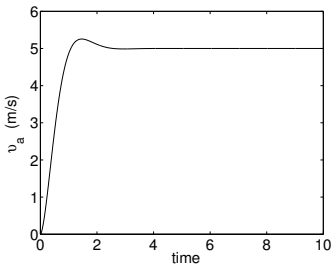

(a) Output air velocity

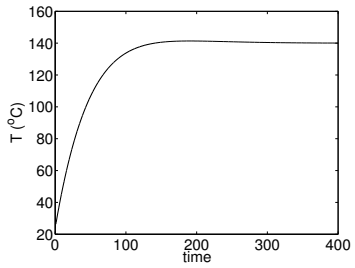

(b) Output air temperature

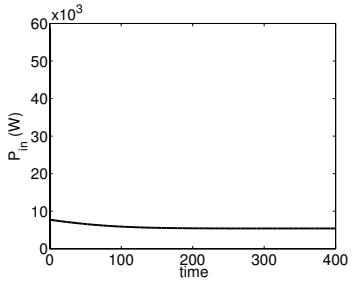

(c) Input power to the main resistive coils

Figure 6.5: Response of the overall process with the PID controllers

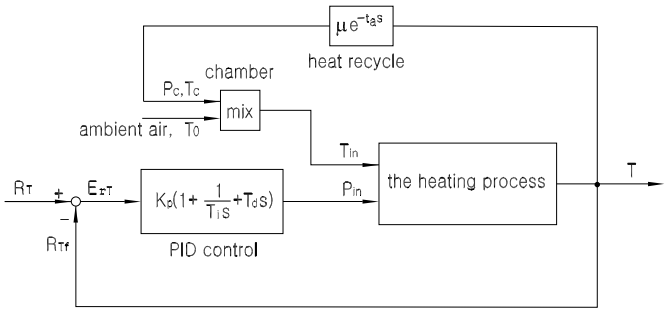

Figure 6.6: Heating process with heat recycle

PID parameters as those designed above, the response of the air temperature is shown in Figure 6.7 where the maximum overshoot is 2.5% ($143.5\,^oC$) and the settling time is $90\,sec$.

Comparing Figure 6.5(b) with Figure 6.7(a), it is found that the response of the heating process is faster and the overshoot is larger when heat recycle is used. From Figure 6.5(c) and Figure 6.7(b), it is clear that the power input has decreased greatly after heat recycle is used. However, the overshoot specification is not satisfied (see Figure 6.7(a)) and hence modifications of the PID controller is considered

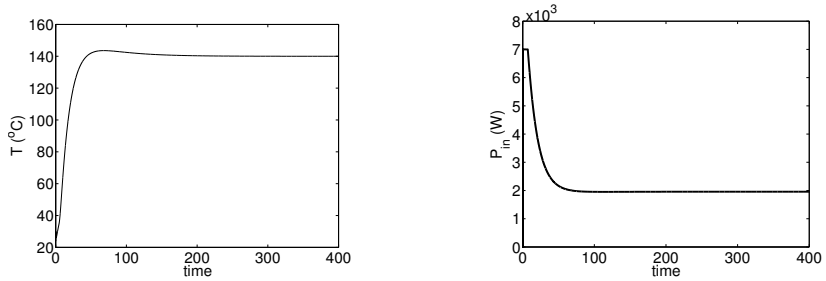

(a) Output air temperature (b) Input power to the resistive coils

Figure 6.7: Response of the heating process with heat recycle

next.

6.3 Modification of the PID Controller

In practice, to reduce the overshoot and the influence of the abrupt change in the set point, u_c, set point weighting (Åström and Hägglund, 1988) is used in the PID controller. The modified PID is shown in (6.8). This modified PID controller adds a zero at $-1/T_i b$ to the closed-loop system. b is selected so that this zero is 2 to 3 times larger than the dominant poles. In addition, the modified PID contains a filter which filters the measurement noise at the output $Y(s)$.

$$U(s) = K_p\{bU_c(s) - Y(s) + \frac{1}{T_i s}[U_c(s) - Y(s)] - \frac{T_d s}{1 + \frac{T_d s}{N}} Y(s)\} \tag{6.8}$$

By using this modified PID controller, the closed loop transfer function of the DC motor becomes

$$G_m(s) = \frac{K_p C[\frac{bT_i T_d}{N} s^2 + (T_i b + \frac{T_d}{N})s + 1]}{\frac{T_i T_d}{N} s^4 + (T_i + \frac{T_i T_d A}{N})s^3 + (T_i A + \frac{BT_i T_d}{N} + \frac{K_p C T_i T_d}{N} + K_p C T_i T_d)s^2 + (T_i B + K_p C T_i + \frac{K_p C T_d}{N})s + K_p C} . \tag{6.9}$$

When the original PID controller is replaced by this modified PID controller,

the closed loop transfer function of the heating process becomes

$$G_h(s) = \frac{K_p C k_f [\frac{bT_iT_d}{N}s^2 + (T_ib + \frac{T_d}{N})s + 1]}{\frac{T_iT_d}{N}s^4 + (T_i + \frac{T_iT_dA}{N})s^3 + (T_iA + \frac{BT_iT_d}{N} + \frac{K_pCk_fT_iT_d}{N} + K_pCk_fT_iT_d)s^2 + (T_iB + K_pCk_fT_i + \frac{K_pCk_fT_d}{N})s + K_pCk_f} \tag{6.10}$$

where the time delay is ignored.

According to the requirements of the maximum overshoot and settling time, K_p, T_i, T_d and b in (6.10) and (6.9) have to be reselected. $K_p = 2.2$, $T_i = 0.11$, $T_d = 0.3$ and $b = 2$ were obtained for the motor part while $K_p = 54.5$, $T_i = 35$, $T_d = 0.2$ and $b = 0.5$ were obtained for the heating process. In both controllers, select $N = 10$ (Åström and Hägglund, 1988). The closed loop responses are calculated using (6.9) and (6.10) and the results are shown in Figure 6.8, where T_{load}=1 $N.m$ is added at a time of 400 sec and heat recycle is used. The desired air temperature setting, R_T, is 140 ^oC and the desired air velocity setting, R_v, is 5 m/s.

Comparing Figures 6.8(a) and 6.8(c) with Figures 6.5(a) and 6.7(a) respectively, it is found that the overshoot has decreased from 5% to 4% (from 5.25 m/s to 5.2 m/s) in the air velocity and from 2.5% to 0.14% (from 143.5 ^oC to 140.2 ^oC) in the air temperature. Settling time has decreased from 1 sec to 0.93 sec and from 90 sec to 85 sec for the air velocity and temperature respectively.

If the set points of v_a and T are changed to 7 m/s at a time of 500 sec and to 150 ^oC at a time of 700 sec respectively, the responses are shown in Figure 6.9.

From Figures 6.8 and 6.9, it is observed that the modified PID controllers designed for the motor and heater parts have achieved their specifications.

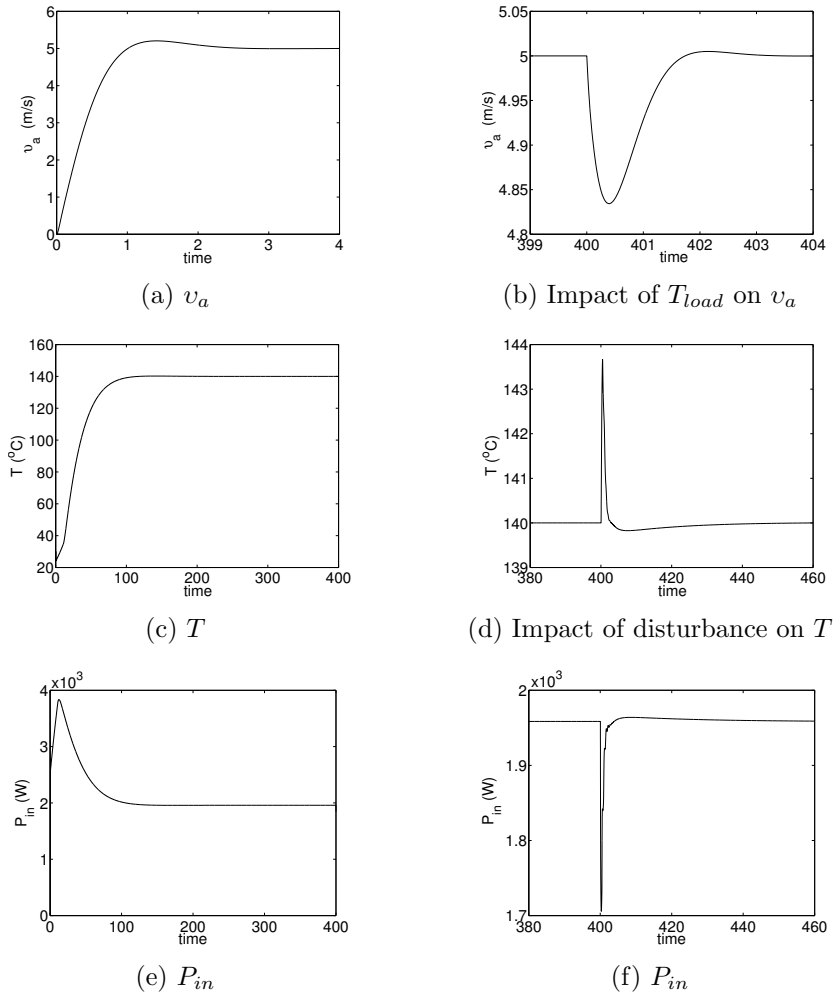

(a) υ_a (b) Impact of T_{load} on υ_a

(c) T (d) Impact of disturbance on T

(e) P_{in} (f) P_{in}

Figure 6.8: Responses of the two main parts with the modified PID controller

6.4 PID Control for the Additional Coil

The process of designing the PID controller for the additional coil is similar to that for the heating process shown in the earlier sections.

Substituting $\upsilon_a = 5\ m/s$ into (5.1), we get

$$\frac{T'_{add}(s)}{P_{inadd}(s)} = \frac{0.111}{0.287s^2 + 239.971s + 3.9}\ . \tag{6.11}$$

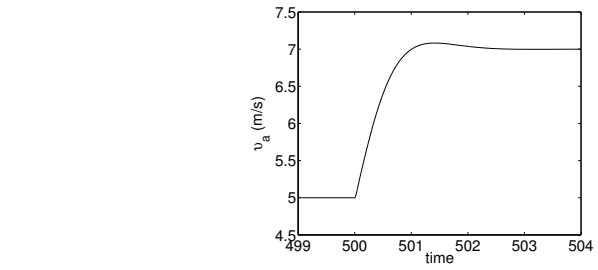

(a) υ_a

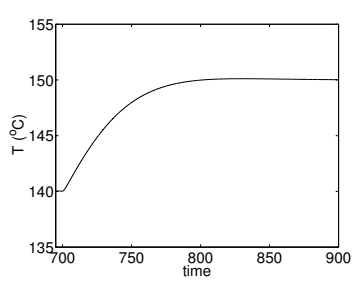

(b) T

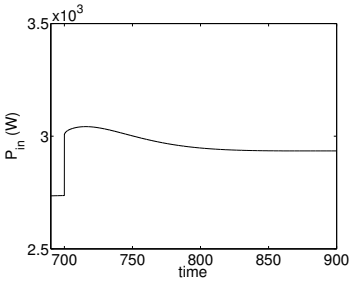

(c) P_{in}

Figure 6.9: Responses of the two main parts to the changes of set points

Partial factorizing (6.11), we obtain

$$\frac{T'_{add}(s)}{P_{inadd}(s)} = \frac{4.6257 \times 10^{-4}}{s + 0.0163} - \frac{4.6257 \times 10^{-4}}{s + 836.1196} \ , \tag{6.12}$$

which shows the poles at $s = -836.1196$ and $s = -0.0163$. Hence, the response of (6.12) will be dominated only by the first partial factor.

Then the transfer function of the additional coil can be approximately written as

$$G_{add}(s) = \frac{4.6257 \times 10^{-4}}{s + 0.0163} = \frac{B}{s + A} \ . \tag{6.13}$$

The additional coil is used after T and υ_a have reached steady state. The overshoot of its response is required to be minimal so as to meet the temperature uniformity. Thus, the modified PID controller is selected. By using the modified PID controller shown in (6.8), the closed-loop transfer function of the additional coil becomes

$$G_{add}(s) = \frac{K_pB[\frac{T_iT_db}{N}s^2 + (T_ib + \frac{T_d}{N})s + 1]}{\frac{T_iT_d}{N}s^3 + (T_i + \frac{T_iT_dA}{N} + \frac{T_dK_pBT_i}{N} + K_pBT_iT_d)s^2 + (T_iA + K_pBT_i + \frac{K_pBT_d}{N})s + K_pB}. \quad (6.14)$$

K_p, T_i and T_d can be calculated by comparing the denominator of (6.14) with the desired characteristic polynomial. If v_a =5 m/s, T = 140 ^oC and the maximum overshoot of this part is no more than 0.2 ^oC, then K_p=505.2208, T_i=51.9333, T_d=0.1, b=1 and N=10, where the desired characteristic polynomial is $(s{+}100)(s^2{+}0.25s + 0.0045)$.

As discussed in Section 4.5.1, we assume that the temperature difference between T_{inadd} and T_{cen} is required to reduce by half, where T_{inadd} is 140 ^oC and T_{cen} is 140.34 ^oC obtained from (4.56). Thus the setting of the output air temperature for this part is 140.17 ^oC. By using the modified PID controller with the above parameters, the response is shown in Figure 6.10, where the power input, P_{inadd}, to the additional coil is in the range of $0 \sim 200\,W$.

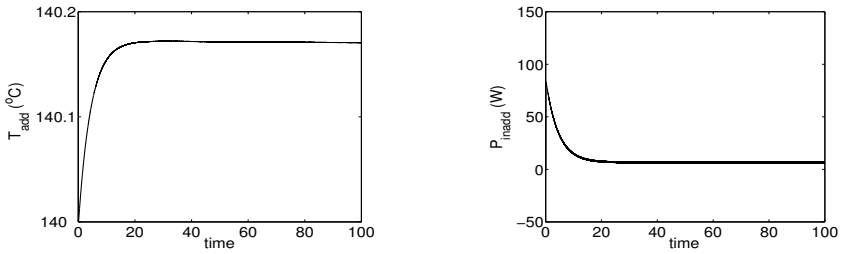

(a) T_{add} (b) P_{inadd}

Figure 6.10: Response of the additional coil with the modified PID controller

When the air velocity changes from 5 m/s to 7 m/s at a time of 200 sec, T_{cen} becomes 140.26 ^oC and thus the set point of T_{add} is 140.13 ^oC. The temperature response due to the additional coil is shown in Figure 6.11(a). When T changes from 140 ^oC to 150 ^oC at a time of 400 sec, T_{cen} becomes 150.26 ^oC and then the set point of T_{add} is 150.13 ^oC. The response of this part is shown in Figure 6.11(b). P_{inadd} for these two stages is shown in Figure 6.11(c) by using the same modified PID controller.

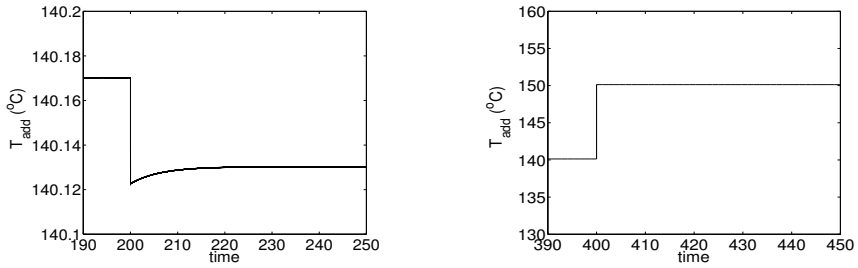

(a) T_{add}

(b) T_{add}

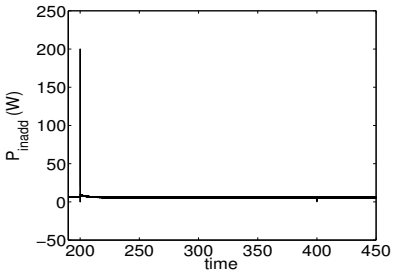

(c) P_{inadd}

Figure 6.11: Response of the additional coil to the changes of set points

6.5 Conclusion

In this chapter, two types of PID controllers are used to control the heat gun. When choosing PID parameters, fast response and zero steady errors are considered. For designing the PID controllers, the desired dominant characteristic polynomial is determined by the required response characteristics, such as the settling time and the maximum overshoot. Parameters of the PID controllers are obtained by using the pole placement method.

Chapter 7

State Feedback Control Methods

7.1 Introduction

In the previous chapter, the feedback signals were mainly outputs. In addition to the output variables, T and v_a, the system has other states which have not been used for control. In this chapter, the heat gun is controlled using state feedback methods such as the state feedback control by using the pole placement method, the Linear-Quadratic state-feedback Regulator (LQR) and Linear-Quadratic-Gaussian (LQG) control. Each subsystem of the heat gun is investigated separately. In order to obtain good uniformity in the air temperature and velocity, T and v_a, their steady state errors should be less than $\pm 0.5^oC$ and $\pm 1\, m/s$ respectively. At the same time, the maximum overshoots of the responses should be less than 1.4% and 5% for T and v_a respectively. The settling time of T and v_a are also respectively set as $110\, sec$ and $2\, sec$ as in the previous chapter. The settling time and maximum overshoot of the additional coil, T_{add}, should be less than $50\, sec$ and $0.2\, ^oC$ respectively. The steady state error of T_{add} should be less than $0.2\, ^oC$. The problem of actuator saturation is also considered in this chapter.

To apply the above control methods, state space representations of the heat gun are required.

7.2 State Space Representations of the Heat Gun

State space representations of the motor part are deduced from (4.1), (4.3), (4.6) (4.10) and (4.16), which are reproduced here for convenience.

$$\upsilon_a(t) = k_n\omega(t) = 0.02\omega(t) \tag{4.16}$$

$$e_b(t) = K_E\omega(t) \tag{4.1}$$

$$e_a(t) = L_m\frac{di_a(t)}{dt} + R_m i_a(t) + e_b(t) \tag{4.3}$$

$$T_{or}(t) = K_T i_a(t) = 0.18 i_a(t) \tag{4.6}$$

$$J\frac{d\omega(t)}{dt} = T_{or}(t) - T_{load}(t) - B\omega(t) \tag{4.10}$$

From (4.16), (4.1) and (4.3), we obtain

$$\begin{aligned}\frac{di_a(t)}{dt} &= -\frac{R_m}{L_m}i_a(t) - \frac{K_E}{k_n L_m}\upsilon_a(t) + \frac{1}{L_m}e_a(t)\\ &= -54.3478 i_a(t) - 978.2609\upsilon_a(t) + 108.6957 e_a(t)\ .\end{aligned} \tag{7.1}$$

From (4.16), (4.6) and (4.10), we obtain

$$\begin{aligned}\frac{d\upsilon_a(t)}{dt} &= \frac{K_T k_n}{J}i_a(t) - \frac{B}{J}\upsilon_a(t) - \frac{k_n}{J}T_{load}(t)\\ &= 0.2289 i_a(t) - 0.006357\upsilon_a(t) - 1.2715 T_{load}(t)\ .\end{aligned} \tag{7.2}$$

Combining (7.1) and (7.2), the state space representations of the motor are given by,

$$\begin{bmatrix}\dot{i}_a\\ \dot{\upsilon}_a\end{bmatrix} = \begin{bmatrix}-54.3478 & -978.2609\\ 0.2289 & -0.006357\end{bmatrix}\begin{bmatrix}i_a\\ \upsilon_a\end{bmatrix} + \begin{bmatrix}108.6957\\ 0\end{bmatrix}e_a + \begin{bmatrix}0\\ -1.2715\end{bmatrix}T_{load} \tag{7.3}$$

$$y_m = \begin{bmatrix}0 & 1\end{bmatrix}\begin{bmatrix}i_a\\ \upsilon_a\end{bmatrix}\ . \tag{7.4}$$

State space representations of the main resistive coils are derived from (4.20), (4.21), (4.24) and (4.26).

$$P_{in}(t) - \bar{h}A_r(T'_r(t) - T'_a(t)) = V_r c_{pr}\rho_r \frac{dT'_r(t)}{dt} \tag{4.26}$$

$$Q_a = k_a \upsilon_a = 7.85 \times 10^{-3}\upsilon_a \tag{4.21}$$

$$\dot{m}_a = \rho_a Q_a \tag{4.20}$$

$$P_{in}(t) = \rho_a V_a c_{pa}\frac{dT'_a(t)}{dt} + \rho_r V_r c_{pr}\frac{dT'_r(t)}{dt} + \dot{m}_a c_{pa} T'_a(t) \tag{4.24}$$

From (4.26), we obtain

$$\begin{aligned}\frac{dT'_r(t)}{dt} &= -\frac{\bar{h}A_r}{\rho_r V_r c_{pr}}T'_r(t) + \frac{\bar{h}A_r}{\rho_r V_r c_{pr}}T'_a(t) + \frac{1}{\rho_r V_r c_{pr}}P_{in}(t) \\ &= -0.0163T'_r(t) + 0.0163T'_a(t) + 0.0104P_{in}(t)\ .\end{aligned} \tag{7.5}$$

Form (4.20), (4.21), (4.24) and (4.26), we get

$$\begin{aligned}\frac{dT'_a(t)}{dt} &= \frac{\bar{h}A_r}{\rho_a V_a c_{pa}}T'_r(t) + (-\frac{\bar{h}A_r}{\rho_a V_a c_{pa}} - \frac{k_a \upsilon_a}{V_a})T'_a(t) \\ &= 6.3739T'_r(t) - (6.3739 + 37.6282\upsilon_a)T'_a(t)\end{aligned} \tag{7.6}$$

Combining (7.5) and (7.6), the state space representations of the main resistive coils are shown as follows,

$$\begin{bmatrix}\dot{T}'_r \\ \dot{T}'_a\end{bmatrix} = \begin{bmatrix}-0.0163 & 0.0163 \\ 6.3739 & -6.3739 - 37.6282\upsilon_a\end{bmatrix}\begin{bmatrix}T'_r \\ T'_a\end{bmatrix} + \begin{bmatrix}0.0104 \\ 0\end{bmatrix}P_{in} \tag{7.7}$$

$$y_h = \begin{bmatrix}0 & 1\end{bmatrix}\begin{bmatrix}T'_r \\ T'_a\end{bmatrix} \tag{7.8}$$

where υ_a is the air velocity.

The hot air transfer function in the insulated pipe, from Section 4.4, is given by,

$$T = [e^{-0.00581/v_a} T_a + (1 - e^{-0.00581/v_a}) \cdot T_2] e^{-(0.22/v_a)s} . \tag{4.44}$$

If the air velocity of $5\,m/s$ is set for the design of controllers, (4.44) becomes

$$T = [0.9988 T_a + 0.0012 T_2] e^{-0.044s} . \tag{7.9}$$

From Figure 5.6, it is also found that the difference between T and T_a is very small when the air velocity is changing, especially when the air velocity is more than 1 m/s. The range of T_2 is $24 \sim 30\,^oC$ (see Section 4.4). Selecting $T_2 = 30\ ^oC$, then we obtain

$$T = [0.9988 T_a + 0.036] e^{-0.044s} \tag{7.10}$$

which means that

$$T = 0.9988 T_a(t - 0.044) + 0.036 u_s(t - 0.044) \approx 0.9988 T_a(t - 0.044) \tag{7.11}$$

where $u_s(t)$ is a unit step function. Equation (7.11) shows that the difference between T and T_a is a gain approaching 1 and a short time delay.

Thus T_a is substituted by T to simplify the design of the controllers, then (7.7) and (7.8) becomes

$$\begin{bmatrix} \dot{T}_r' \\ \dot{T}' \end{bmatrix} = \begin{bmatrix} -0.0163 & 0.0163 \\ 6.3739 & -6.3739 - 37.6282 v_a \end{bmatrix} \begin{bmatrix} T_r' \\ T' \end{bmatrix} + \begin{bmatrix} 0.0104 \\ 0 \end{bmatrix} P_{in} \tag{7.12}$$

$$y_h = \begin{bmatrix} 0 & 1 \end{bmatrix} \begin{bmatrix} T_r' \\ T' \end{bmatrix} \tag{7.13}$$

where $T' = T - T_0$.

Like the above, if the air velocity is set as $5\,m/s$ for the design of controllers, (7.12) becomes

$$\begin{bmatrix} \dot{T}'_r \\ \dot{T}' \end{bmatrix} = \begin{bmatrix} -0.0163 & 0.0163 \\ 6.3739 & -194.5149 \end{bmatrix} \begin{bmatrix} T'_r \\ T' \end{bmatrix} + \begin{bmatrix} 0.0104 \\ 0 \end{bmatrix} P_{in} \ . \tag{7.14}$$

Thus, controlling T is similar to controlling T' and the heater part subsystem can be represented by (7.14) and (7.13).

In addition, the state space representations of the additional coil are obtained from (4.45), (4.46) and (4.48).

$$Q_{add} = k_{add}\upsilon_{add} = 7.85 \times 10^{-3}\upsilon_a \tag{4.46}$$

$$P_{inadd}(t) - \bar{h}_r A_{radd}(T'_{radd}(t) - T'_{add}(t)) = V_{radd}c_{pr}\rho_r \tfrac{dT'_{radd}(t)}{dt} \tag{4.48}$$

$$\rho_a V_{add}c_{pa}\tfrac{dT'_{add}(t)}{dt} + \rho_r V_{radd}c_{pr}\tfrac{dT'_{radd}(t)}{dt} = P_{inadd}(t) - \rho_a c_{pa}Q_{add}T'_{add}(t) \tag{4.45}$$

From (4.48), we obtain

$$\begin{aligned} \frac{dT'_{radd}(t)}{dt} &= -\frac{\bar{h}_r A_{radd}}{\rho_r V_{radd}c_{pr}}T'_{radd}(t) + \frac{\bar{h}_r A_{radd}}{\rho_r V_{radd}c_{pr}}T'_{add}(t) + \frac{1}{\rho_r V_{radd}c_{pr}}P_{inadd}(t) \\ &= -0.0163T'_{radd}(t) + 0.0163T'_{add}(t) + 0.1468P_{inadd}(t) \ . \end{aligned} \tag{7.15}$$

From (4.45), (4.46) and (4.48), we get

$$\begin{aligned} \frac{dT'_{add}(t)}{dt} &= \frac{\bar{h}_r A_{radd}}{\rho_a V_{add}c_{pa}}T'_{radd}(t) + (-\frac{\bar{h}_r A_{radd}}{\rho_a V_{add}c_{pa}} - \frac{k_{add}\upsilon_{add}}{V_{add}})T'_{add}(t) \\ &= 2.6333T'_{radd}(t) - (2.6333 + 166.6667\upsilon_a)T'_{add}(t) \end{aligned} \tag{7.16}$$

where it is assumed that $\upsilon_{add} = \upsilon_a$. Combining (7.15) and (7.16), the state space representations of the additional coil are given by

$$\begin{bmatrix} \dot{T}'_{radd} \\ \dot{T}'_{add} \end{bmatrix} = \begin{bmatrix} -0.0163 & 0.0163 \\ 2.6333 & -2.6333 - 166.6667\upsilon_a \end{bmatrix} \begin{bmatrix} T'_{radd} \\ T'_{add} \end{bmatrix} + \begin{bmatrix} 0.1468 \\ 0 \end{bmatrix} P_{inadd} \tag{7.17}$$

and

$$y_{add} = \begin{bmatrix} 0 & 1 \end{bmatrix} \begin{bmatrix} T'_{radd} \\ T'_{add} \end{bmatrix} . \tag{7.18}$$

If v_a =5 m/s is set for the design of controllers, (7.17) becomes

$$\begin{bmatrix} \dot{T}'_{radd} \\ \dot{T}'_{add} \end{bmatrix} = \begin{bmatrix} -0.0163 & 0.0163 \\ 2.6333 & -840.9668 \end{bmatrix} \begin{bmatrix} T'_{radd} \\ T'_{add} \end{bmatrix} + \begin{bmatrix} 0.1468 \\ 0 \end{bmatrix} P_{inadd} . \tag{7.19}$$

Thus, the additional coil is represented by (7.19) and (7.18).

The complete state space system of the heat gun is shown in Figure 7.1.

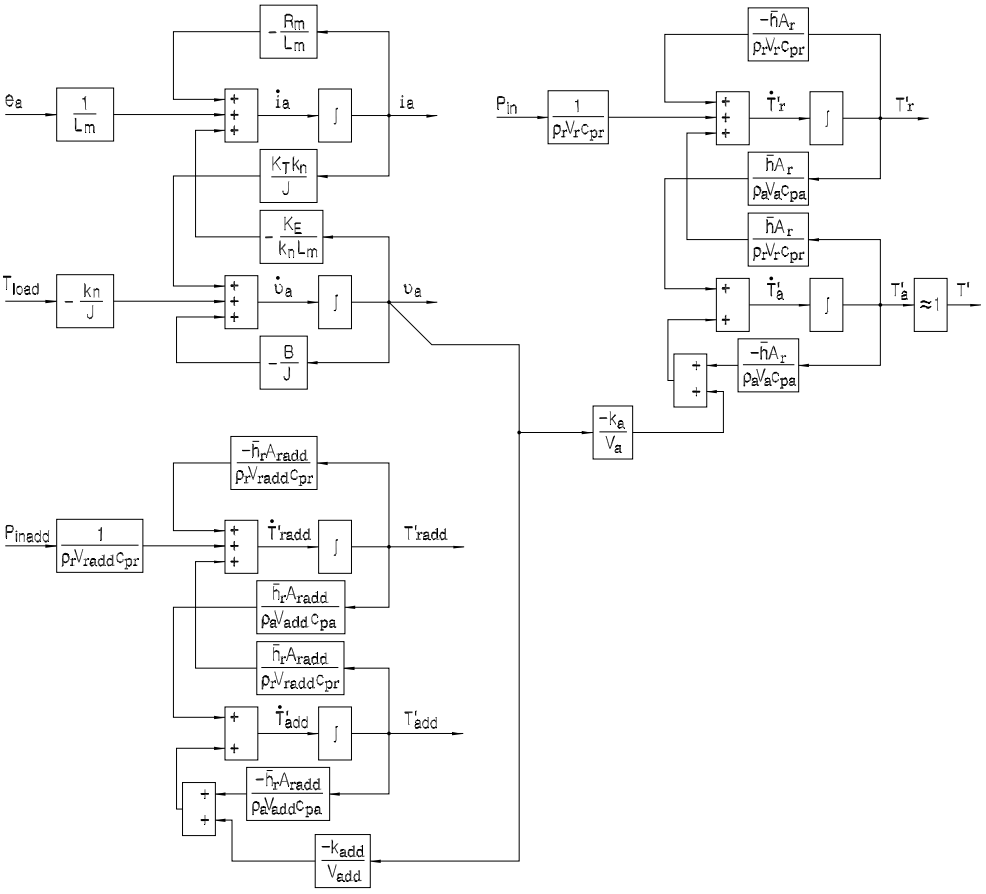

Figure 7.1: The schematic diagram of the heat gun system

All the above state space models of the subsystems can be written in the following forms,

$$\begin{aligned} \dot{x} &= Ax + Bu \\ y &= Cx \end{aligned}$$

where x is the state vector, y is the output and u is the control input of the system.

The above state space models are now used to design state feedback control, LQR and LQG for the heat gun. In these control methods, the control command is given by

$$u = -Kx$$

where K is the feedback gain.

7.3 State Feedback Control

Firstly, the state feedback controller is designed by using the pole placement method (Franklin *et al.*, 1994). K is chosen so as to place the poles of the system to match the desired ones by using $u = -Kx$. In order to achieve a zero steady state error, an integrator is added. Let the error equation be

$$\dot{f} = e = r - Cx \tag{7.20}$$

where r is the reference signal.

7.3.1 State Feedback Control for the Heat Gun

By using the integrator shown in (7.20), the matrices shown in (7.3) and (7.4) becomes augmented matrices of order three. The augmented representations of

the motor are as follows,

$$\begin{bmatrix} \dot{i}_a \\ \dot{v}_a \\ \dot{f}_m \end{bmatrix} = \begin{bmatrix} -54.3478 & -978.2609 & 0 \\ 0.2289 & -0.006357 & 0 \\ 0 & -1 & 0 \end{bmatrix} \begin{bmatrix} i_a \\ v_a \\ f_m \end{bmatrix} + \begin{bmatrix} 108.6957 \\ 0 \\ 0 \end{bmatrix} e_a + \begin{bmatrix} 0 \\ -1.2715 \\ 0 \end{bmatrix} T_{load} + \begin{bmatrix} 0 \\ 0 \\ 1 \end{bmatrix} r_m \quad (7.21)$$

$$y_m = \begin{bmatrix} 0 & 1 & 0 \end{bmatrix} \begin{bmatrix} i_a \\ v_a \\ f_m \end{bmatrix} . \quad (7.22)$$

Setting the desired dominant poles for the motor as given by the solutions of $s^2 + 2\zeta\omega_n s + \omega_n^2 = s^2 + 8s + 25 = 0$, where $\zeta = 0.8$ and $\omega_n = 5$ ensure that the settling time is less than $2\,sec$ and the maximum overshoot is less than 5%. In addition, setting the third pole at $s = -60$, we obtain

$$K_m = \begin{bmatrix} 0.1255 & 11.2797 & -60.2883 \end{bmatrix}.$$

For the heating process, with the integrator shown in (7.20), (7.14) and (7.13) becomes an augmented system shown in (7.23) and (7.24).

$$\begin{bmatrix} \dot{T}_r' \\ \dot{T}' \\ \dot{f}_h \end{bmatrix} = \begin{bmatrix} -0.0163 & 0.0163 & 0 \\ 6.3739 & -194.5149 & 0 \\ 0 & -1 & 0 \end{bmatrix} \begin{bmatrix} T_r' \\ T' \\ f_h \end{bmatrix} + \begin{bmatrix} 0.0104 \\ 0 \\ 0 \end{bmatrix} P_{in} + \begin{bmatrix} 0 \\ 0 \\ 1 \end{bmatrix} r_h \quad (7.23)$$

$$y_h = \begin{bmatrix} 0 & 1 & 0 \end{bmatrix} \begin{bmatrix} T_r' \\ T' \\ f_h \end{bmatrix} . \quad (7.24)$$

Similarly, if the desired dominant poles for the heater part are given by the solutions of $s^2 + 10s + 25 = 0$ and the third pole is equal to -190, we derive the feedback gain

$$K_{h1} = \begin{bmatrix} 525.85 & 12945.98 & -71656.41 \end{bmatrix}$$

for the heater part. However, the response of the air temperature using this K_{h1} has large oscillations because $0\,W \leq P_{in} \leq 7000\,W$ is set. Therefore, the requirement of a fast response needs to be relaxed so as to reduce the power input.

Thus, the eigenvalues of the original heater subsystem should not be changed too much by the state feedback controller so as to reduce the input expense. The eigenvalues of the original heater part are -194.5154 and -0.0158. Moreover, the settling time is required to improve from $230\,sec$ to $110\,sec$, thus -0.035 is chosen as an eigenvalue for the design of the state feedback controller. If the desired poles for the heater part are given by the solutions of $(s + 194.5)(s + 0.035)^2 = 0$, we obtain

$$K_{h2} = \begin{bmatrix} 3.7308 & 45.2921 & -3.5943 \end{bmatrix}.$$

By using the state feedback controllers with the parameters of K_m and K_{h2}, the responses of the motor and heater parts are shown in Figure 7.2 where the limit of P_{in} is $0 \sim 7000\ W$ and the set points of υ_a and T are $5\,m/s$ and 140^oC respectively.

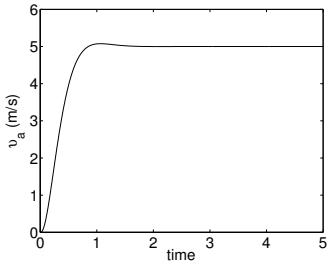

(a) υ_a

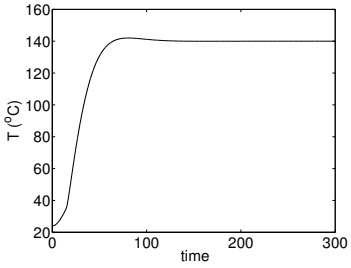

(b) T with heat recycle

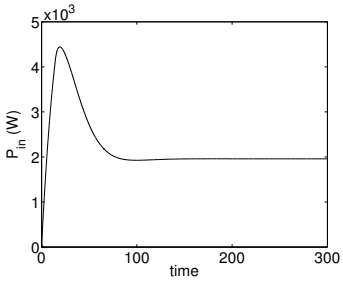

(c) P_{in} with heat recycle

Figure 7.2: Responses of the motor and heater parts by using K_m and K_{h2}

From Figure 7.2(a), it is observed that the maximum overshoot is less than $0.25m/s$ or 5% and the settling time is less than 2 sec. From Figure 7.2(b), it is observed that the maximum overshoot is less than 2^oC or 1.4% and the settling time is less than 110 sec. Figures 7.2 shows that the responses of the air velocity and temperature meet the requirements of control by using the state feedback controllers.

By using the state feedback controllers with the above K_m and K_{h2}, if $T_{load} = 1\,N.m$ is added at time $300\,sec$, the responses are shown in Figure 7.3. While the set points of υ_a and T are changed from $5\,m/s$ to $7\,m/s$ at $500\,sec$ and from $140\,^oC$ to $150\,^oC$ at $700\,sec$ respectively, the responses of these parts are shown in Figure 7.4.

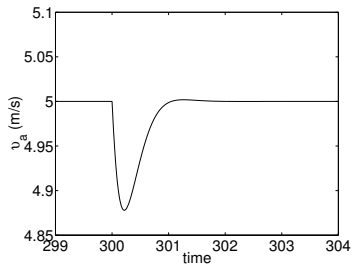

(a) υ_a

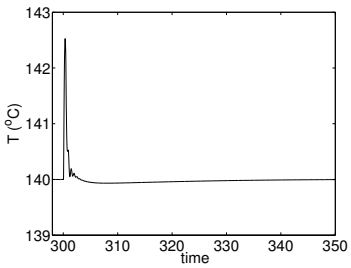

(b) T

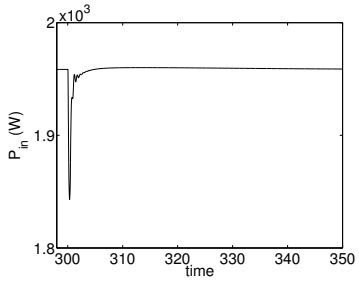

(c) P_{in}

Figure 7.3: Responses of the motor and heater parts to T_{load}

From Figures 7.3 and 7.4, it is observed that the responses of υ_a and T to load disturbance and set point changes meet the requirements of control except that the maximum overshoot of T caused by T_{load} is quite high. This will be investigated in Section 7.3.2.

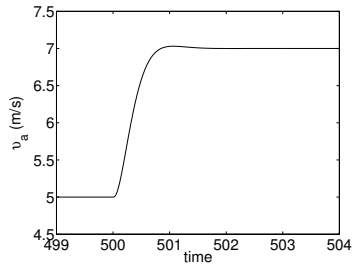

(a) υ_a

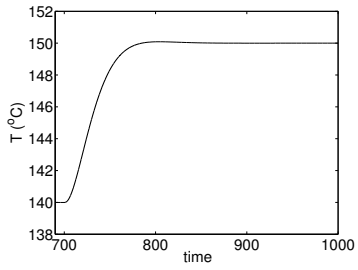

(b) T

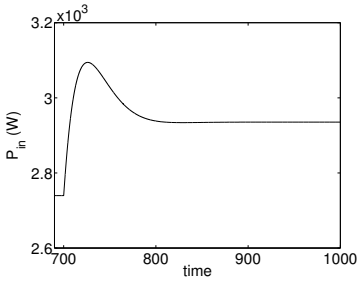

(c) P_{in}

Figure 7.4: Responses of the motor and heater parts to the changes of set points

For the additional coil, like the heating process, the integrator shown in (7.20) is also added to achieve zero steady state error. The matrices shown in (7.19) and (7.18) become the augmented matrices written as follows:

$$\begin{bmatrix} \dot{T}'_{radd} \\ \dot{T}'_{add} \\ \dot{f}_{add} \end{bmatrix} = \begin{bmatrix} -0.0163 & 0.0163 & 0 \\ 2.6333 & -835.9668 & 0 \\ 0 & -1 & 0 \end{bmatrix} \begin{bmatrix} T'_{radd} \\ T'_{add} \\ f_{add} \end{bmatrix} + \begin{bmatrix} 0.1468 \\ 0 \\ 0 \end{bmatrix} P_{inadd} + \begin{bmatrix} 0 \\ 0 \\ 1 \end{bmatrix} r_{add} \tag{7.25}$$

$$y_m = \begin{bmatrix} 0 & 1 & 0 \end{bmatrix} \begin{bmatrix} T'_{radd} \\ T'_{add} \\ f_{add} \end{bmatrix} . \tag{7.26}$$

Similar to the state feedback control design for the heating process, $0\,W \leq P_{inadd} \leq 200\,W$ is also considered. The eigenvalues of the additional coil, shown in (7.19) and (7.18), are -836 and -0.0163. The desired poles are set as the solutions of $(s + 836)(s + 1)^2 = 0$ where $s = -1$ ensures that the settling time is less than

50 *sec*, we get

$$K_{add} = \begin{bmatrix} 13.5 & 17.4 & -2162.5 \end{bmatrix}$$

for the additional coil. If v_a =5 m/s, T = 140 ^oC and the temperature difference between T_{inadd} and T_{cen} is required to reduce by half (see Section 4.5.1), the setting of T_{add} is 140.17 ^oC. The response of this part is shown in Figure 7.5 by using the the state feedback controller with the above K_{add}. From Figure 7.5, it is found

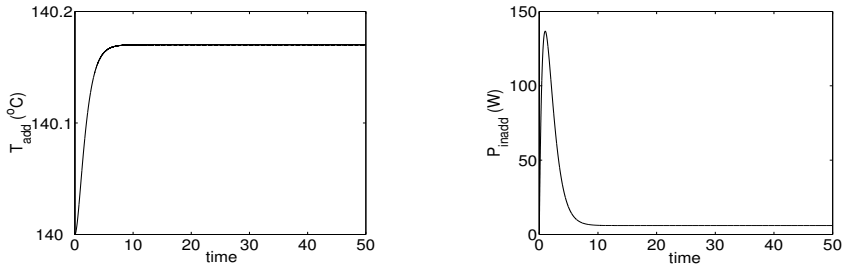

(a) T_{add} (b) P_{inadd}

Figure 7.5: Response of the additional coil by using state feedback control

that the response meets the requirements of control (see Section 7.1).

When the air velocity changes from 5 m/s to 7 m/s, where the set point of T_{add} is 140.13 ^oC, at time of 200 *sec*, and T changes from 140 ^oC to 150 ^oC, where the set point of T_{add} is 150.13 ^oC, at time 400 sec, then the responses of this part are shown in Figure 7.6 by using the above same state feedback controller. Figure 7.6(c) is the amplification of part of Figure 7.6(b). From Figure 7.6, it is found that the responses of T_{add} to the changes of the set point and v_a meet the requirements of control.

7.3.2 Disturbance Rejection

From Figure 7.3(a) and Figure 7.3(b), it is observed that the influence of T_{load} is quite significant. Ways are needed to reduce it. According to the motor equations in (7.21) and (7.22), by using the state feedback controller, the transfer function

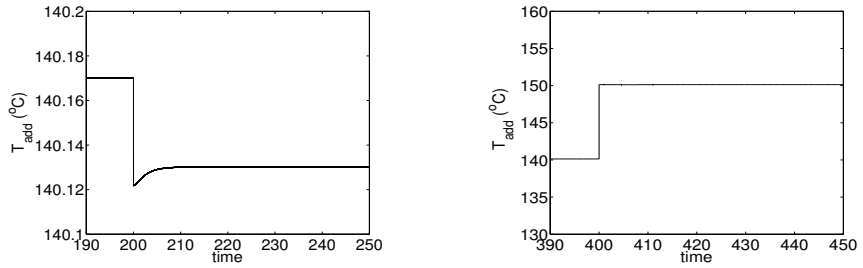

(a) T_{add} (b) T_{add}

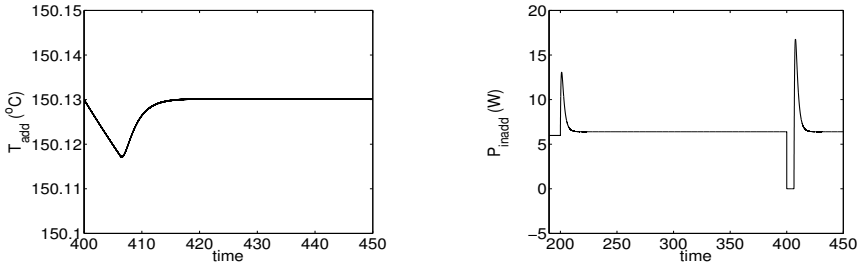

(c) T_{add} (d) P_{inadd}

Figure 7.6: Responses of the additional coil to the changes on the set point and υ_a

between T_{load} and the output, y_m (υ_a), is given by

$$Y_m(s) = C(sI - A + BK)^{-1}DT_{load}(s) \tag{7.27}$$

where $A = \begin{bmatrix} a_{11} & a_{12} & 0 \\ a_{12} & a_{22} & 0 \\ 0 & -1 & 0 \end{bmatrix} = \begin{bmatrix} -54.3478 & -978.2609 & 0 \\ 0.2289 & -0.006357 & 0 \\ 0 & -1 & 0 \end{bmatrix}$, $B = \begin{bmatrix} b \\ 0 \\ 0 \end{bmatrix} = \begin{bmatrix} 108.6957 \\ 0 \\ 0 \end{bmatrix}$,

$D = \begin{bmatrix} 0 \\ d \\ 0 \end{bmatrix} = \begin{bmatrix} 0 \\ -1.2715 \\ 0 \end{bmatrix}$, $C = \begin{bmatrix} 0 & 1 & 0 \end{bmatrix}$ and $K = \begin{bmatrix} k_1 & k_2 & k_3 \end{bmatrix}$.

Substituting these A, B, C, D and K into (7.27), we obtain

$$\frac{Y_m(s)}{T_{load}(s)} = \frac{ds(s - a_{11} + bk_1)}{s^3 + (-a_{11} + bk_1 - a_{22})s^2 + (a_{11}a_{22} - a_{22}bk_1 - a_{12}a_{21} + a_{21}bk_2)s - a_{21}bk_3}. \tag{7.28}$$

There is a zero at $s = -(-a_{11} + bk_1)$. Choosing K by using the pole placement method, the denominator of (7.28) can be arbitrarily changed to the form

$$(s + f)(s^2 + 2\zeta\omega_n s + \omega_n^2) \tag{7.29}$$

where positive f is far bigger than the dominant poles which are determined by ζ and ω_n. By comparing the denominator of (7.28) and (7.29), we obtain

$$(-a_{11} + bk_1) - a_{22} = 2\zeta\omega_n + f \ . \tag{7.30}$$

It is known that large magnitude of zero leads to small oscillation (Franklin *et al.*, 1994). Thus, large ζ, ω_n and f are chosen to make the magnitude of $(-a_{11}+bk_1)$ larger so as to reduce the oscillation caused by T_{load}. The effect of reducing the oscillation by increasing ζ, ω_n and f for the motor is shown in Figures 7.7(a) and 7.7(c) where the set points of v_a and T are $5\,m/s$ and 140^oC respectively, $T_{load} = 1\,N.m$ is added at time of $300\,sec$ and K_{h2} in Section 7.3.1 is used for the heating process. Figures 7.7(b) and 7.7(d) are responses of v_a and T respectively

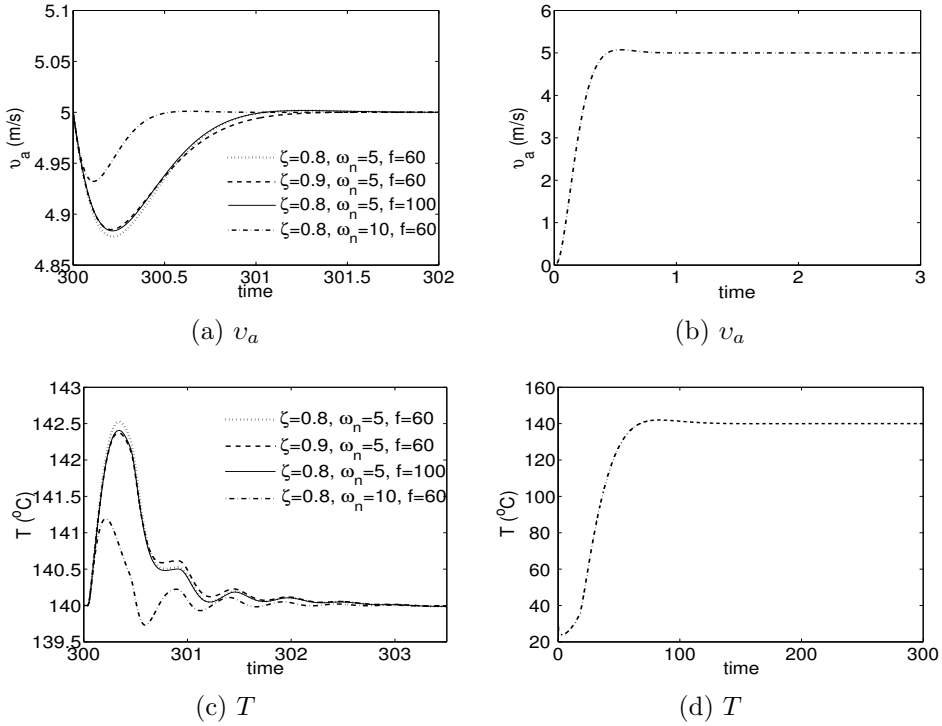

(a) v_a (b) v_a

(c) T (d) T

Figure 7.7: Responses of the motor and heater parts to T_{load}

by choosing $\zeta = 0.8$, $\omega_n = 10$ and $f = 60$ for the state feedback control design of the motor. ζ, ω_n and f are not changed for the heating process because these

changes will lead to actuator saturation. From Figure 7.7, it is found that the responses of v_a and T to T_{load} meet the requirements of control if $\zeta = 0.8$, $\omega_n = 10$ and $f = 60$ are selected for the state feedback control design of the motor.

It is observed that the oscillations caused by T_{load} in Figures 7.7(a) and 7.7(c) are much better than those shown in Figures 7.3(a) and 7.3(b) respectively.

When the set points of v_a and T are changed from $5\,m/s$ to $7\,m/s$ at $500\,sec$ and from $140\,^oC$ to $150\,^oC$ at $700\,sec$ respectively, the responses are shown in Figure 7.8. Comparing Figure 7.4(a) with Figure 7.8(a), it is found that when

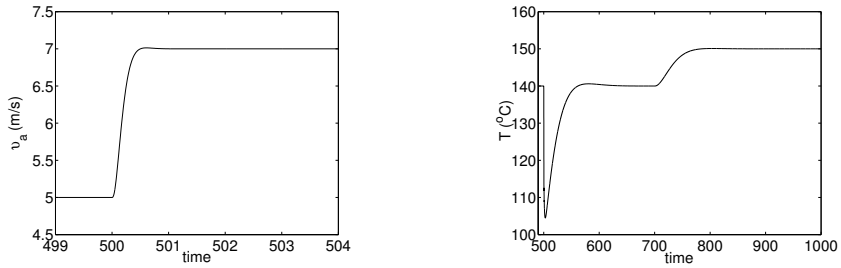

(a) v_a (b) T

Figure 7.8: Responses of the motor and heater parts to the changes of the set points

the set point is changed, the response becomes faster and the maximum overshoot becomes smaller after a larger ω_n is chosen.

In the design of the state feedback controller, the cost of the input is not considered so that the transient response does not follow the desired one because the desired input cannot be realized.

Thus, the LQR method which considers the cost of the input will be used to design the controllers for the heat gun in the next section.

7.4 LQR

Like Section 7.3, an augmented system is used to achieve zero steady state error. Thus, when the LQR method is used to design controllers for the heat gun, the

state space models of the augmented subsystems shown in Section 7.3.1 are also used here. The optimal gain matrix, K, is calculated so that the state-feedback law $u = -Kx$ minimizes the quadratic cost function in (7.31).

$$J = \int_0^\infty (x^T Q x + u^T r u) dt \tag{7.31}$$

where Q is a positive-definite (or positive-semidefinite) Hermitian or real symmetric matrix and r is a positive-definite Hermitian or real symmetric matrix (Ogata, 2002). When choosing Q for (7.31), the ratios among q_{11}, q_{22} and q_{33}, which are diagonal elements of Q, are decided by the control requirements discussed in Section 7.1. q_{11}, q_{22} and q_{33} are weights corresponding to x_1, x_2, x_3, which are the elements of state vector. r is the weighting on the control effort, u. The error, x_3, is given the highest priority in the design of the controller. Therefore, this leads to big ratios of q_{33} vs r, q_{33} vs q_{11}, and q_{33} vs q_{22}.

For the motor part, choosing

$$Q_m = \begin{bmatrix} 0 & 0 & 0 \\ 0 & 1 & 0 \\ 0 & 0 & 1000 \end{bmatrix} \text{ and } r_m = [0.001],$$

we obtain

$$K_m = \begin{bmatrix} 0.2634 & 79.0257 & -1000 \end{bmatrix}.$$

In selecting Q_m, $q_{m33} = 1000$ is much bigger than $q_{m22} = 1$ and $q_{m11} = 0$ which means paying more attention on the error than on v_a and i_a. $r_m = 0.001$ is only a small weight on the control effort, u.

For the heating process, the ratio among q_{11}, q_{22}, q_{33} and r implies the relative weights of T_r, T, error and the control input. If r_h is selected too small, it will lead to extremely high magnitude of the power input which may not be realizable in reality. Thus, for the heater part, the weight on the input power is increased

and the error is also considered simultaneously. For the heater part, the weighting matrices are set as

$$Q_h = \begin{bmatrix} 1 & 0 & 0 \\ 0 & 1 & 0 \\ 0 & 0 & 100 \end{bmatrix} \text{ and } r_h = [30].$$

With these, the feedback gain is obtained as

$$K_h = \begin{bmatrix} 2.2038 & 0.0096 & -1.8257 \end{bmatrix}.$$

We set the desired υ_a as 5 m/s and the desired T as 140 ^oC. The closed-

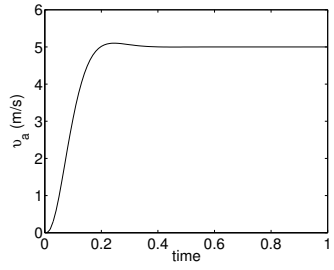

(a) υ_a

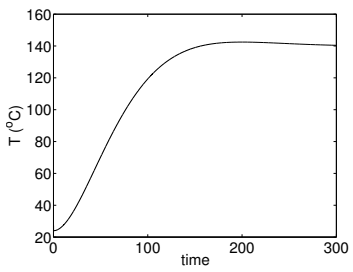

(b) T without heat recycle

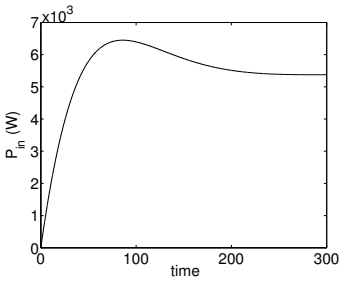

(c) P_{in} without heat recycle

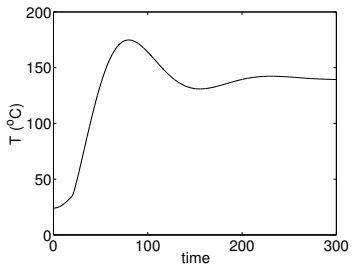

(d) T with heat recycle

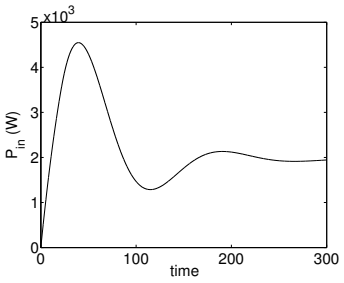

(e) P_{in} with heat recycle

Figure 7.9: Responses of the motor and the heater parts by using LQR

loop responses of the motor and heater parts using the LQR approach are shown

in Figure 7.9 where $0\,W \leq P_{in} \leq 7000\,W$. When the heat recycle is used, P_{in} decreases greatly while the oscillation of T becomes higher (see Figures 7.9(d) and 7.9(e)).

From Figure 7.9(d), it is seen that the heat recycle has a significant effect on the response. Thus the influence of heat recycle needs to be reduced. It was investigated in Section 4.6 that P_c, the internal energy transferred into the chamber by the heat recycle, is given by

$$P_c = \mu \rho_a c_{pa} Q_{ac} T_c \tag{7.32}$$

where μ, ρ_a , c_{pa}, T_c and Q_{ac} were also introduced in Section 4.6. T_c is the temperature of the recycled air and Q_{ac} is the air flow rate in the recycle path. If T_c and Q_{ac} at the heat recycle pipe's outlet are measurable, we may consider cancelling the influence of the heat recycle by modifying the control effort to

$$u = -Kx - P_c \ . \tag{7.33}$$

The response of the heater part is shown in Figure 7.10 by using the modified control command in (7.33) instead of $u = -Kx$. From Figure 7.10(a), it is observed

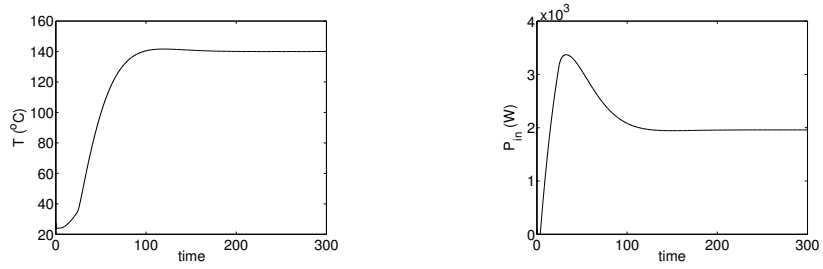

(a) T (b) P_{in}

Figure 7.10: Response of the heater part by using (7.33)

that the oscillation is greatly decreased by using (7.33).

If $T_{load} = 1\,N.m$ is added at time $300\,sec$, while the set points of v_a and T

are changed from $5\,m/s$ to $7\,m/s$ at $400\,sec$ and from $140\,^oC$ to $150\,^oC$ at $700\,sec$ respectively, the responses are shown in Figure 7.11.

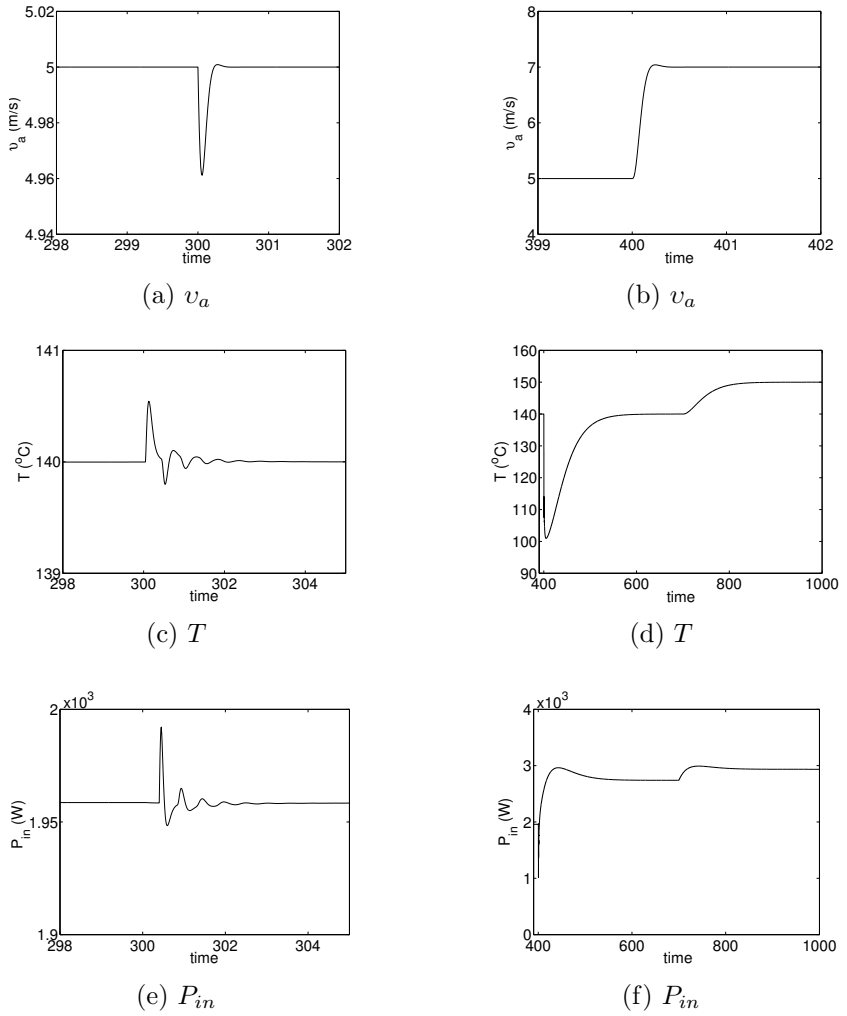

(a) υ_a (b) υ_a

(c) T (d) T

(e) P_{in} (f) P_{in}

Figure 7.11: Responses of the motor and heater parts to the changes on set points and T_{load}

Comparing the responses in Figure 7.11 with those in Figures 7.7, it is observed that the oscillations caused by T_{load} is greatly decreased by using the LQR method. The weighting on the error has improved the design.

For the additional coil, we set

$$Q_{add} = \begin{bmatrix} 0 & 0 & 0 \\ 0 & 1 & 0 \\ 0 & 0 & 1000 \end{bmatrix} \text{ and } r_{add} = [0.001].$$

This gives

$$K_{add}=\begin{bmatrix}6.44 & 1.20 & -1000\end{bmatrix}.$$

If v_a =5 m/s, $T = 140\ ^oC$ and the temperature difference between T_{inadd} and T_{cen} is required to reduce by half (see Section 4.5.1), the set point of T_{add} is $140.17\,^oC$. The response is shown in Figure 7.12, where the power input to the additional coil is nonnegative, by using the above parameters.

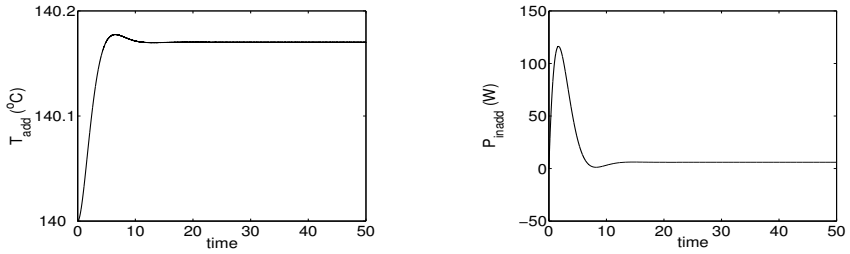

(a) T_{add} (b) P_{inadd}

Figure 7.12: Response of the additional coil by using LQR

When the air velocity changes from $5\,m/s$ to $7\,m/s$, where the set point of T_{add} is $140.13\,^oC$, at time of $200\,sec$, and T changes from $140\,^oC$ to $150\,^oC$, where the set point of T_{add} is $150.13\,^oC$, at time of 400 sec, the response is shown in Figure 7.13 by using the above same parameters in the LQR controller. Figure 7.13(c) is the amplification of part of Figure 7.13(b). We see that the oscillation and settling time in Figures 7.12(a), 7.13(a) and 7.13(c) meet the requirements.

7.5 LQG

In the above closed-loop control, the data fedback were assumed to be measurable. But not all the states, which include the temperature of the resistive wires, are easily measured. Besides, measurement noise will also influence the results of the control. In this section, the LQG method is investigated.

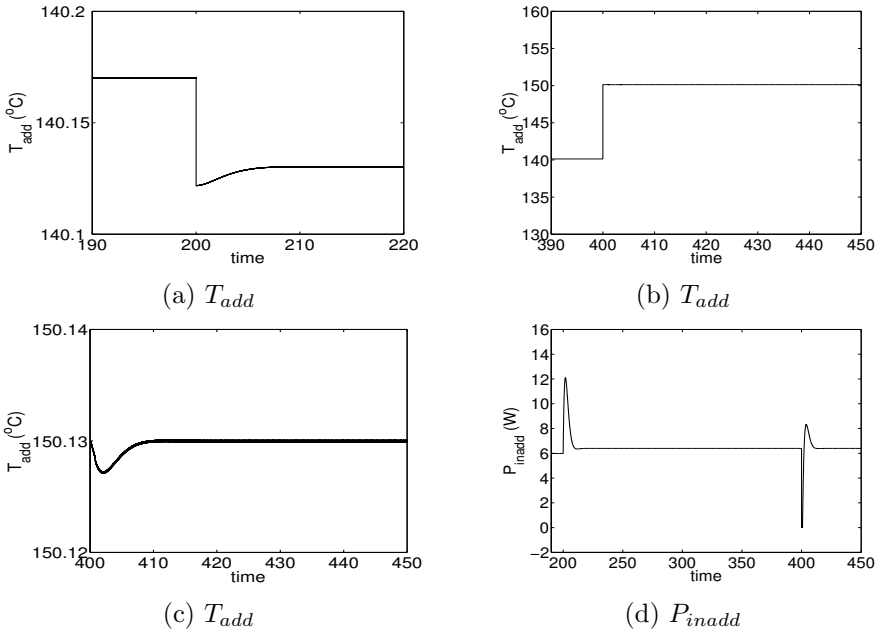

(a) T_{add} (b) T_{add}

(c) T_{add} (d) P_{inadd}

Figure 7.13: Response of the additional coil to the changes on the set points and υ_a

In the design of the LQG controller, the integrator of (7.20) is also included. Thus the transfer functions of the augmented subsystems shown in Section 7.3.1 are used for designing the controller. The control command is given by

$$u = -Kx.$$

As to the controller gains, K, the parameters obtained in Section 7.4 are used here because the controller gain is chosen to minimize the cost function of (7.34) (see (7.31)) in the LQG method (Skogestad and Postlethwaite, 1996).

$$J = E\{\lim_{T\to\infty} \frac{1}{T} \int_0^T (x^T Q x + u^T r u) dt\} \tag{7.34}$$

In the LQG design, the observer gain, K_o, is chosen by using the Kalman filter method. K_o is chosen to minimize $E\{[x - \hat{x}]^T [x - \hat{x}]\}$ where $\hat{x}$ is the estimated states of the system (Skogestad and Postlethwaite, 1996). The estimator is given by

$$\dot{\hat{x}} = A\hat{x} + Bu + K_o(y - C\hat{x}) \tag{7.35}$$

where x is the state vector.

7.5.1 LQG Design for the Heat Gun

To begin with, the observability of the DC motor system is checked. The observability matrix for the augmented matrices shown in (7.21) and (7.22) is

$$ob_m = \begin{bmatrix} C \\ CA \\ CA^2 \end{bmatrix} = \begin{bmatrix} 0 & 1 & 0 \\ 0.2289 & -0.0064 & 0 \\ -12.4417 & -223.9239 & 0 \end{bmatrix}. \tag{7.36}$$

The rank of ob_m is 2. Thus the motor system described by the augmented matrices is unobservable. Then the observability of the matrices (without augmentation) shown in (7.3) and (7.4) is checked. The new observability matrix is

$$ob_m = \begin{bmatrix} C \\ CA \end{bmatrix} = \begin{bmatrix} 0 & 1 \\ 0.2289 & -0.0064 \end{bmatrix}. \tag{7.37}$$

The rank of the new observability matrix is 2.

So, when the estimator for the motor part is being established, the augmented system is not used while the state space matrices of the system shown in (7.3) and (7.4) are used.

For the Kalman filter of the motor part, selecting

$$Q_{om} = \begin{bmatrix} 1 & 0 \\ 0 & 1 \end{bmatrix} \text{ and } r_{om} = \begin{bmatrix} 1 \end{bmatrix}$$

which means weighting both the process noise and measurement noise equally, we get

$$K_{om} = \begin{bmatrix} -2.1447 & 0.1285 \end{bmatrix}^T.$$

Like the motor, the observability of the heater part is firstly checked. The observability matrix for the augmented heater system in (7.23) and (7.24) is as follows,

$$ob_h = \begin{bmatrix} C \\ CA \\ CA^2 \end{bmatrix} = \begin{bmatrix} 0 & 1 & 0 \\ 6.37 & -194.51 & 0 \\ -1239.92 & 37836.15 & 0 \end{bmatrix} . \tag{7.38}$$

The rank of this ob_h is 2. The augmented system is unobservable. Thus the matrices shown in (7.14) and (7.13) are used to check observability. The new observability matrix for the heater part is

$$ob_h = \begin{bmatrix} C \\ CA \end{bmatrix} = \begin{bmatrix} 0 & 1 \\ 6.37 & -194.51 \end{bmatrix} . \tag{7.39}$$

The rank of the new observability matrix is 2. Therefore, the matrices in (7.14) and (7.13) are used to build the estimator for the heater part.

For the observer of the heater part, selecting

$$Q_{oh} = \begin{bmatrix} 1 & 0 \\ 0 & 1 \end{bmatrix} \text{ and } r_{oh} = \begin{bmatrix} 0.1 \end{bmatrix},$$

we obtain

$$K_{oh} = \begin{bmatrix} 2.7173 & 0.1147 \end{bmatrix}^T .$$

When the motor and heater parts are simulated together, the states, υ_a and T, fedback into the controllers are real values because these states are measurable outputs, y. Other states which are fedback to the controllers are replaced by their estimated values.

We set the desired T as 140 ^oC and the desired υ_a as 5 m/s. The responses of the motor and heater parts by using the LQG method are shown in Figure 7.14 where T_{Load}=1 $N.m$ is added at 300 sec.

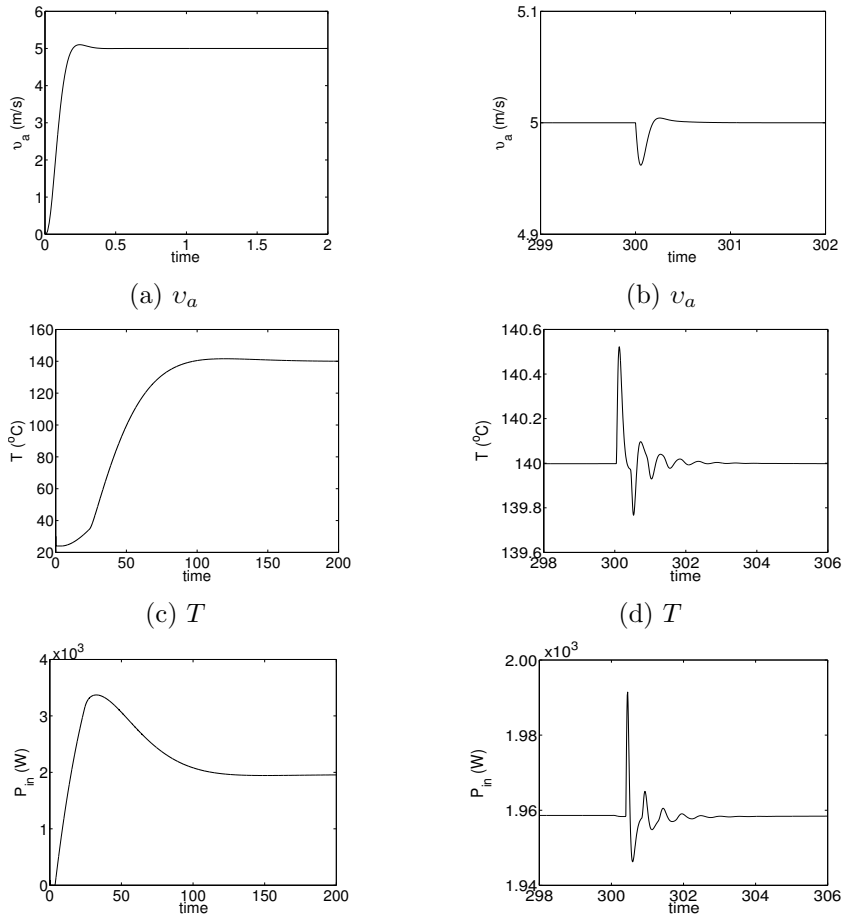

(a) υ_a (b) υ_a

(c) T (d) T

(e) P_{in} (f) P_{in}

Figure 7.14: Responses of the motor and heater parts by using the LQG controllers

From Figure 7.14, it is observed that the responses of υ_a and T meet the control objectives in Section 7.1.

For the observer of the additional coil subsystem, the state space model in (7.19) and (7.18) is used to design the observer. Selecting

$$Q_{oadd} = \begin{bmatrix} 1 & 0 \\ 0 & 1 \end{bmatrix} \text{ and } r_{oadd} = \begin{bmatrix} 0.1 \end{bmatrix}$$

which means weighting $\hat{T}_{radd}$ and $\hat{T}_{add}$ equally, we get

$$K_{oadd} = \begin{bmatrix} 0.8921 & 0.0088 \end{bmatrix}.$$

For the control effort, $u = -K_{add}x$, K_{add} is the same as in Section 7.4. T_{add} and estimated $\hat{T}_{radd}$ are used to calculate the control command. If υ_a =5 m/s, $T = 140$

^oC and the temperature difference between T_{inadd} and T_{cen} is required to reduce by half (see Section 4.5.1), the set point of T_{add} is $140.17\,^oC$. The response of this part is shown in Figure 7.15, where the power input to the additional coil is nonnegative.

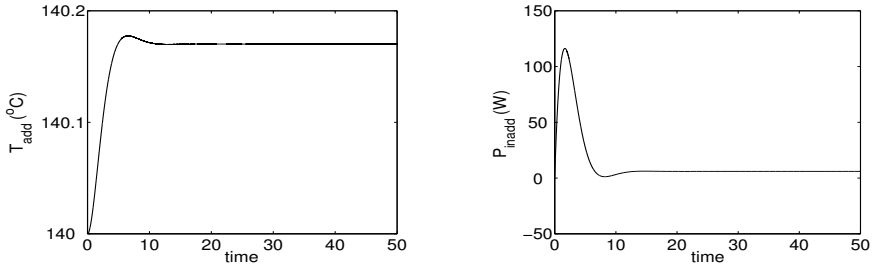

(a) T_{add} (b) P_{inadd}

Figure 7.15: Response of the additional coil by using LQG

When the air velocity changes from $5\,m/s$ to $7\,m/s$, where the set point of T_{add} is $140.13\,^oC$, at time $200\,sec$, and T changes from $140\,^oC$ to $150\,^oC$, where the set point of T_{add} is $150.13\,^oC$, at time $400\,sec$, then the response of this part is shown in Figure 7.16 by using the same LQG controller. Figure 7.16(c) is the amplification of part of Figure 7.16(b). From Figures 7.15 and 7.16, it is observed that the response has a settling time and maximum overshoot which are less than $10\,sec$ and $0.2\,^oC$ respectively and the steady state error is zero.

7.5.2 Measurement Noise

In reality, the output of the sensor is always effected by the measurement noise whose influence can be reduced by the observers. The measurement noise, assumed to be white noise having a power spectral density of 0.1, is added to the sensor of the output air temperature, T, to test the performance of the observer. By using the LQG method, the response of the heater part under the above measurement noise is shown in Figure 7.17. In this process, $\hat{T}$ and $\hat{T}_r$ are used to calculate the control command instead of T and T_r. K_h, K_{oh}, K_m and K_{om} are the same as those

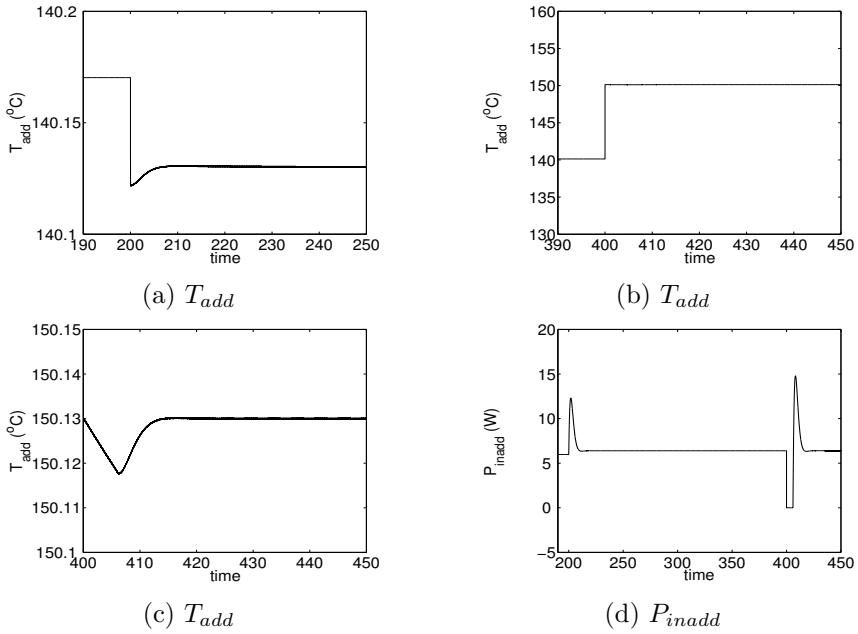

(a) T_{add} (b) T_{add}

(c) T_{add} (d) P_{inadd}

Figure 7.16: Response of the additional coil to the changes of set points

in Section 7.5.1, and the set points for T and v_a are 140^oC and $5\,m/s$ respectively.

The output from the air temperature sensor is shown in Figure 7.17(a). $\hat{T}$ from the observer is shown in Figure 7.17(b). The real values of T are shown in Figure

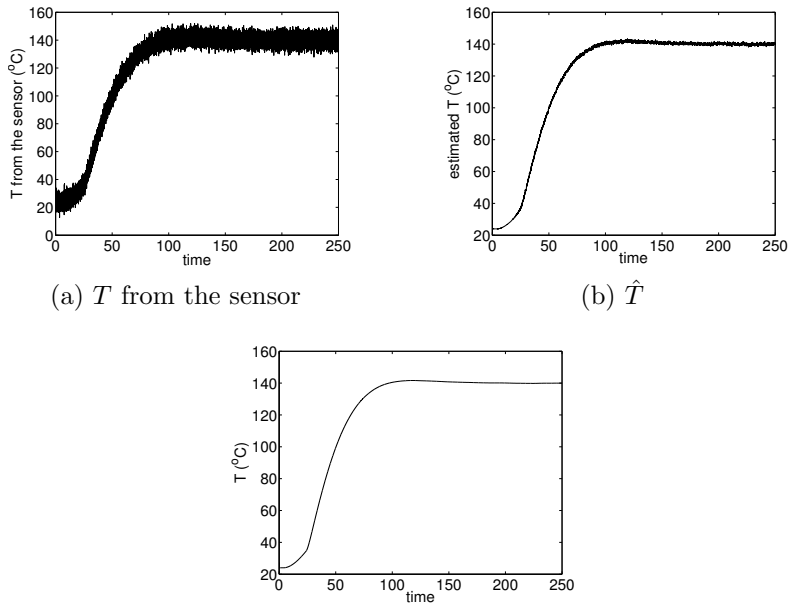

(a) T from the sensor (b) $\hat{T}$

(c) T

Figure 7.17: The effect of LQG on measurement noise

7.17(c). It is observed that the difference between $\hat{T}$ and T is very small, indicating that the Kalman filter can optimally estimate the state of the system even if there is measurement noise.

7.6 Actuator Saturation

From the above discussion, it is clear that the power input to the resistive coils and the additional coil cannot be negative. In reality, the magnitude can not be extremely high either. Thus there is the problem of actuator saturation. In this section, the method suggested by Emami-Naeini *et al.* (Dec. 1994) is developed for the heater part.

The discrete state space transfer function of the heater part is introduced for this application. When the air velocity is 5 m/s, the heater model in (7.14) and (7.13) written in the discrete state space form are as follows:

$$\begin{bmatrix} T_r'(k+1) \\ T'(k+1) \end{bmatrix} = \begin{bmatrix} 0.9984219 & 8.367 \times 10^{-5} \\ 0.0327191 & 2.746 \times 10^{-6} \end{bmatrix} \begin{bmatrix} T_r'(k) \\ T'(k) \end{bmatrix} + \begin{bmatrix} 0.00103918 \\ 3.23 \times 10^{-5} \end{bmatrix} P_{in}(k) \tag{7.40}$$

$$y_h(k) = \begin{bmatrix} 0 & 1 \end{bmatrix} \begin{bmatrix} T_r'(k) \\ T'(k) \end{bmatrix} \tag{7.41}$$

where the sample time is 0.1 *sec* and a *zero order hold* is used.

The method makes the system track a reference of $y(k) = r(k)$ for all $k \geq N$ where N is an integer to be decided later.

The discrete transfer function of a stable system can be written as

$$P(z) = C(zI - A)^{-1}B = \sum_{i=1}^{2} \frac{H_i}{z - \lambda_i} \tag{7.42}$$

where $|\lambda_i| < 1$ is a pole of the discrete transfer function.

The input u can be divided into two parts: an N-tap Finite Impulse Response

(FIR) filter and a steady-state part, $U_{ss}(z)$,

$$U(z) = U_{FIR}(z) + U_{ss}(z) \ . \tag{7.43}$$

Then the input may be expressed as

$$U(z) = \sum_{i=0}^{N} p_i z^{-i} + \hat{p}\frac{z^{-N}}{z-1} \tag{7.44}$$

where p_i and $\hat{p}$ are inputs at different steps and the second term of the right hand side of (7.44) is a delayed step. The term $\sum_{i=0}^{N} p_i z^{-i}$ vanishes after N steps. Thus the input becomes

$$u(k) = \sum_{k=0}^{N} p_k \delta_k + \hat{p}1(k-N-1) \ . \tag{7.45}$$

The output can also be divided into two parts: an N-tap FIR and a steady-state part as follows

$$Y(z) = C(zI - A)^{-1}BU(z) = Y_{FIR}(z) + Y_{ss}(z) \ . \tag{7.46}$$

The desired steady-state output is

$$Y_{ss}(z) = \frac{z}{z-1}r \tag{7.47}$$

where r is a constant reference. Substituting (7.44) and (7.47) into (7.46) and equating the residues for the system poles, $z = \lambda_i$, and the pole of the input signal at $z = 1$, we obtain, for $z = 1$,

$$\sum_{i=1}^{2} \frac{H_i}{1-\lambda_i}\hat{p} = r \tag{7.48}$$

where H_i is shown in (7.42), and each λ_j satisfies

$$\sum_{i=0}^{N} H_j \lambda_j^{-i} p_i + H_j \frac{\lambda_j^{-N}}{\lambda_j - 1} \hat{p} = 0 \tag{7.49}$$

where $j = 1, 2$.

Choosing an integer N, a linear problem is formed from (7.49) as follows

$$\alpha(N) \begin{bmatrix} p \\ \hat{p} \end{bmatrix} = \gamma\beta$$

where γ is a scaling factor and $p = \begin{bmatrix} p_0 & p_1 & p_2 & \dots & p_N \end{bmatrix}^T$. The desired value of γ is 1. Matrices α and β are in (7.50) for the heater part.

$$\begin{aligned} \alpha(N) &= \begin{bmatrix} 0 & 0 & ... & 0 & \sum_{k=1}^{2} \frac{H_k}{1-\lambda_k} \\ H_1 & H_1\lambda_1^{-1} & ... & H_1\lambda_1^{-N} & H_1 \frac{\lambda_1^{-N}}{\lambda_1 - 1} \end{bmatrix} \\ \beta &= \begin{bmatrix} r \\ 0 \end{bmatrix} \end{aligned} \tag{7.50}$$

Considering the actuator saturation problem, we set the power limits as

$$\begin{aligned} u_{min} \leq & p_i \leq u_{max} \\ u_{min} \leq & \hat{p} \leq u_{max} \end{aligned} \tag{7.51}$$

where $i = 0, 1, 2, ..., N$, $u_{max} = 7000\,W$ and $u_{min} = 0\,W$.

Initially, N is chosen to obtain p_i and $\hat{p}$. If p_i and $\hat{p}$ do not satisfy the limits in (7.51), then N should be increased. If p_i and $\hat{p}$ satisfy the limit, N should be decreased to the smallest possible that satisfies (7.51).

If the desired output air temperature, r, is 140 ^oC, we obtain $p_i = 9782$ and $\hat{p} = 5396.5$ by choosing $N = 500$. Because $p_i = 9782 > u_{max} = 7000$, then N is increased to calculate p_i and $\hat{p}$ again. Finally we find that the power input is 7000

W before $N = 936$ steps and 5396.5 W after $N = 936$ steps. The result is shown in Figure 7.18, where the open-loop system is used, the heat recycle is not applied and the air velocity is $5\,m/s$. Figure 7.18(a) shows good tracking action of the

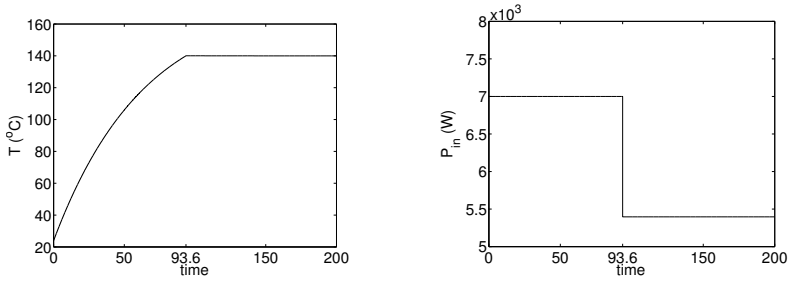

(a) T (b) P_{in}

Figure 7.18: Response of the heater part

system when the open-loop is used.

With different set points for air velocities and temperatures, different N and different input power values can be obtained by using the same method. These values are used to build a database off line, and they can be applied on line for control.

In order to reject any disturbance in the air velocity and handle other modeling errors, a closed-loop system shown in Figure 7.19 is designed using the modified PID controller:

$$U(s) = K_p\{bU_c(s) - Y(s) + \frac{1}{T_i s}[U_c(s) - Y(s)] - \frac{T_d s}{1+\frac{T_d s}{N}}Y(s)\} \tag{6.8}$$

The modified PID controller, (6.8), is used as the controller in the discrete system model shown in Figure 7.19. For its application in the discrete system (Åström and Wittenmark, 1997), the proportional part of (6.8), becomes

$$u_P(k) = K_p(bu_c(k) - y(k)) \tag{7.52}$$

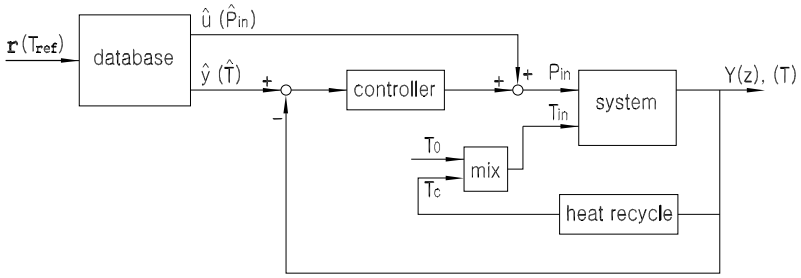

Figure 7.19: Transfer diagram of the closed-loop system

The integral part of (6.8) is replaced by

$$u_I(k+1) = u_I(k) + \frac{K_p h}{T_i} e(k) \tag{7.53}$$

where $e(k)$ is the error. The derivative part of (6.8) becomes

$$u_D(k) = \frac{T_d}{T_d + Nh} u_D(k-1) - \frac{K T_d N}{T_d + Nh}(y(k) - y(k-1)) \tag{7.54}$$

Using $u(k) = u_P(k) + u_I(k) + u_D(k)$ and selecting $K_p = 54.5$, $T_i = 35$, $T_d = 0.2$ $b = 0.85$ h=0.01 and $N = 10$ for the heater part, we obtain the result shown in Figure 7.20 where $v_a = 5\,m/s$ and the set point of T is changed from $140\,^oC$ to $150\,^oC$ at time $300\,sec$.

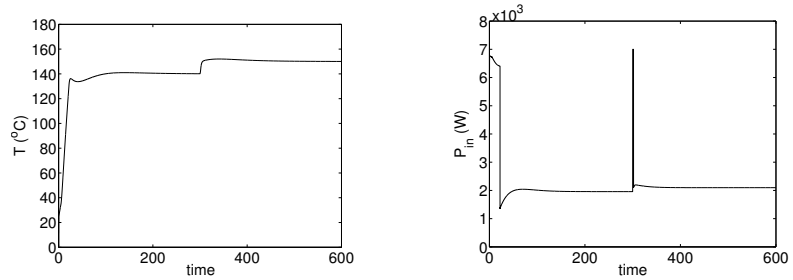

(a) T (b) P_{in}

Figure 7.20: Response of the closed-loop heater part by using the modified PID controller

From the above simulation results, we see that the problem of actuator saturation is well solved.

7.7 Comparisons of the Different Control Methods

The state feedback control, LQR and LQG methods have their own advantages. The state feedback control can place the poles of the system at arbitrary locations. The LQR controller is designed to minimize the cost function. The LQG controller is more robust to measurement noise. Although, the desired transient response can be obtained by the use of the state feedback controller (see Figures 7.2(a) and 7.5(a)), when T_{load} is added, the oscillations of the responses using the LQR and LQG controllers are smaller than those using the state feedback controllers (see Figures 7.7, 7.11 and 7.14). This is due to the large weight put on the error when the LQR and LQG controllers were designed.

7.8 Conclusion

In this chapter, three control methods for the heat gun, namely state feedback control, LQR and LQG, were discussed. For different control methods, responses of the heat gun were presented to show the effects of the controllers. Besides these, solutions of disturbance rejection, actuator saturation and the influence of heat recycle were also developed.

Chapter 8

Conclusions

8.1 Main Achievements

The heat gun designed in this thesis has attained the requirements listed as follows,

1. High air volume.

   In this thesis, an air velocity of at least $5\,m/s$ is considered when choosing the motor and designing the controllers. As a result, the air volume of the heat gun is at least $0.04\,m^3/s$.

2. Controllable air temperature and air velocity.

   The control of the air temperature is realized by controlling the power input to the main resistive coils and additional coil. The air velocity is regulated by controlling the rotation speed of the DC motor. Controllers of the heat gun were designed by using different control methods including PID control, state feedback control, LQR and LQG. In addition, disturbance rejection, actuator saturation, and the influence of heat recycle and measurement noise are also taken into consideration in the design of the controllers.

3. Uniform air temperature and velocity.

With the design of the heat gun structure and controllers, the uniformity of the output air temperature is less than $\pm 0.5\,^oC$ for a range between $120\,^oC$ and $200\,^oC$, and the uniformity of the output air velocity is not more than $5 \pm 1\,m/s$.

8.2 Some Suggestions

The goal of designing and developing a new air heater which meets the requirements of the heating process for wafers is well considered. Further research which may improve the performance of the heat gun are as follows:

1. The shape of the vanes which drive the air through the heat gun plays an important role on the air movement. Some analysis on the shape may bring some improvement to the air velocity uniformity.

2. Other software can be utilized in the new heaters so that a favorable human-machine interface could be created, such as LabVIEW.

3. The practical heat gun could be constructed to test the simulation results.

Bibliography

Åström, K. J. and B. Wittenmark (1997). *Computer-Controlled Systems: Theory and Design*. third ed.. Upper Saddle River, NJ: Prentice Hall.

Åström, K. J. and T. Hägglund (1988). *Automatic Tuning of PID Controllers*. Research Triangle Park, NC: Instrument Society of America. New York: J. Wiley.

Atkins, M. R. (2005). Compact integrated forced air drying system. *United States Patent 6,931,205*.

Bejan, A. (1995). *Convection Heat Transfer*. second ed.. New York: J. Wiley.

Burmeister, L. C. (1993). *Convective Heat Transfer*. second ed.. New York: J. Wiley.

Cameron, D. M. (1993). Fixed volume ptc air heater with heat output adjusted by a damper controlling air flow over the ptc element. *United States Patent 5,197,112*.

D'Azzo, J. J. and C. H. Houpis (1981). *Linear Control System Analysis and Design: Conventional and Modern*. second ed.. New York: McGraw-Hill.

Emami-Naeini, A., M. G. Kabuli and R. L. Kosut (Dec. 1994). Finite-time tracking with actuator saturation: Application to rtp temperaturetractory following. In: *Proc. Conf. Decision Control*. pp. 73–78.

Franklin, G. F., J. D. Powell and A. Emami-Naeini (1994). *Feedback Control of Dynamic Systems*. third ed.. Reading, Mass. : Addison-Wesley.

Gillespie, D. R. H. (1993). *First Year Report*. University of Oxford.

Glucksman, D. Z. and J. A. Deros (1997). Electric air heater with cage-shaped heating element comprised of resistance alloy strips and inclined guide vanes. *United States Patent 5,619,612*.

Gorlach, I. A. (2004). Model of a thermal gun for abrasive blasting. *CD-adapco Dynamics*.

Holman, J. P. (1988). *Thermodynamics*. fourth ed.. New York: McGraw-Hill.

Holman, J. P. (1997). *Heat Transfer*. eighth ed.. New York: McGraw-Hill.

Kreith, F. and M. S. Bohn (1986). *Principles of Heat Transfer*. forth ed.. New York: Harper & Row.

Malloy, J. F. (1969). *Thermal Insulation*. New York, Van Nostrand-Reinhold.

Menassa, C. (2001). Air heating device. *United States Patent 6,169,850*.

Ogata, K. (2002). *Modern Control Engineering*. fourth ed.. Upper Saddle River, New Jersey: Prentice Hall.

Plummer, J. D., M. Deal and P. B. Griffin (2000). *Silicon VLSI Technology: Fundamentals, Practice and Modeling*. Upper Saddle River, NJ: Prentice Hall.

Skogestad, S. and I. Postlethwaite (1996). *Multivariable Feedback Control: Analysis and Design*. first ed.. Chichester, New York: Wiley.

UL499 (1997). Electric heating appliances. *UL STANDARDS*.

Wade, P. and C. Tyler (1997). An investigation of various unwrap/reduction methods to quantify phase-shifted holographic interferometry. In: *ICIASF'97*

Record. International Congress on Instrumentation in Aerospace Simulation Facilities. pp. 322–328.

Wang, Z., D. R. H. Gillespie and P. T. Ireland (1996). Advances in heat transfer measurements using liquid crystals. *Engineering Foundation, Turbulent Heat Transfer* pp. 1–25.